Type-I fractons — foliation in non-abelian models

Thesis by

Zongyuan Wang
(王宗远)

In Partial Fulfillment of the Requirements for the
degree of
Ph.D. in Physics

CALIFORNIA INSTITUTE OF TECHNOLOGY
Pasadena, California

2025
Defended May 9th, 2025

© 2025

Zongyuan Wang
(王宗远)
ORCID: 0000-0003-0813-6247

All rights reserved

ACKNOWLEDGEMENTS

I am deeply grateful to my advisor, Xie Chen, for her constant patience, encouragement, and guidance throughout my study at Caltech. I have learned immensely from her mentorship. This thesis would not have been possible without her consistent and timely support.

I would like to thank my Ph.D. examination committee for their invaluable guidance and support, from my initial candidacy exam to the final thesis defense: Jason Alicea, Olexei Motrunich, and Nai-Chang Yeh. And, I would like to thank Anton Kapustin and Kenneth G. Libbrecht for their advice during the early stage of my Ph.D.

I am grateful to my collaborators for their inspiring discussions and dedicated hard work. Without them, I would not have been able to complete any of my projects: Arpit Dua, Michael Hermele, Xiuqi Ma, Ananth Malladi, Wilbur Shirley, David T. Stephen, Avi Vadali, and Zhenghan Wang.

I was fortunate to be surrounded by friends and colleagues whose companionship and generous support means a great deal to me. I would like to express my gratitude and acknowledge them for being a part of my Ph.D. journey, especially: Eric Black, Yu-An Chen, Yinan Chen, Margarita Davydova, Dolores (Loly) Ekmekjian, Xiaozhen Fu, Shouzhen Gu, Yingfei Gu, Jeongwan Haah, Po-Shen Hsin, Wenjie Ji, Ho Tat Lam, Dongjun Li, Zhiru Liu, Yue Liu, Di Luo, Yang Lyu, Lin Ma, Yutao Ma, Linhao Ma, Nandagopal Manoj, William Morong, Akiyoshi Park, Christopher A. Pattison, Linqing Peng, Kevin Slagle, Nathanan Tantivasadakarn, Yuiki Takahashi, Bowen Yang, Lei Gioia Yang, Zixin (Gary) Ye, Phelan Yu, Robijn Vanhove, Sara Vanovac, Ziyi Wang, Xiao-Gang Wen, Dominic J. Williamson, Jian-Hao Zhang, Jiaxin Zhang, Yiwen Zhang, and Sisi Zhou.

I am deeply grateful to my parents for their timely support and unwavering belief in me. I feel incredibly fortunate to have been raised in a family that fosters a growth mindset and encourages me every step of the way.

Lastly, I would like to share a reference that I think might help people at any stages of their studies or careers: Richard Hamming's talk on his research experiences and methodologies [1].

While this thesis marks the end of my Ph.D. journey, standing at where I am now, I feel that the most significant chapter of my life is just beginning. What comes next?

With eager resolve, I stride into the uncharted future where new stories will unfurl and unknown heights await discovery.

ABSTRACT

In this thesis, we present recent contributions to the study of Type-I non-abelian fracton models, which led us to propose the notion of *generalized foliated fracton orders* that captures the universal properties of both abelian and non-abelian Type-I fracton models.

Fracton models are known for their exotic properties such as point-like excitations with restricted mobilities and robust topological ground state degeneracy that grows sub-extensively with the system size. A multitude of Type-I fracton models whose excitations obey either abelian or non-abelian fusion rules have recently been constructed. Among them, a large number of the abelian fracton models have been shown to possess foliation structures, where models of different system sizes can be related through the addition / removal of an entire piece of topologically ordered system on a sub-dimensional manifold via the action of a finite-depth local unitary circuit. In this thesis, this is referred to as the *original* foliation renormalization group (RG) scheme, which leads us to the notion of original foliation fracton orders. The Ising cage-net model and other similar non-abelian models are closely related to these abelian models in terms of their excitation structures and coupled layers construction etc. However, it was not known whether their fracton orders can also be understood within the original foliation framework. We address this problem in this thesis.

In Chapter 2, we show that the Ising cage-net model does not fit into the original definition of foliated fracton orders, by calculating its ground state degeneracy. We realize that there exists naturally a more general way to define foliation – the *generalized foliation scheme* (Chapter 3). The Ising cage-net and other similar non-abelian fracton models are foliated according to this generalized scheme. In the generalized foliation scheme, the RG transformation is defined by, from the excitation perspective, the condensation of planons / gauging subsystem symmetries. In terms of quantum circuits, this RG transformation is equivalent to a sequential linear-depth circuit that acts near a sub-dimensional manifold. With this definition, we can study phase relation of the Ising cage-net with other known fracton models. In Chapter 4, via *gauging composite subsystem symmetries*, we further show that the Ising cage-net belongs to the same generalized foliated fracton phases as the prototypical X-cube model. Furthermore, gauging composite subsystem symmetries opens up a new route to constructing non-abelian fracton models hosting exotic non-abelian

fractons. An example is the *tri-Ising-fracton model* (Sec. 4.5).

PUBLISHED CONTENT AND CONTRIBUTIONS

[1] Xiuqi Ma, Ananth Malladi, Zongyuan Wang, Zhenghan Wang, and Xie Chen. "Ground state degeneracy of the Ising cage-net model". In: *Phys. Rev. B* 107 (8 Feb. 2023), p. 085123. DOI: 10.1103/PhysRevB.107.085123.
Zongyuan Wang participated in the conception of the project, the theoretical analysis, and the writing of the manuscript.

[2] Zongyuan Wang, Xiuqi Ma, David T. Stephen, Michael Hermele, and Xie Chen. "Renormalization of Ising cage-net model and generalized foliation". In: *Phys. Rev. B* 108 (3 July 2023), p. 035148. DOI: 10.1103/PhysRevB.108.035148.
Z.W. participated in the conception of the project, the theoretical analysis, and the writing of the manuscript.

[3] Avi Vadali, Zongyuan Wang, Arpit Dua, Wilbur Shirley, and Xie Chen. "Composite subsystem symmetries and decoration of sub-dimensional excitations". In: *SciPost Phys.* 17 (2024), p. 071. DOI: 10.21468/SciPostPhys.17.3.071.
Z. W. participated in the conception of the project, the theoretical analysis, and the writing of the manuscript.

TABLE OF CONTENTS

Chapter 1

INTRODUCTION

Quantum computers hold promising potential to efficiently solve problems that are expensive on classical machines [2]. However, they are prone to errors. Today's quantum computers have error rates on the order of 10^{-3} for two-qubit gates [3–13], underscoring the need for fault-tolerant schemes. Fault-tolerant schemes suppress errors from the physical components of a quantum computer, provided that these components operate below some error rate threshold. Below this threshold, these schemes correct errors faster than new errors could occur. Thereby, the encoded logical information is maintained. One route to fault-tolerance is to protect logical information by encoding it across multiple entangled qubits. This led to the development of fault-tolerant schemes via quantum error correction codes [14–17].

For quantum processors, fault-tolerant computation can be achieved by performing error correction actively using quantum codes. Errors originating from the components of a quantum computer do affect encoded information in the quantum codes. However, their impact can be reversed. To do so, these codes require an accompanying *fast* decoding protocol. Decoding involves two steps. First, the presence of errors must be detected as they occur. Second, a recovery operation must be applied before the errors can propagate to inflict irreversible damage to the encoded logical information. Significant progress has been made in the implementation of quantum codes in quantum processors. Notably, the Google Quantum team recently reported the achievement of below-threshold quantum error correction using the surface code on their superconducting-qubit-based quantum computer [18].

For quantum memories, on the other hand, a higher goal is to store the encoded information without active error correction. To achieve this, quantum codes are required to be intrinsically resilient against errors and, in the thermodynamic limit, the coherence time for the encoded information diverges. This led to the notion of self-correcting codes [19]. To date, self-correcting codes still await theoretical breakthrough.

Self-correcting codes exist in 4D. The prototypical example is the 4D toric code, where the energy cost of creating a logical error grows in the linear system size and where, below a critical temperature, the encoded information has a coherence time

that scales exponentially in the linear system size [20]. Are there self-correcting codes in lower dimensions? More specifically, do they exist in 3D? In an attempt to answer this question, Haah's cubic code was proposed.

It is known that string-like logical operators, whose generation involves only constant energy cost, were impediments to self-correction. This is the key to proving the no-go theorems for self-correcting codes in 2D [21–23]. To search for self-correcting codes in any dimension, we need to, first, find codes without string-like operators. An outcome of this search in 3D is the Haah's cubic code (code No.1 in Ref. [24]), which was later recognized to be the defining model of a new class of quantum phases of matter – fracton orders [25]. It is to be noted that Haah's cubic code does not achieve an exponential storage time [26]. The search for low dimensional (≤ 3) self-correcting codes remains open.

1.1 Debut of fractons

Introduced in 2011, Haah's cubic code is a 3D quantum stabilizer code defined on a three-dimensional cubic lattice without string-like logical operators [24]. The excitations are point-like and are created by tetrahedron-shaped operators. As shown in the leftmost illustration in Fig. 1.1, such an operator creates four point excitations at the corners. The four point excitations can move in a coordinated manner with the enlargement of the tetrahedron-shaped operator across multiple cubic cells (middle and rightmost illustrations of Fig. 1.1). However, individual point excitation cannot be moved from one cubic cell to another without incurring additional energy costs. In other words, there does not exist an operator that transports a single point excitation. Hence, individual point excitations are immobile.

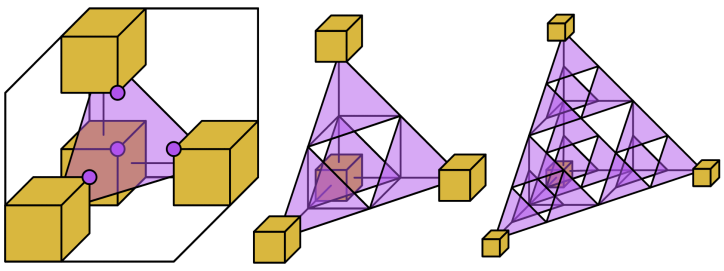

Figure 1.1: Excitations in the Haah's cubic code and their movements. Every yellow cube indicates the location of a point excitation. These point excitations are created by the tetrahedron-shaped operators in purple. The excitations are only move in a coordinated fashion as shown in the left, middle, and right. Illustrations taken from Ref. [27].

Such an immobile point excitation is termed *fracton* in 2016 [25]. The name comes from the observation that these excitations can only move in a coordinated formation. When the entire formation is viewed as a single mobile quasiparticle, each individual point excitation may be interpreted as a fraction of that quasiparticle, hence the name [25].

Haah's cubic code has properties that are different from the familiar topologically ordered systems. On the 3-torus, it has a ground state degeneracy (GSD) that exhibits strong oscillations dependent on the linear system size, bounded within an exponentially scaling envelope [24]. Therefore, it does not fit into the notion of topological order where the GSD on a manifold depends only on its topology but not the system size[1] [29]. The dependence of the GSD on the system size signals that Haah's cubic code has a different order.

Given the exotic features of Haah's cubic code, an immediate question arises: do fractons exist in other models? The answer is yes. In retrospect, the first fracton model is the Chamon model, discovered in 2005 [30]. Similar to Haah's cubic code, the Chamon model has a GSD that scales exponentially in the linear size of the system, and it has point excitations that are individually immobile, i.e. fractons [31]. Moreover, the Chamon model hosts additional point excitations that are partially mobile: *lineons*, which are only mobile along a line, and *planons*, which are only mobile within a plane.

The Chamon model and Haah's cubic code are representatives of the two types of fracton models based on their excitations' mobilities. *Type-II* fracton models, such as the Haah's cubic code, feature only fractons. *Type-I* fracton models, such as the Chamon model, feature excitations that possess partial mobilities.

1.2 Zoo of fracton models

Fractons emerged unexpectedly from the discovery of the Chamon model and Haah's cubic code. This naturally raises the question: how do we systematically construct fracton models? More fundamentally, what physical mechanisms give rise to the characteristic restricted mobilities?

In 2016, it was discovered that fractons can be constructed from gauging subsystem symmetries [25]. For example, fractons can arise from gauging planar subsystem

[1] Take the toric codes as examples of topologically ordered systems. The 2D toric code has a GSD of 4 on the 2-torus [17], and the 3D toric code has a GSD of 8 on the 3-torus [28]. None depends on the system size.

symmetries in all three directions. As shown in (a) of Fig 1.2, a symmetry charge that transforms under only one planar symmetry is fully mobile within the plane. When a symmetry charge transforms under two intersecting planar symmetries, the charge is restricted to move along the intersection of the two planes and thus is a lineon, (b) of Fig 1.2. Finally, as shown in (c) of Fig 1.2, if a symmetry charge transforms under three intersecting planar symmetries, then it is immobile. Upon gauging, these symmetry charges become fractionalized excitation with the corresponding mobilities. That is, the symmetry charge in (a) after gauging becomes a planon. The symmetry charge in (b) becomes a lineons. Lastly, the symmetry charge in (c) becomes a fracton.

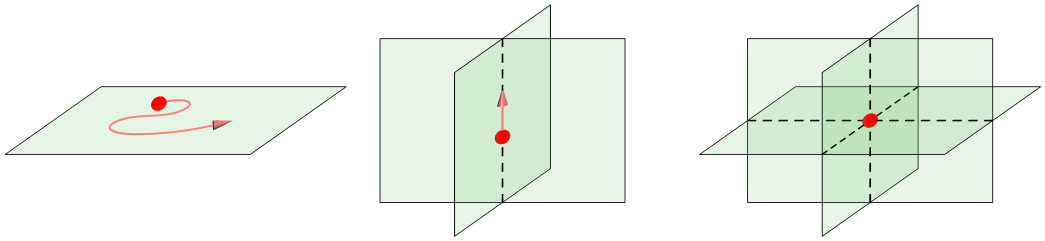

Figure 1.2: Mobilities of the symmetry charges (the red dots). (a) a symmetry charge, transforming under one planar symmetry, is mobile within the plane. Upon gauging it becomes a planon; (b) a symmetry charge, transforming under two planar symmetries, becomes a lineon after gauging; (c) a symmetry charge, transforming under three planar symmetries, becomes immobile and hence a fracton after gauging.

Gauging subsystem symmetries is a powerful method for building fracton models. The Chamon model and Haah's cubic code can be obtained by gauging planar and fractal subsystem symmetries respectively [25]. The method also yields another paradigmatic example of fracton, the X-cube model [25], which we review in Chapter 3. Subsequent works, including Chapter 4 of this thesis, unveiled many more exotic fracton models [32–37].

Another route to constructing fracton models is by coupling together lower dimensional lattice systems [38–41]. A notable example obtained via a coupling method is the Ising cage-net, which hosts non-abelian lineons [42]. The Ising cage-net serves as the prime example of a non-abelian fracton model in this thesis. We briefly mention its significance in Sec. 1.4 and review it in detail in Chapter 2.

Parallel to the lattice model constructions, fracton models have also been built from field-theoretic approaches. In 2017, it was discovered that fracton can arise from the conservation of dipole and higher moments of charges in higer-rank gauge theories

[43, 44]. In 2018, it was discovered that the rank-two $U(1)$ gauge theory can lead to the X-cube model via the Higgs mechanism [45, 46]. The quest for building fracton models was carried on by several following works such as Ref. [47, 48].

1.3 The notion of fracton phases: (original) foliation

Fracton models are representatives of different orders than the topological orders. Recall from Sec. 1.1, the Chamon and Haah's cubic code have GSDs that grow sub-extensively with the system size. This feature is ubiquitous among fracton models. However, it is not present in topologically ordered models where the GSDs depend on the topology but invariant with respect to the size of the system. If we were to naively classify fracton models according to the definition of topological orders [29, 49–51], then each system size of a fracton model would be classified to represent a different topological order. Therefore, the classification of fracton models by the notion of topological orders is not meaningful. This calls for a new notion to classify fracton models – fracton orders.

How do we define fracton orders? More technically, since quantum phases are defined by renormalization group (RG) transformations, the question for fracton phases boils down to: how do we define RG transformations for fracton models? For Type-I fracton models, it was discovered that many of them possess a foliation structure.

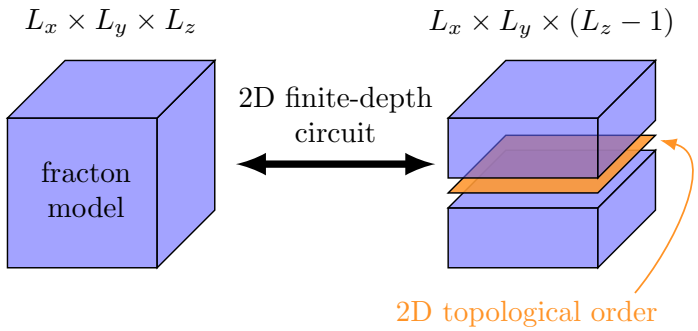

Figure 1.3: An illustration of the original foliated RG scheme in 3D. In this scheme, a layer of 2D topologically ordered system can be added into or removed from a fracton model via a finite-depth local unitary circuit near the plane. For an example, see Sec. 3.1 where we review the foliation structure of the X-cube model.

In 2018, it was found that we can enlarge (or shrink) the 3D X-cube model by adding (or removing) a 2D toric code topological order via a finite-depth local unitary circuit near the 2D sub-manifold [52]. This immediately led to the introduction

of the *(original) foliated RG* as illustrated in Fig. 1.3, and subsequently *(original) foliated fracton orders* [32, 52, 53].

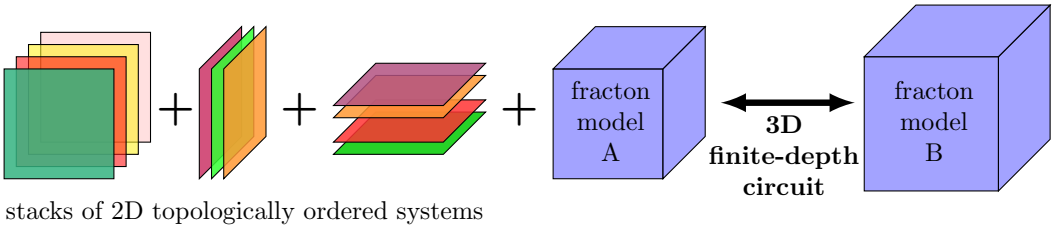

Figure 1.4: An illustration of the equivalence relation for original foliated fracton orders in 3D. This equivalence relation is induced by the original foliation RG (Fig. 1.3). Two fracton models A and B have the same original foliated fracton order if they can be transformed into each other via a 3D finite-depth circuit with stacks of 2D topologically ordered systems as resources.

The original foliation RG scheme induces an equivalence relation for fracton models. This equivalence relation then defines the notion of original foliated fracton orders. Fracton models are said to have the same original foliated fracton order if they can be transformed into each other via the addition or removal of sub-dimensional topological orders through finite-depth local unitary circuits as shown in Fig 1.4 [32, 52, 53]. Under this equivalence relation, the X-cube model, the semionic X-cube, the checkerboard model, and the Majorana checkerboard model can all be transformed into each other [53–55]. Therefore, they have the same original foliated fracton order.

1.4 Beyond foliation? – Ising cage-net and generalized foliation

Not all fracton models are foliated in the sense of Sec. 1.3, even for some of the Type-I models[2]. In 2019, a non-abelian Type-I fracton model, the Ising cage-net, was discovered [42]. A question immediately arises: is the Ising cage-net foliated? The Ising cage-net is similar to the foliated models such as the X-cube model in many ways. Both models have fractons, lineons, and planons. Both can be constructed by coupling intersecting stacks of the doubled-Ising string-net (in the case of Ising cage-net) and intersecting stacks of the 2D toric code (in the case of X-cube) [41, 42]. A naive expectation is that the Ising cage-net is foliated. However, in Chapter 2, we answer this question in the negative: the Ising cage-net cannot fit into the original foliated RG scheme.

It is then curious to ask: can we think of the Ising cage-net model as a fixed point

[2]Haah's cubic code and similar Type-II fracton models obviously cannot be foliated.

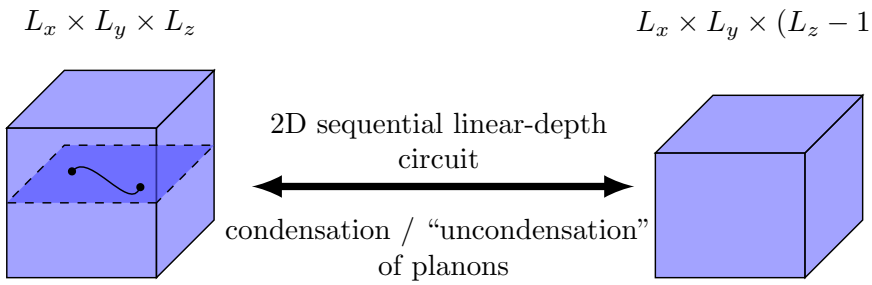

Figure 1.5: An illustration of the generalized foliation RG scheme in 3D. It contains the original foliation as a special case. The generalized foliation RG transformations are given by condensation of bosonic planons / "uncondensation" (i.e. gauging, see Chapter 4), or equivalently, by a sequential linear-depth circuit near the plane.

of a suitably generalized RG? More specifically, can the foliated RG be generalized somehow to include the Ising cage-net model? In Chapter 3, we answer this question in the positive. We find that there is a natural way to generalize the original foliation to the *generalized foliation scheme*. We show that the Ising cage-net is a fixed point model under this scheme. The generalized RG transformation can be understood from two perspectives in terms of excitations and quantum circuits, as shown in Fig. 1.5. From the excitation point of view, the RG transformation is defined by condensation / "uncondensation" of bosonic planons. In terms of quantum circuits, the RG is given by a sequential linear-depth circuit[3].

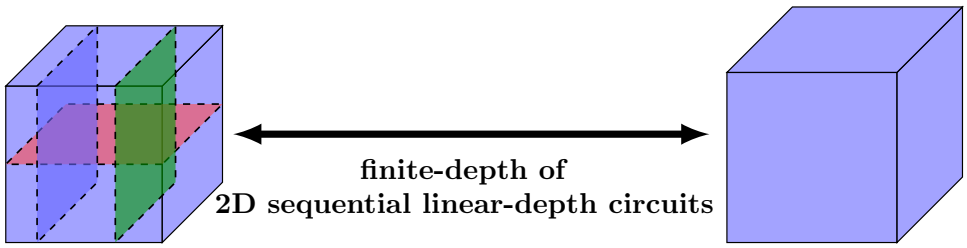

Figure 1.6: An illustration of the equivalence relation for generalized foliated fracton orders in 3D. Two fracton models are in the same foliated fracton phases if they can be related via a circuit of finite-depth of 2D sequential linear-depth circuits.

The generalized foliated RG scheme induces equivalence relations between fracton models, which subsequently define the notion of *generalized foliated fracton order*. As shown in Fig. 1.6, two fracton models are in the same generalized foliated fracton order if they can be transformed into each other via a circuit that is a finite-depth of sub-dimensional sequential linear-depth circuits. Using this equivalence relation,

[3]The original foliated RG arises as a special case of the generalized procedure, because finite-depth local unitary circuits are strictly a subset contained in the set of sequential linear-depth circuits near the sub-manifold.

we show that the Ising cage-net and the X-cube model have the same generalized foliated fracton order (Chapter 4).

1.5 Non-abelian fracton from gauging composite subsystem symmetries

Given the generalized foliated scheme, we can ask: to which generalized foliated fracton phase does the Ising cage-net belong? We show that the Ising cage-net and the X-cube model are in the same generalized foliated fracton order in Chapter 4. We establish this equivalence through a method that we call *gauging composite subsystem symmetries*. Precisely, we find that the Ising cage-net can be obtained by dressing up fractional excitations of the X-cube model via condensation of planons. The power of gauging composite subsystem symmetries goes beyond reproducing the Ising cage-net. Many more exotic fracton models can be built, including non-abelian fractons.

Non-abelian fractons have been elusive and challenging to construct. Extensive efforts have been devoted to finding these model [39, 42, 56–62]. In Sec. 4.5, via gauging composite subsystem symmetries, we discover a new Type-I fracton model, in which all fractons are non-abelian. This new model is obtained by decorating the fracton of the X-cube model with three Ising anyons. Therefore, each of the fractons has a quantum dimension of $(\sqrt{2})^3$. We name this model the *tri-Ising-fracton model*. We note that, in terms of the generalized foliation, the tri-Ising-fracton model have the same order as the X-cube model and the Ising cage-net.

1.6 What's next for fractons?

The study of fracton is at its early stage. There are still many open questions. For example, having established the notion of generalized foliated fracton order, what are the invariant quantities? In the original foliated fracton orders, two invariant quantities are the quotient superselection sectors [53] and entanglement entropy [63]. In view of the generalized scheme, do these quantities remain as invariants of generalized foliated fracton orders? If not, what are their counterparts in the generalized orders? Furthermore, besides the X-cube / the Ising cage-net order, are there other universality classes? Specifically, in the original foliation, the twisted models in Ref. [64] represent distinct fracton phases from that of the X-cube model. In the generalized scheme, do these twisted models still represent different generalized foliated fracton orders than that of the X-cube? On the other hand, we expect that the fracton models constructed through gauging strong subsystem symmetry protected topological (SSPT) models cannot be obtained from gauging

composite subsystem symmetries (Chapter 4). Therefore, we expect these gauged SSPT models represent different generalized foliated fracton orders than that of the X-cube. Is our expectation correct? These questions await future explorations.

Recently, Type-I fracton models have been studied in the infinite component Chern-Simons theories [65–67]. They do not have fractons. Still, they host excitations with restricted mobilities: lineons and planons. Many of these models are not foliated even according to the generalized scheme. It then remains open to design RG transformations for these models and, in turn, to classify their orders.

1.7 Organization of the thesis

In this section, we summarize the contents of this thesis as well as the connections between the Chapters.

In Chapter 2, we calculate the ground state degeneracy of the Ising cage-net model and find that, even though it follows a similar coupled layer structure as the X-cube model, the Ising cage-net model cannot be foliated in the same sense as with the X-cube model as defined in Ref. [52]. A generalized notion of foliation is hence needed to understand the renormalization group transformation of the Ising cage-net model. The calculation is performed using an operator algebra approach that we develop in this Chapter, and we demonstrate its validity through a series of examples.

In Chapter 3, we introduce the generalized foliated RG scheme under which the Ising cage-net is a fixed point model, and which includes the original foliated RG as a special case. The Ising cage-net model thus gives a prototypical example of the generalized foliated RG, and its system size can be changed either by condensing / “uncondensing" bosonic planon excitations near a 2D plane or through a linear-depth quantum circuit in the same plane. We show that these two apparently different RG procedures are closely related, as they lead to the same gapped boundary when implemented in part of a plane.

In Chapter 4, we construct fracton models with exotic lineons and fractons via gauging composite symmetries. More specifically, we investigate 3D systems with planar symmetries where, for example, the planar symmetry of a planon charge is combined with one of the planar symmetries of a fracton charge. We propose the principle of Remote Detectability to determine how the gauge fluxes bind and potentially change their mobilities. This understanding is then used to design fracton models with sub-dimensional excitations that are decorated with excitations having nontrivial statistics or non-abelian fusion rules. In particular, we show that the

Ising cage-net can be obtained by the decoration of the excitations in the X-cube model. Therefore, the Ising cage-net and the X-cube model belong to the same order according to generalized foliation scheme in Chapter 3. We also discover a new Type-I non-abelian fracton model, the tri-Ising-fracton model.

Chapter 2

GROUND STATE DEGENERACY OF FRACTON MODELS: AN OPERATOR ALGEBRA PERSPECTIVE

Is the Ising cage-net foliated? The original foliation scheme[1] requires that for a foliated fracton model, an entire layer of 2D topological order to be added or removed from the model [32, 52]. It then follows that a necessary condition for a fracton model to be foliated is: on given a topology, its GSD for different system sizes must be related by an integral factor. That is, for $L_1 > L_2$, $\mathrm{GSD}(L_1)/\mathrm{GSD}(L_2) \in \mathbb{Z}$. Therefore, one thing we can check is the GSD of the Ising cage-net on the 3-torus.

The Ising cage-net model is an exactly solvable model. We can compute the GSD by constructing the ground space projector from its Hamiltonian terms. However, since the Ising cage-net model is not a stabilizer model, the computation of its GSD is not simple (the GSD of minimal Ising cage-net of size $1 \times 1 \times 1$ is computed in Appendix 2.11). To overcome this challenge, we develop an operator algebra method for computing the ground state degeneracy of the Ising cage-net model.

Using this method, we find the GSD of an $L_x \times L_y \times L_z$ Ising cage-net to be

$$\mathrm{GSD} = \frac{1}{8}\left(E_3 + E_2 + 5E_1 + 45\right), \tag{2.1}$$

where $E_3 = 9^{L_x+L_y+L_z}$, $E_2 = 9^{L_x+L_y} + 9^{L_y+L_z} + 9^{L_z+L_x}$, and $E_1 = 9^{L_x} + 9^{L_y} + 9^{L_z}$. Direct calculation shows that the GSD does not grow by integer multiples when the system size grows. For example, when $L_x = L_y = L_z = 2$, GSD = 69048; when $L_x = L_y = 2, L_z = 3$, GSD = 614016. Therefore, Ising cage-net cannot be foliated in the sense that its system size can be increased / decrease by adding / removing 2D topological orders via a finite-depth circuit.

In Chapter 3, we show that the system size of Ising cage-net can be changed by condensing / "uncondensing" bosonic planon excitations near a 2D plane or, correspondingly, through a linear depth circuit that scales with the size of the plane. This constitutes what we call the *generalized foliated scheme* for renormalization group transformation.

The rest of this Chapter is organized as follows: In Section 2.1, we review the Ising cage-net. In Section 2.3, we introduce the operator algebra approach to calculating

[1] We have introduced it in Sec. 1.3, and we will review it in detail in Chapter 3.

GSD by studying the simple example of the chiral Ising anyon model. The underlying mathematics of the operator algebra approach is the theory of semisimple algebras, and we discuss the structure of semisimple algebras in Section 2.4. More mathematical details can be found in Appendix 2.8. The construction of Ising cage-net involves p-loop condensation, and we study boson condensation in the operator algebra approach in Section 2.5 with the example of a condensation transition in the doubled Ising string-net model. We then use the operator algebra approach in Section 2.6 to study a more complicated 2D topological order, the one-foliated Ising cage-net model. This model is closely related to Ising cage-net – the main focus of this paper – but is still a 2D model so we can check the consistency of the operator algebra approach with anyon counting. Also in Section 2.6, we present another method of computing the GSD using a Cartan subalgebra. In Section 2.7, we put all of these tools together and compute the GSD of Ising cage-net in two ways: Cartan subalgebra and the full algebra of logical operators.

2.1 Review: the Ising cage-net

The building block of Ising cage-net is the doubled Ising string-net model [68] (doubled Ising for short). As a string-net model, doubled Ising can be realized on any 2D trivalent lattice. For the purpose of constructing Ising cage-net later, we choose a square-octagon lattice (Fig. 2.1). On each edge of the lattice, we put a local Hilbert space of dimension 3, with orthonormal basis vectors $|0\rangle$, $|1\rangle$ and $|2\rangle$. The labels $\{0, 1, 2\}$ are understood as values of "strings" located at the edges. We also need a set of symbols $(\delta_{ijk}, d_s, F^{ijm}_{kln})$, where all indices take values in $\{0, 1, 2\}$. For example, $\delta_{ijk} = 1$ if $ijk = 000, 011, 022, 112$ or their permutations, and $\delta_{ijk} = 0$ otherwise.

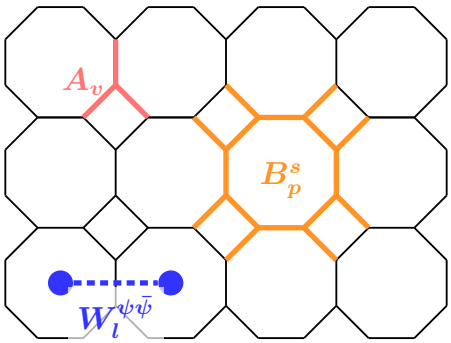

Figure 2.1: A square-octagon lattice. A vertex term A_v and a plaquette term B_p^s are shown. The string operator $W_l^{\psi\bar{\psi}}$ creates a $\psi\bar{\psi}$ excitation on each of the two plaquettes bordering the edge l.

The Hamiltonian consists of a vertex term A_v for each vertex v and a plaquette term B_p for each plaquette p. The vertex term is

$$A_v \left| \begin{array}{ccc} & j & \\ i & & k \end{array} \right\rangle = \delta_{ijk} \left| \begin{array}{ccc} & j & \\ i & & k \end{array} \right\rangle,$$

which allows certain ways for the strings to "fuse" at a vertex at low energy. The plaquette term is

$$B_p = \frac{\sum_s d_s B_p^s}{\sum_s d_s^2},$$

where the operator B_p^s involves the symbols F_{kln}^{ijm} and essentially acts by fusing an s-loop into the plaquette p. The precise definition of B_p^s is reviewed in Appendix 2.9. The full Hamiltonian is then

$$H = -\sum_v A_v - \sum_p B_p.$$

This is a commuting projector Hamiltonian when restricted to the low-energy subspace where $A_v = 1$ for all v. It has anyons 1, σ, $\bar{\sigma}$, ψ, $\bar{\psi}$, $\sigma\bar{\psi}$, $\psi\bar{\sigma}$, $\sigma\bar{\sigma}$ and $\psi\bar{\psi}$, where $\bar{\psi}$ is the time-reversal of ψ but otherwise unrelated to ψ, and similarly for $\bar{\sigma}$. In fact, doubled Ising can be viewed as the chiral Ising anyon model [69] (more discussion in Section 2.3) which has anyons 1, σ and ψ, stacked with its time-reversal which has anyons 1, $\bar{\sigma}$ and $\bar{\psi}$. This is where the name "doubled" Ising comes from. The fusion rules for σ and ψ are $\sigma \times \sigma = 1 + \psi$, $\sigma \times \psi = \sigma$, $\psi \times \psi = 1$; similarly for $\bar{\sigma}$ and $\bar{\psi}$. The R-symbols and string operators of the anyons can be found in Ref. [68], and we mention some important ones here:

- The braiding of σ with ψ gives a phase -1, and ψ braids trivially with ψ; same for $\bar{\sigma}$ and $\bar{\psi}$.
- The operator $W_l^{\psi\bar{\psi}} = (-1)^{n_1(l)}$ creates a $\psi\bar{\psi}$ excitation on each of the two plaquettes bordering the edge l, where $n_1(l) = 1$ if the state on the edge l is $|1\rangle$, and $n_1(l) = 0$ otherwise (Fig. 2.1). We can extend the blue dashed line to obtain a string operator of $\psi\bar{\psi}$.

As a 2D topological order, the GSD of doubled Ising is equal to the number of anyons [70], i.e. GSD = 9.

To construct Ising cage-net [42], we first stack up layers of doubled Ising in the x, y and z directions. The resulting lattice is a truncated cubic lattice (Fig. 2.2). In this lattice, an edge l_μ parallel to the μ direction for $\mu = x$, y or z is called a principal

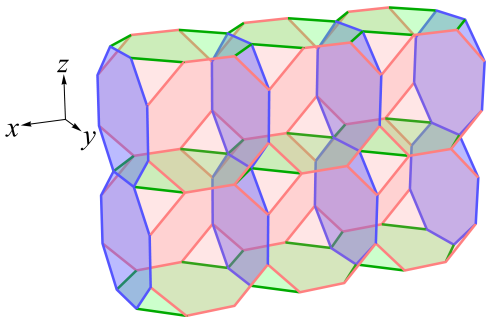

Figure 2.2: A truncated cubic lattice built from intersecting layers of the square-octagon lattice.

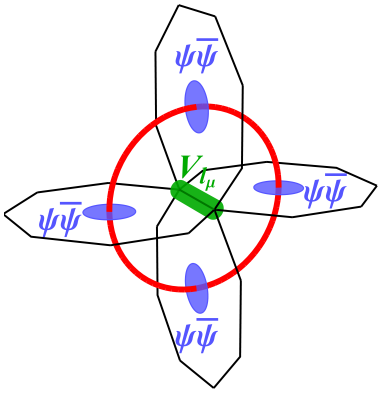

Figure 2.3: A $\psi\bar{\psi}$ p-loop shown in red. It is created by the operator V_{l_μ}, the green cylinder. Connecting the $\psi\bar{\psi}$ particles with line segments orthogonal to their hosting plaquettes, we obtain the p-loop.

edge. We will also distinguish the octagon and square plaquettes, denoting them by p_o and p_s, respectively. On a principal edge l_μ, the operator

$$V_{l_\mu} = W_{l_\mu}^{(\psi\bar{\psi})^\nu} W_{l_\mu}^{(\psi\bar{\psi})^\rho} = (-1)^{n_1^\nu(l_\mu)} (-1)^{n_1^\rho(l_\mu)} \tag{2.2}$$

creates a $\psi\bar{\psi}$ particle-loop ("p-loop" for short) around the edge (Fig. 2.3), where μ, ν and ρ are distinct. To be precise, $a^\mu(i)$ denotes the anyon a in the ith plane orthogonal to the μ direction, and we may omit the i label when it is clear from context. For example, if $\mu = x$ then we can take $\nu = y$, $\rho = z$, and the $\psi\bar{\psi}$ particles in the p-loop originate from the xz and xy planes. We can condense these p-loops with the Hamiltonian

$$H_0 - J \sum_\mu \sum_{l_\mu} V_{l_\mu},$$

where H_0 is the Hamiltonian for the decoupled layers of doubled Ising, and $J > 0$ is a large coefficient enforcing the condensation. This reduces the low-energy Hilbert space on each edge to one of dimension 5, spanned by $|00\rangle$, $|02\rangle$, $|20\rangle$, $|22\rangle$ and $|11\rangle$.

If we apply perturbation theory with H_0 as the perturbation, the plaquette terms $B^1_{p_o}$ must be assembled into cube terms

$$B_c = \prod_{p_o \in c} \frac{\sqrt{2}}{2} B^1_{p_o}$$

for each cube c. The resulting Hamiltonian of Ising cage-net is

$$H = -\sum_{v,\mu} A^\mu_v - \sum_{p_s} B_{p_s} - \sum_{p_o} \frac{1}{4}(1 + B^2_{p_o}) - \sum_c B_c, \tag{2.3}$$

where A^μ_v is the vertex term at vertex v orthogonal to the μ direction, and $B^2_{p_o}$ is the plaquette term of the 2-loop (not the square of an operator). The terms are shown in Fig. 2.4. This is a commuting projector Hamiltonian when restricted to the low-energy subspace where all vertex terms are satisfied.

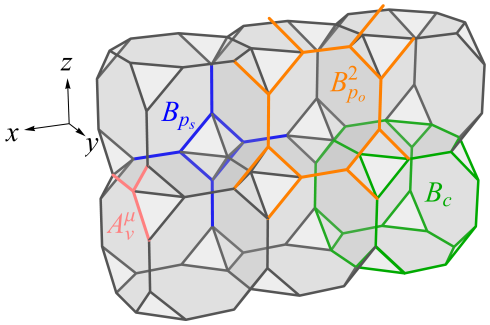

Figure 2.4: Hamiltonian terms of Ising cage-net. The full Hamiltonian is given by (2.3).

In order for an anyon to remain deconfined upon condensation, its string operator must commute with V_{l_μ}. In other words, the anyon must braid trivially with the $\psi\bar{\psi}$ p-loop. For example, a σ planon in an xy plane has a braiding phase -1 with a $\psi\bar{\psi}$ p-loop created by some V_{l_x} or V_{l_y}, and is therefore confined. On the other hand, a σ planon in an xy plane combines with a σ planon in an xz plane to form a lineon that moves in the x direction, and this lineon is deconfined. We summarize the deconfined excitations in Table 2.1.

Although Ising cage-net is exactly solvable, it is not obvious how to calculate its GSD. In the following sections, we will introduce a new way of calculating the GSD that applies to Ising cage-net. We will start with some simple 2D topological orders, and work our way up to Ising cage-net.

2.2 Overview of the method: operator algebra approach to GSD

As an exactly solvable model, the GSD of Ising cage-net can in principle be explicitly determined, but the non-abelian nature of the model complicates the problem. We

Mobility	Type	Excitations
Planon	Abelian	$\psi^\mu(i)$, $\bar{\psi}^\mu(i)$
	Non-abelian	$\sigma^\mu(i)\sigma^\mu(j)$, $\bar{\sigma}^\mu(i)\sigma^\mu(j)$, $\sigma^\mu(i)\bar{\sigma}^\mu(j)$, $\bar{\sigma}^\mu(i)\bar{\sigma}^\mu(j)$
Lineon	Abelian	
	Non-abelian	$\sigma^\mu(i)\sigma^\nu(j)$, $\bar{\sigma}^\mu(i)\sigma^\nu(j)$, $\sigma^\mu(i)\bar{\sigma}^\nu(j)$, $\bar{\sigma}^\mu(i)\bar{\sigma}^\nu(j)$

Table 2.1: Elementary excitations in Ising cage-net. We have $\mu \neq \nu$ in the lineon sector. The lineon $\sigma^x(i)\sigma^y(j)$ moves in the z direction; similarly for the other non-abelian lineons.

deal with it, as shown below, by focusing on the operator algebra of the logical operators in the ground space of the model. By logical operators, we mean all possible operators acting on the ground space. We use the fact that if the ground space has dimension n, then the logical operators form the algebra Mat_n of all $n \times n$ complex matrices, and a maximal, abelian, diagonalizable subset among all logical operators has dimension n. Hence the dimension of the ground space can be determined from the dimension of either the full algebra or the Cartan subalgebra of the logical operators.

To determine the dimension of the operator algebras, we make use of the coupled layer condensation picture of the model. In particular, we start from a straightforward but redundant operator algebra A which is the tensor product of operators algebras coming from the decoupled doubled Ising layers. The layers are coupled through p-loop condensation. Correspondingly, we take the commutant M' of the condensate algebra M within A, obtaining the deconfined algebra. Moreover, the deconfined algebra is further restricted by the constraints coming from the Hamiltonian (cube terms in Ising cage-net). When the set of both types of constraints is modded out, we get a semisimple algebra PM', i.e. one with a block-diagonal form. The full logical operator algebra A_0 should be a matrix algebra, i.e. containing a single block. This structure will be recovered once we take into account the splitting of certain logical operators after condensation. This process is illustrated in Fig. 2.5.

2.3 GSD of the chiral Ising

The chiral Ising anyon model [69] ("chiral Ising" for short) is a 2D topological order whose properties such as GSD and anyon structure are well-known. As explained in Section 2.1, we can use chiral Ising to construct doubled Ising and hence Ising cage-

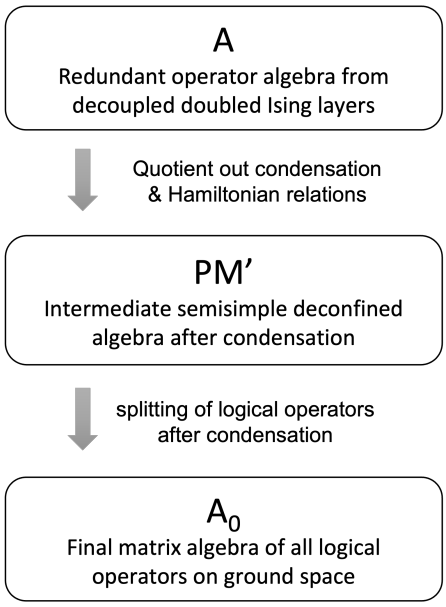

Figure 2.5: Procedure for determining the algebra of logical operators on the Ising cage-net ground space.

net. In this section, we review chiral Ising and calculate its GSD with an alternative method, namely the operator algebra approach. While this approach may seem over-complicated for this relatively simple model, we aim to set up the general formalism and present several useful mathematical statements, as this approach will be used in Section 2.7 for calculating the GSD of Ising cage-net.

There are three anyons in chiral Ising: 1, σ and ψ. This model can be obtained e.g. by gauging the $\mathbb{Z}_2$ fermion parity symmetry in a $p+ip$ superconductor. In this context, 1 is the vacuum, σ is the π gauge flux, and ψ is the gauge charge. The fusion rules are $\sigma \times \sigma = 1 + \psi$, $\sigma \times \psi = \sigma$, $\psi \times \psi = 1$. The F- and R-symbols can be found in Ref. [71]. The GSD of a 2D topological order on a torus is equal to its number of anyons, so the Ising anyon model has GSD = 3. This is equivalent to saying that the algebra of logical operators is $A_0 = \mathrm{Mat}_3$. Here, Mat_n is the set of all $n \times n$ complex matrices. In the operator algebra approach which we will discuss now, we treat A_0 as the more fundamental object, design a framework to compute A_0 without knowledge of the ground space $\mathcal{H}_0$, and view $\mathcal{H}_0$ as a representation space of A_0.

The starting point of the operator algebra approach is a set of logical operators. We require these operators to linearly span the vector space of all logical operators, but we don't require them to be linearly independent. For a 2D topological order on a

torus, we take these to be operators of the form

$$v(a,b,c) = \quad , \tag{2.4}$$

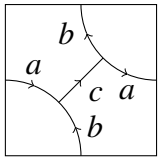

where a, b, c are anyons consistent with the fusion rules (for simplicity we assume no fusion multiplicity). We call such an operator an *elementary operator*. If $b = 1$ then we must have $a = c$, and we will sometimes use the short-hand notation $a_x = v(a, 1, a)$; similarly $b_y = v(1, b, b)$.

Of course, an elementary operator acts on the ground space $\mathcal{H}_0$ and has a matrix representation, but our discussion here does not rely on such a representation. Instead, we view the elementary operators as abstract objects. We can form a complex vector space A over the elementary operators, with formal addition and formal scalar multiplication. The vector space A has an additional operation called multiplication, defined for a pair of elementary operators by stacking one operator on top of the other and reducing the diagram to a sum of elementary operators using F and R symbols:

$$v(a,b,c)v(a',b',c') = \quad$$

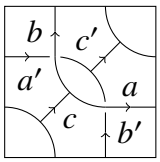

$$= \sum_{f,g} \sqrt{\frac{d_f d_g}{d_a d_{a'} d_b d_{b'}}} \quad$$

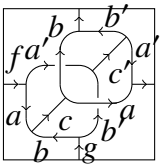

$$= \sum_{f,g,h} \lambda(f,g,h) v(f,g,h),$$

with some coefficients $\lambda(f, g, h)$. Here f, g and h are some anyons, and d_a is the quantum dimension of a. Going from the first line to the second line, we fused a with a' to get f, and b with b' to get g; going from the second line to the third line, we used F- and R-moves to transform the diagrams into elementary operators. In principle, we can compute $\lambda(f, g, h)$ for a general anyon theory, but in this paper we will only need some simple cases. For example, in chiral Ising we have

$$\psi_x \psi_y = v(\psi, 1, \psi) v(1, \psi, \psi) = -v(\psi, \psi, 1),$$

where the minus sign comes from $R_1^{\psi,\psi} = -1$. The multiplication has an identity $1 = v(1, 1, 1)$. We say that A is an *algebra*, which is a complex vector space equipped

with multiplication and a multiplicative identity (Definition 8 in Appendix 2.8 explains this concept more rigorously). If one views the elements of A as operators on $\mathcal{H}_0$, then the addition, scalar multiplication and multiplication are the usual matrix operations. However, we stress again that we would like to view A as a structure in its own right and not interpret it as a matrix algebra acting on a Hilbert space just yet.

For the chiral Ising, we have 10 elementary operators

$$\begin{aligned} &v(1,1,1), \quad && v(\psi,1,\psi),\\ &v(1,\psi,\psi), \quad && v(\psi,\psi,1),\\ &v(\sigma,1,\sigma), \quad && v(1,\sigma,\sigma),\\ &v(\sigma,\psi,\sigma), \quad && v(\psi,\sigma,\sigma),\\ &v(\sigma,\sigma,1), \quad && v(\sigma,\sigma,\psi). \end{aligned}$$

Therefore, $\dim(A) = 10$. However, we know that the algebra of logical operators should be $A_0 = \mathrm{Mat}_3$ which has $\dim(A_0) = 9$, so A is too large. This means that we need to reduce the redundancy in A by modding out some relations. Conveniently, this redundancy reduction turns out to be equivalent to acting on A by a projector P, which kills the subspace $(1-P)A$ and preserves its complement PA.

Before discussing where the relations come from, we want to first answer a question: How do we know whether we have found sufficiently many relations so that PA is small enough? For a topological or fractonic order, its algebra of logical operators should be Mat_n for some n. Conversely, a matrix algebra Mat_n has the property that no more redundancy can be modded out (Definition 10 and Lemma 11). Therefore, the redundancy reduction stops if and only if PA is a matrix algebra.

Furthermore, all of the algebras in the physical models in this paper have the additional property of being so-called semisimple.

Definition 1. An algebra A is *semisimple* if it can be written as a direct sum

$$A = A_1 \oplus \cdots \oplus A_m, \tag{2.5}$$

where each A_i is a matrix algebra.

The redundancy reduction amounts to finding a projector P that kills all but one A_i, and then the true algebra of logical operators is this A_i. The kernel of P consists of

operators that we identify with 0, so we are taking a "quotient" of A (see details in Appendix 2.8).

Given A, its decomposition (2.5) can be performed systematically, but for the case of chiral Ising in this section, we will first write down the result:

$$A = \mathrm{Mat}_3 \oplus \mathrm{Mat}_1. \tag{2.6}$$

A systematic derivation can be found in Section 2.4. In this decomposition, we have

$$\begin{aligned}\mathrm{Mat}_3 = \mathrm{span}\{&1+\psi_x, 1+\psi_y, 1+r,\\ &\sigma_x, \sigma_y, v(\sigma,\psi,\sigma), v(\psi,\sigma,\sigma),\\ &v(\sigma,\sigma,1), v(\sigma,\sigma,\psi)\},\\ \mathrm{Mat}_1 = \mathrm{span}\{&1-r\},\end{aligned}$$

where

$$r = \frac{1}{2}\left(1+\psi_x+\psi_y-\psi_x\psi_y\right). \tag{2.7}$$

The 9 spanning elements of Mat_3 are not very important, but the element r will be useful throughout this paper.

Given the decomposition (2.6), clearly we want to define the projector P such that $PA = \mathrm{Mat}_3$. However, if we didn't know that $A_0 = \mathrm{Mat}_3$ in the first place, then we would need to justify this choice of P. To do so, we note that A is obtained only using fusion rules, F-symbols and R-symbols, while further information such as the topology of the torus hasn't been fully utilized. Indeed, we can put a contractible σ-loop "around the corners" of the torus, reduce it to a sum of elementary operators on the one hand, and demand it be equal to the quantum dimension $\sqrt{2}$ of σ on the other hand. Using red lines for σ-strings and blue lines for ψ-strings, the reduction

to elementary operators is performed as follows:

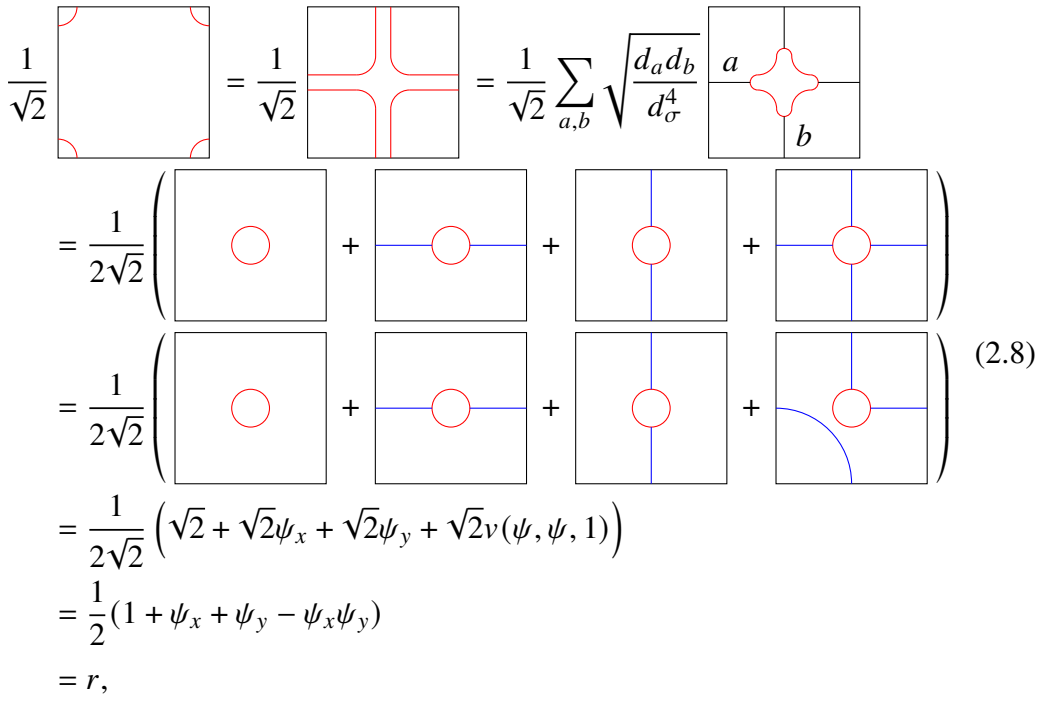

$$
\begin{aligned}
&= \frac{1}{2\sqrt{2}} \left(\quad + \quad + \quad + \quad \right) \\
&= \frac{1}{2\sqrt{2}} \left(\quad + \quad + \quad + \quad \right) \\
&= \frac{1}{2\sqrt{2}} \left(\sqrt{2} + \sqrt{2}\psi_x + \sqrt{2}\psi_y + \sqrt{2} v(\psi, \psi, 1) \right) \\
&= \frac{1}{2} (1 + \psi_x + \psi_y - \psi_x \psi_y) \\
&= r,
\end{aligned}
\tag{2.8}
$$

where we moved the $\sqrt{2}$ to the denominator. In this calculation, we first moved the σ-strings close together, and then fused the parallel σ-strings to obtain four outcomes (second line). The result is demanding $r = 1$. In other words, we identify $1 - r$ with 0 by taking the projector $P = (1 + r)/2$, which precisely kills $1 - r$. The same relation was also found in Ref. [72]. We can repeat the same calculation for a 1-loop or a ψ-loop "around the corners", but in the end we obtain tautological relations. Only non-abelian anyons can give non-trivial relations.

To conclude this section, we summarize the operator algebra approach as follows:

Protocol 2. Suppose we have a topological or fractonic order.

1. We take a set of logical operators that span the space of all logical operators but are not necessarily linearly independent.
2. We reduce the redundancy of these logical operators with F- and R-moves as much as possible. Then we take the formal algebra A over the remaining operators, which is a semisimple algebra. In a 2D topological order, if we take the operators $v(a, b, c)$ as in (2.4), then these operators have no such redundancy and there is no need for this step.
3. We find relations in A by physical argument. In a 2D topological order, the relations are given by loops of (non-abelian) anyons "around the corners". For

Ising cage-net, we will see that the relations are given by cage structures of non-abelian strings. We then mod out the relations by acting with the corresponding projector P. If PA is a matrix algebra, then the true algebra of logical operators is $A_0 = PA$. In Section 2.4, we will discuss a quick way to find P.

2.4 Structure of semisimple algebra

The correctness of the decomposition (2.6) can be checked by hand, but this is far from systematic. At the same time, we also do not have a systematic method for converting relations to projectors. In this section, we resolve these two issues by discussing the structure of a semisimple algebra, and provide an efficient way to compute projectors. Several statements in this section will be used in the calculations in later sections.

In the decomposition (2.5) of a semisimple algebra A, each component A_i has its own multiplicative identity P_i, called a primitive central projector of A.

Definition 3. An element $x \in A$ is *central* if $[x, y] = 0$ for all $y \in A$. The set of all central elements of A is the *center* of A, written as $Z(A)$. A central element $x \in Z(A)$ is a *central projector* if $x^2 = x$. A central projector x is *primitive* if for all central projector $y \in A$, we have $xy = 0$ or x.

The primitive central projectors P_i have the property that every central projector Q can be written as

$$Q = \sum_i \lambda_i P_i,$$

where $\lambda_i = 0$ or 1. If we represent A as block-diagonal matrices, then a central projector is the identity of several blocks, and a primitive one occupies exactly one block. It behaves like a projector in the usual sense when acting on A by left multiplication (equivalent to right multiplication and conjugation since Q is central).

In principle, given a basis $\{v_\alpha\}$ of A and structure constants $f^\gamma_{\alpha\beta}$ defined by

$$v_\alpha v_\beta = \sum_\gamma f^\gamma_{\alpha\beta} v_\gamma, \tag{2.9}$$

the central projectors are the solutions to the equations

$$\begin{aligned} [x, v_\alpha] &= 0 \text{ for all } \alpha, \\ x^2 &= x. \end{aligned} \tag{2.10}$$

If the solutions are $\{Q_k\}$, then the primitive ones form the subset $\{P_i\} \subset \{Q_k\}$ of maximal size such that $P_i P_j = 0$ for all $i \neq j$. We then obtain the decomposition (2.5) where $A_i = P_i A$.

Next, we discuss the conversion of relations into projectors. In this paper, the relations obtained from physical argument happen to all be central in A. It also happens that a simply linear rescaling is enough to convert all the relations into central projectors, e.g. the rescaling of $1 - r$ into $(1 - r)/2$ for chiral Ising. Suppose that we have relations $Q_1, \ldots, Q_m$ where each Q_k is a central projector. Then the overall projector is

$$P = (1 - Q_1) \cdots (1 - Q_m). \tag{2.11}$$

Such a projector can also be constructed without the assumption that Q_k is central, and this construction is discussed in Appendix 2.8.

Following this procedure, we find the primitive central projectors of chiral Ising to be

$$P_1 = \frac{1}{2}(1 + r), \; P_2 = \frac{1}{2}(1 - r).$$

Applying (2.11) with $Q = P_2$, we find

$$PA = (1 - P_2)A = P_1 A = \mathrm{Mat}_3,$$

which is the matrix algebra we want.

In the remaining sections, (2.11) will be used constantly for computing projectors.

2.5 Doubled-Ising to toric code: an operator algebra view of anyon condensation

Ising cage-net is obtained via p-loop condensation, an example of Bose-Einstein condensation. In this section, we discuss the topic of condensation in the operator algebra approach by studying the simple example of condensation in doubled Ising.

As explained in Section 2.1, doubled Ising is a stack of two copies of chiral Ising, whose anyons are 1, σ, ψ and 1, $\bar{\sigma}$, $\bar{\psi}$, respectively. Now suppose we want to condense the boson $\psi\bar{\psi}$. For an anyon to remain deconfined upon condensation, it must braid trivially with $\psi\bar{\psi}$. Such anyons are $1 = \psi\bar{\psi}$, $\psi = \bar{\psi}$ and $\sigma\bar{\sigma}$. Furthermore, $\sigma\bar{\sigma}$ is no longer a simple particle, but instead "splits" into two anyons $\sigma\bar{\sigma} = e + m$. To see why, note that $\sigma\bar{\sigma}$ is the fusion product of two Majorana modes and hence a (complex) fermion mode. The parity p of this fermion mode can be 0 (unfilled) or 1 (filled), and braiding with σ or $\bar{\sigma}$ switches the value of p, so p is not a good

quantum number in doubled Ising. However, if $\psi\bar{\psi}$ is condensed then both σ and $\bar{\sigma}$ are confined, and therefore p becomes a good quantum number that distinguishes the unfilled fermion mode (anyon e) from the filled (anyon m). The resulting topological order is the toric code [73].

It turns out that the operator algebra approach provides a nice description of condensation and, in particular, the "splitting" of anyons. To begin with, we follow Steps 1 and 2 of Protocol 2 to obtain a semisimple algebra A with $\dim(A) = 100$. Since doubled Ising is two copies of chiral Ising, we can find the decomposition of A by taking a tensor product:

$$\begin{aligned} A &= (\mathrm{Mat}_3 \oplus \mathrm{Mat}_1)^{\otimes 2} \\ &= \mathrm{Mat}_9 \oplus \mathrm{Mat}_3 \oplus \mathrm{Mat}_3 \oplus \mathrm{Mat}_1. \end{aligned} \tag{2.12}$$

The quantum dimensions of σ and $\bar{\sigma}$ give us two relations $r = 1$ and $\bar{r} = 1$, where

$$\begin{aligned} r &= \frac{1}{2}\left(1 + \psi_x + \psi_y - \psi_x\psi_y\right), \\ \bar{r} &= \frac{1}{2}\left(1 + \bar{\psi}_x + \bar{\psi}_y - \bar{\psi}_x\bar{\psi}_y\right). \end{aligned}$$

By (2.11), these relations give rise to a projector

$$P = \frac{1}{4}(1 + r)(1 + \bar{r}),$$

and $PA = \mathrm{Mat}_9$ is the correct (ground space) operator algebra of doubled Ising. Of course, $\sigma\bar{\sigma}$ is also a non-abelian anyon, and it gives a relation $r\bar{r} = 1$, but we don't need to consider this relation separately because $r = 1 = \bar{r}$ already implies $r\bar{r} = 1$.

To condense $\psi\bar{\psi}$, we want to identify $\psi_x\bar{\psi}_x$ and $\psi_y\bar{\psi}_y$ with 1 and understand the consequence of doing so. Let M be the subalgebra of A generated by $\psi_x\bar{\psi}_x$ and $\psi_y\bar{\psi}_y$. M is an *abelian* subalgebra since we have $[x, y] = 0$ for all $x, y \in M$. Upon condensation, the logical operators that remain "deconfined" are those that commute with M. Such deconfined operators form the *commutant* of M, which is a semisimple subalgebra of A defined as

$$M' = \{x \in A \mid [x, y] = 0 \text{ for all } y \in M\}.$$

Since M is abelian, we have $M \subset M'$. To be precise, M' is spanned by elementary operators $v(a, b, c)$ where a and b take values in $\{1, \psi, \bar{\psi}, \psi\bar{\psi}, \sigma\bar{\sigma}\}$. A straightforward calculation shows $\dim(M') = 28$. By analyzing the primitive central projectors of M' using (2.10), we can decompose M' as

$$M' = (\mathrm{Mat}_3 \oplus 3\mathrm{Mat}_2) \oplus 3\mathrm{Mat}_1 \oplus 3\mathrm{Mat}_1 \oplus \mathrm{Mat}_1, \tag{2.13}$$

where $3\mathrm{Mat}_2$ means $\mathrm{Mat}_2 \oplus \mathrm{Mat}_2 \oplus \mathrm{Mat}_2$, etc. Here, the summands are organized in correspondence with the summands in (2.12), i.e. $(\mathrm{Mat}_3 \oplus 3\mathrm{Mat}_2)$ is a subalgebra of the Mat_9 in (2.12), the first $3\mathrm{Mat}_1$ is a subalgebra of the first Mat_3 in (2.12), and so on.

Next, we need to mod out all relations we know. Firstly, we have the quantum dimension of $\sigma\bar{\sigma}$, which demands $r\bar{r} = 1$. By (2.11), this gives a projector

$$P_{12} = \frac{1}{2}(1 + r\bar{r}).$$

We chose the notation P_{12} for consistency with the discussion in Section 2.6. Now we note that

$$P_{12}A = \mathrm{Mat}_9 \oplus \mathrm{Mat}_1,$$

since r and $\bar{r}$ both act as $+1$ on Mat_9, and both act as -1 on Mat_1. Therefore, by restricting the action of $(1 + r\bar{r})/2$ to M', we have

$$P_{12}M' = (\mathrm{Mat}_3 \oplus 3\mathrm{Mat}_2) \oplus \mathrm{Mat}_1.$$

Secondly, we have the condensation which demands $\psi_x\bar{\psi}_x = 1$ and $\psi_y\bar{\psi}_y = 1$. Again by (2.11), these two relations give a projector

$$P_{\mathrm{c}} = \frac{1}{4}(1 + \psi_x\bar{\psi}_x)(1 + \psi_y\bar{\psi}_y),$$

where the subscript "c" stands for "condensation". Thus the overall projector is

$$P = P_{\mathrm{c}}P_{12},$$

and we need to check the action of P_{c} on $(\mathrm{Mat}_3 \oplus 3\mathrm{Mat}_2)$ and on Mat_1. The latter is straightforward: Mat_1 is spanned by $(1 - r)(1 - \bar{r})$, and explicit calculation shows

$$P_{\mathrm{c}}(1 - r)(1 - \bar{r}) = (1 - r)(1 - \bar{r}).$$

Therefore, Mat_1 is in PM'. On the other hand, let $Q_0 = (1+r)(1+\bar{r})/4$ be the central projector that projects A onto Mat_9. Since both P_{c} and Q_0 are central projectors, so is $P_{\mathrm{c}}Q_0$, and we also claim that $P_{\mathrm{c}}Q_0$ is primitive. This is a consequence of the following lemma:

Lemma 4. Let B be a matrix algebra, N an abelian subalgebra of B, and N' the commutant of N. Then we have $Z(N') = N$.

It is easy to see that $N \subset Z(N')$, and Lemma 4 says that the two are actually equal. Technically, N must satisfy another condition, and Lemma 13 in Appendix 2.8 explains this point more rigorously. Applying Lemma 4 with $B = Q_0 A$ and $N = Q_0 M$, we know that $Z(Q_0 M')$ is generated by $\psi_x \bar{\psi}_x Q_0$ and $\psi_y \bar{\psi}_y Q_0$. It is then straightforward to use the prescription in Section 2.4 to find the primitive projectors from the central elements, and indeed $P_c Q_0$ is one of them. Thus we know that $P_c Q_0 M'$ is a matrix algebra, and we need to determine whether it is Mat_3 or one of the three copies of Mat_2. For this purpose, we note that for any operator $x \in A$, we can represent xQ_0 as a 9×9 matrix $\rho_9(xQ_0)$, or $\rho_9(x)$ for short. The subscript l in ρ_l indicates the matrix dimension. A systematic way to determine this representation ρ_9 can be found in Appendix 2.8, but here we will start with a 3×3 matrix representation ρ_3 of operators in chiral Ising:

$$\begin{aligned} \rho_3(\psi_x) &= \begin{pmatrix} 1 & & \\ & 1 & \\ & & -1 \end{pmatrix}, \ \rho_3(\sigma_x) = \begin{pmatrix} 0 & \sqrt{2} & 0 \\ \sqrt{2} & 0 & 0 \\ 0 & 0 & 0 \end{pmatrix}, \\ \rho_3(\psi_y) &= \begin{pmatrix} 1 & & \\ & -1 & \\ & & 1 \end{pmatrix}, \ \rho_3(\sigma_y) = \begin{pmatrix} 0 & 0 & \sqrt{2} \\ 0 & 0 & 0 \\ \sqrt{2} & 0 & 0 \end{pmatrix}. \end{aligned} \tag{2.14}$$

The correctness of this representation can be confirmed by hand or by following the discussion in Appendix 2.8. The operators in Mat_9 can be obtained by tensoring the above matrices. In particular, $\rho_9(Q_0)$ is the 9×9 identity, and we find $\rho_9(P_c Q_0)$ to be a diagonal matrix

$$\rho_9(P_c Q_0) = \mathrm{diag}(1, 0, 0, 0, 1, 0, 0, 0, 1). \tag{2.15}$$

Since $\mathrm{tr}(\rho_9(P_c Q_0)) = 3$, we have $P_c Q_0 M' = \mathrm{Mat}_3$. To summarize, we have

$$PM' = \mathrm{Mat}_3 \oplus \mathrm{Mat}_1, \tag{2.16}$$

where the projector P accounts for deconfined anyons and the condensation condition.

The bottom line of (2.16) is that even after modding out all the relations we know, we still do not obtain a matrix algebra. However, we know that the algebra of logical operators must be a matrix algebra, so we need to do something to PM'. For this purpose, we visualize PM' as block-diagonal matrices embedded in Mat_4:

$PM' =$ 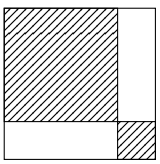 . (2.17)

We have the following observation: The splitting of $\sigma\bar{\sigma}$ precisely "fills the blanks" in (2.17) to turn $\mathrm{Mat}_3 \oplus \mathrm{Mat}_1$ into Mat_4.

To justify this observation, we will work out a 4×4 matrix representation ρ_4 of, say, e_x and compare it with the known result from the toric code. By (2.15), the Mat_3 block of an element $x \in PM'$ is obtained by taking rows and columns 1, 5 and 9 from $\rho_9(x)$. On the other hand, the Mat_1 block of $x \in PM'$ is determined by its action on the generator $(1-r)(1-\bar{r})$ of Mat_1. For example,

$$\begin{aligned} \psi_x(1-r)(1-\bar{r}) &= -(1-r)(1-\bar{r}), \\ \sigma_x\bar{\sigma}_x(1-r)(1-\bar{r}) &= 0. \end{aligned}$$

Using this method, we find the ρ_4 representations of some operators in PM' to be

$$\rho_4(\psi_x) = \begin{pmatrix} 1 & & & \\ & 1 & & \\ & & -1 & \\ & & & -1 \end{pmatrix}, \quad \rho_4(\sigma_x\bar{\sigma}_x) = \begin{pmatrix} 0 & 2 & 0 & 0 \\ 2 & 0 & 0 & 0 \\ 0 & 0 & 0 & 0 \\ 0 & 0 & 0 & 0 \end{pmatrix},$$

$$\rho_4(\psi_y) = \begin{pmatrix} 1 & & & \\ & -1 & & \\ & & 1 & \\ & & & -1 \end{pmatrix}, \quad \rho_4(\sigma_y\bar{\sigma}_y) = \begin{pmatrix} 0 & 0 & 2 & 0 \\ 0 & 0 & 0 & 0 \\ 2 & 0 & 0 & 0 \\ 0 & 0 & 0 & 0 \end{pmatrix}.$$

We want to use physical argument to find $\rho_4(e_x)$. We have equations

$$\begin{aligned} \rho_4(e_x)^\dagger &= \rho_4(e_x), \\ (1+\rho_4(\psi_x))\rho_4(e_x) &= \rho_4(\sigma_x\bar{\sigma}_x), \\ \rho_4(e_x)\rho_4(\psi_y) &= -\rho_4(\psi_y)\rho_4(e_x), \\ \rho_4(e_x)^2 &= 1. \end{aligned}$$

Line 1 says that e is its own antiparticle; line 2 comes from $\psi \times e = m$ and $\sigma\bar{\sigma} = e+m$; line 3 says that e and ψ braid with a -1 phase; line 4 comes from the fusion rule of e. The most general solution is

$$\rho_4(e_x) = \begin{pmatrix} 0 & 1 & & \\ 1 & 0 & & \\ & & 0 & e^{i\theta} \\ & & e^{-i\theta} & 0 \end{pmatrix}.$$

As expected, $\rho_4(e_x)$ has entries $e^{\pm i\theta}$ in the "blank" areas of (2.17). There is no way to fix θ, since conjugation by

$$U = \begin{pmatrix} 1 & & & \\ & 1 & & \\ & & 1 & \\ & & & e^{i\phi} \end{pmatrix}$$

acts trivially on $\mathrm{Mat}_3 \oplus \mathrm{Mat}_1$ but non-trivially on Mat_4, mapping θ to $\theta \pm \phi$. Without loss of generality, we choose $\theta = 0$. This gives

$$\rho_4(e_x) = \begin{pmatrix} 0 & 1 & & \\ 1 & 0 & & \\ & & 0 & 1 \\ & & 1 & 0 \end{pmatrix}, \quad \rho_4(m_x) = \begin{pmatrix} 0 & 1 & & \\ 1 & 0 & & \\ & & 0 & -1 \\ & & -1 & 0 \end{pmatrix}.$$

Using the same method while demanding $\rho_4(e_y)$ commute with $\rho_4(e_x)$, we find

$$\rho_4(e_y) = \begin{pmatrix} 0 & 0 & 1 & 0 \\ 0 & 0 & 0 & 1 \\ 1 & 0 & 0 & 0 \\ 0 & 1 & 0 & 0 \end{pmatrix}, \quad \rho_4(m_y) = \begin{pmatrix} 0 & 0 & 1 & 0 \\ 0 & 0 & 0 & -1 \\ 1 & 0 & 0 & 0 \\ 0 & -1 & 0 & 0 \end{pmatrix}.$$

One may check that these indeed obey the (ground space) operator algebra of the toric code. Moreover, they generate matrices such as

$$\begin{pmatrix} 0 & 0 & 0 & 1 \\ 0 & 0 & 0 & 0 \\ 0 & 0 & 0 & 0 \\ 0 & 0 & 0 & 0 \end{pmatrix} = \frac{1}{4}\rho_4(\sigma_x\bar{\sigma}_x)[\rho_4(e_y) - \rho_4(m_y)],$$

and hence all other matrices with entries in the "blank" areas of (2.17).

To conclude this section, we summarize condensation in the operator algebra approach as follows:

Protocol 5. Let A be the semisimple algebra of a topological or fractonic order, and suppose that $\{a\}$ is a set of bosons to be condensed.

1. We define M as the subalgebra of logical operators of $\{a\}$. If $\{a\}$ can be condensed simultaneously, then M is always abelian.

2. Let M' be the commutant of M. We define P as the projector due to the condensation condition, relations due to deconfined anyons as well as relations from other physical arguments. For Ising cage-net, the physical arguments will come from the plaquette and cage terms of the Hamiltonian (2.3). We then take the algebra PM'.
3. If the semisimple algebra

$$PM' = \mathrm{Mat}_{d_1} \oplus \cdots \oplus \mathrm{Mat}_{d_m}$$

has more than one component, then certain operators must split. The result of splitting is a matrix algebra

$$A_0 = \mathrm{Mat}_{d_1+\cdots+d_m},$$

which is obtained by "filling the blanks" in the matrix representation of PM'. The correctness of this operation can be confirmed manually for all the 2D models in this paper, and we conjecture that this holds for all topological or fractonic orders.

2.6 GSD of the one-foliated Ising cage-net

We will discuss one more 2D topological order in this section before going to Ising cage-net in Section 2.7. In particular, we will show a method of computing the GSD using a Cartan subalgebra, which is very convenient when applied to Ising cage-net.

The model we want to discuss is called the one-foliated Ising cage-net model ("1-F Ising" for short), which is constructed as follows: We take a stack of $2L$ copies of chiral Ising, and condense the boson $\Psi = \psi(1) \times \cdots \times \psi(2L)$, where $\psi(k)$ is the ψ particle from the kth layer. The chirality of these copies of chiral Ising does not affect the GSD. The condensation of doubled Ising into the toric code in Section 2.5 is a special case of this construction with $L = 1$.

In the limit $L \to \infty$, 1-F Ising can be viewed as a fracton model, whose partially mobile excitations are planons. It is related to Ising cage-net as follows: In Ising cage-net, let S_x be a set of principal edges l_x related to each other by translation in the z direction (green edges in Fig. 2.6). Then the operator

$$\prod_{l_x \in S_x} V_{l_x}, \tag{2.18}$$

where V_{l_x} is a condensation operator defined in (2.2), creates a pair of $\psi\bar{\psi}$ anyons in each xy plane. Therefore, Ψ in the xy plane is part of the condensate in Ising cage-

net. So are Ψ in the yz and zx planes. In this sense, 1-F Ising is the "one-foliated" version of Ising cage-net, while Ising cage-net is "three-foliated".

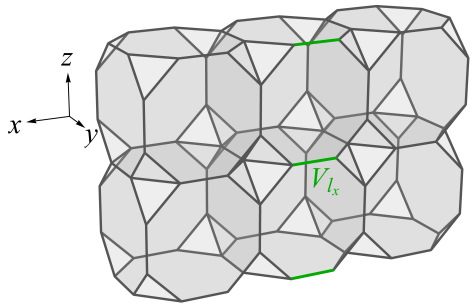

Figure 2.6: 1-F Ising obtained from layers of doubled Ising on a square-octagon lattice, similar to the construction of Ising cage-net. Each plane is a layer of doubled Ising. The product of V_{l_x} on the green edges (the set S_x in (2.18)) creates a pair of $\psi\bar{\psi}$ in each xy plane. If we condense the Ψ particles created this way, then we obtain 1-F Ising together with decoupled layers of doubled Ising in the yz and zx planes.

GSD from anyon counting

Since the 1-F Ising is a 2D topological order, its GSD can be obtained by counting anyons. In order for an anyon to be deconfined upon condensation, it must contain an even number of $\sigma's$ in order to braid trivially with $\Psi = \psi_1 \times \cdots \times \psi_{2L}$. The only such particles are ones where there are an even number of layers with σ. Additionally, we can attach ψ to any layer where there is no σ, since that does not affect the braiding with Ψ. The condensation of Ψ identifies some pairs of anyons with each other, which reduces the number of distinct anyons. Finally, the anyon $\Sigma = \sigma(1) \times \cdots \times \sigma(2L)$ splits into two simple particles $\Sigma = e + m$ since the overall fermion parity of Σ is a good quantum number. Another way to see this is to note that $\Sigma \times \Sigma = 1 + \Psi + \cdots$, so the presence of two identity channels implies that Σ splits into two particles. These conditions give constraints on a label $a(1) \times \cdots \times a(2L)$ of an anyon.

We now count the number of such labelings. If we choose $2k$ layers $i_1, \ldots, i_{2k}$ to attach σ to, where $k = 0, \ldots, L-1$, then there are $(2L - 2k)$ places left to attach ψ. It would seem, therefore, that there are 2^{2L-2k} inequivalent ways to attach ψ to the layers. However, $\Psi = 1$ reduces the number of distinct labelings by a factor of 2. For example, consider the case where $L = 4$. Here, the particles $\sigma_1\sigma_2\psi_3$ and $\sigma_1\sigma_2\psi_4$ are equivalent, since $\sigma_1\sigma_2\psi_3 = \sigma_1\sigma_2 \times \psi_1\psi_2\psi_3 = \sigma_1\sigma_2 \times \psi_4$ using

$\Psi = \psi_1\psi_2\psi_3\psi_4 = 1$. This generalizes straightforwardly to an arbitrary number of layers and σ's, halving the number of anyons in the theory. Therefore, there are $\binom{2L}{2k}2^{2L-2k-1}$ inequivalent ways to choose $2k$ layers to place σ and attach 1's or ψ's to the remaining layers. The case where $k = L$ needs to be considered separately. In this case, the anyon of interest is Σ, which splits into e and m. Thus the total number of anyons in the theory (equal to the GSD) is

$$\begin{aligned}\text{GSD} &= \sum_{k=0}^{L-1}\binom{2L}{2k}2^{2L-2k-1} + 2 \\ &= \sum_{k=0}^{L}\binom{2L}{2k}2^{2L-2k-1} + 2 - \frac{1}{2},\end{aligned}$$

where the +2 accounts for the $k = L$ case. To evaluate this, we use the binomial theorem

$$\begin{aligned}(1+x)^{2L} + (1-x)^{2L} &= \sum_{j=0}^{2L}\binom{2L}{j}\left(x^{2L-j} + (-x)^{2L-j}\right) \\ &= 2\sum_{k=0}^{L}\binom{2L}{2k}x^{2L-2k}.\end{aligned}$$

This can be used to find the GSD:

$$\begin{aligned}\text{GSD} &= \sum_{k=0}^{L}\binom{2L}{2k}2^{2L-2k-1} + 2 - \frac{1}{2} \\ &= \frac{1}{4}(1+2)^{2L} + \frac{1}{4}(1-2)^{2L} + \frac{3}{2} \\ &= \frac{1}{4}\left(9^L + 7\right). \qquad (2.19)\end{aligned}$$

The same result was obtained by K. Slagle, D. Aasen, D. Williamson and W. Shirley [74].

GSD from Cartan subalgebra

We now try to reproduce (2.19) using the operator algebra approach. Protocol 5 is based on the full algebra of 1-F Ising, but we delay this calculation to Section 2.6. Instead, here we will compute the GSD using a so-called Cartan subalgebra of the full algebra.

Definition 6. A subalgebra C of an algebra A is a *Cartan subalgebra* if it is abelian and maximal. Abelian means that $[x, y] = 0$ for all $x, y \in C$; maximal means that if any subalgebra $C' \subset A$ is abelian and $C \subset C'$, then $C' = C$.

Note that this definition is not entirely rigorous mathematically: There is another condition on C which we did not mention, and this condition holds for the choice of C that we will use later. Definition 15 in Appendix 2.8 explains this extra condition.

A Cartan subalgebra is related to the GSD by the following lemma:

Lemma 7. Let A_0 be a matrix algebra, $C_0 \subset A_0$ a Cartan subalgebra. Then $\dim(C_0)^2 = \dim(A_0)$. In particular, if A_0 is a (ground space) operator algebra, then $\mathrm{GSD} = \dim(C_0)$.

To understand this lemma with an example, take C_0 to be the set of diagonal matrices in A_0. The lemma is obvious in this case.

For $2L$ copies of chiral Ising with semisimple algebra

$$A = (\mathrm{Mat}_3 \oplus \mathrm{Mat}_1)^{\otimes 2L},$$

we have a convenient choice of a Cartan subalgebra C, which is spanned by the elementary operators with no σ. To compute the GSD, we want to understand the transition from C to C_0. Our approach will be similar to Steps 1 and 2 of Protocol 5, although we will adapt these steps to fit with the Cartan subalgebra. Let M be the subalgebra of A generated by Ψ_x and Ψ_y (the condensate). In the commutant M' of M, we have central projectors

$$P_{\mathrm{c}} = \frac{1}{4}(1+\Psi_x)(1+\Psi_y) \tag{2.20}$$

due to condensation, and

$$P_{ij} = \frac{1}{2}(1+r(i)r(j)) \tag{2.21}$$

due to deconfined anyons $\sigma(i)\sigma(j)$, where $1 \le i < j \le 2L$ and

$$r(i) = \frac{1}{2}\left(1+\psi_x(i)+\psi_y(i)-\psi_x(i)\psi_y(i)\right).$$

Although there are also non-abelian anyons consisting of more than two σ's and possibly ψ's, for the purpose of constructing projectors it suffices to only consider pairs of σ's. This is because e.g. $\sigma(1)\sigma(2)\sigma(3)\sigma(4)$ gives a relation $r(1)r(2)r(3)r(4) = 1$, but this is already implied by $r(1)r(2) = 1$ and $r(3)r(4) = 1$.

From this point on, we will focus only on the Cartan subalgebra. Importantly, in this specific case we have $C \subset M'$, and the central projectors P_{c} and P_{ij} all map C to C since they also contain no σ. Meanwhile, we can argue physically that splitting

does not enlarge the Cartan subalgebra. This is because the braiding of Σ with e.g. $\psi(1)$ gives a -1 phase and thus the same holds for the anyons e and m split from Σ. Therefore, the entirety of C_0 can be obtained by projection on C. In other words, we have $C_0 = PC$, where

$$P = P_{\mathrm{c}} \prod_{i<j} P_{ij}. \tag{2.22}$$

Since P is a projector, we have

$$\mathrm{GSD} = \dim(PC) = \mathrm{tr}(P).$$

We stress that the underlying vector space here is C, and that we are taking the trace of the action of P on C.

To find $\mathrm{tr}(P)$, we note that in principle, we can write

$$P = \sum_{a,b} \mu(a,b) v(a,b,a\times b), \tag{2.23}$$

where neither a nor b contains any σ (and hence $a \times b$ is unique), and $\mu(a,b)$ are some coefficients. We then observe that when $v(c,d,c\times d) \in C$ is multiplied by $v(a,b,a\times b)$ in (2.23), the result

$$\pm v(a\times c, b\times d, a\times b\times c\times d)$$

is never proportional to $v(c,d,c\times d)$ unless $a = b = 1$. As a result, only $v(1,1,1)$ contributes to $\mathrm{tr}(P)$, so we only need to find the coefficient $\mu(1,1)$. For this purpose, we need to expand (2.22). Firstly, we use $r(i)^2 = 1$ to obtain

$$\begin{aligned}\prod_{i<j} P_{ij} &= \frac{1}{2^{2L-1}} \sum_{k=0}^{L} \prod_{i_1<\cdots<i_{2k}} r(i_1)\cdots r(i_{2k}) \\ &= \frac{1}{2^{2L}} \left[\prod_{i=1}^{2L} (1+r(i)) + \prod_{i=1}^{2L} (1-r(i)) \right].\end{aligned}$$

The first line is a sum of all products of an even number of $r(i)$'s; the second line can be interpreted as forcing the $r(i)$'s to be all $+1$ or all -1, which is a consequence of forcing each pair of the $r(i)$'s to be both $+1$ or both -1 due to $\{P_{ij}\}$. Thus

$$\begin{aligned}P = \frac{1}{4}(1+\Psi_x+\Psi_y+\Psi_x\Psi_y) \\ \times \frac{1}{2^{2L}} \left[\prod_{i=1}^{2L} (1+r(i)) + \prod_{i=1}^{2L} (1-r(i)) \right].\end{aligned}$$

Now since

$$1 + r(i) = \frac{3}{2} + \frac{1}{2}\psi_x(i) + \frac{1}{2}\psi_y(i) - \frac{1}{2}\psi_x(i)\psi_y(i),$$
$$1 - r(i) = \frac{1}{2} - \frac{1}{2}\psi_x(i) - \frac{1}{2}\psi_y(i) + \frac{1}{2}\psi_x(i)\psi_y(i),$$

the only four terms in the expansion of $\prod_i(1 + r(i))$ that combines with one of 1, Ψ_x, Ψ_y and $\Psi_x\Psi_y$ to contribute to $\mu(1, 1)$ are

$$\left(\frac{3}{2}\right)^{2L}, \prod_i\left(\frac{1}{2}\psi_x(i)\right), \prod_i\left(\frac{1}{2}\psi_y(i)\right), \prod_i\left(-\frac{1}{2}\psi_x(i)\psi_y(i)\right).$$

Summing these up, we find that the contribution of the $\prod_i(1 + r(i))$ part to $\mu(1, 1)$ is $\left(9^L + 3\right)/2^{4L+2}$. Similarly, the contribution of the $\prod_i(1 - r(i))$ part is $4/2^{4L+2}$. Combining these together, we obtain

$$\mathrm{GSD} = \mathrm{tr}(P) = 2^{4L}\mu(1, 1) = \frac{1}{4}\left(9^L + 7\right),$$

where we used the fact that $\dim(C) = 2^{4L}$.

This calculation is almost entirely combinatorial and straightforward. However, it is also highly specific to simple examples such as Ising – it relies on a nice Cartan subalgebra which is fixed by the central projectors and cannot be enlarged by splitting due to physical arguments.

GSD from full algebra

Finally for the discussion of 1-F Ising, we compute its GSD using Protocol 5.

Again, we take M to be the subalgebra of A generated by Ψ_x and Ψ_y, and M' the commutant of M. We want to find PM' where P is given by (2.22). We will not try to decompose M' into matrix algebras like we did for doubled Ising in Section 2.5, since most of the components of A will be killed by the central projectors P_{ij}, just like the two copies of Mat_3 in (2.12). Instead, we will first discuss the action of P_{ij} on A, and then apply P_c. To start with, we have

$$\prod_{i<j} P_{ij}A = B_0 \oplus B_1,$$

where $B_0 = \mathrm{Mat}_{9^L}$ and $B_1 = \mathrm{Mat}_1$. This is because $\{P_{ij}\}$ forces the $r(i)$'s to be all $+1$ or all -1. As a result, we have

$$\prod_{i<j} P_{ij}M' \subset B_0 \oplus B_1,$$

so we need to find the action of P_c on $(B_0 \oplus B_1) \cap M'$.

For the $B_1 \cap M'$ part, we know that $B_1 \subset Z(A)$ since B_1 is a 1×1 block. Thus $B_1 \cap M' = B_1$. Each of $\psi_x(i)$ and $\psi_y(i)$ acts on B_1 as -1, so P_c preserves B_1. We conclude that $P_c(B_1 \cap M') = \mathrm{Mat}_1$.

For the $B_0 \cap M'$ part, we will repeat what we did in Section 2.5 for $\mathrm{Mat}_3 \oplus 3\mathrm{Mat}_2$, and use a matrix representation of P_c to determine its action. Let

$$Q_0 = \frac{1}{2^{2L}} \prod_i (1 + r(i))$$

be the central projector that projects onto B_0. By Lemma 4, the central projector $P_c Q_0$ is primitive, and hence the algebra $P_c Q_0 M'$ is a matrix algebra. On B_0, the action of operators such as P_c has representation ρ_{9^L}. Thus we have $P_c Q_0 M' = \mathrm{Mat}_n$ where $n = \mathrm{tr}(\rho_{9^L}(P_c Q_0))$. To find n, we use

$$\begin{aligned} n &= \dim(\text{eigenspace } \rho_{9^L}(P_c) = 1) \\ &= \dim(\text{eigenspace } \rho_{9^L}(\Psi_x) = \rho_{9^L}(\Psi_y) = +1). \end{aligned}$$

Let D_{2L}^{st}, where s, t can be $+$ or $-$, be the dimension of the common eigenspace $\{w\}$ of $\rho_{9^L}(\Psi_x)$ and $\rho_{9^L}(\Psi_y)$ where $\rho_{9^L}(\Psi_x)w = sw$ and $\rho_{9^L}(\Psi_y) = tw$ (i.e. $\pm w$). From the representation ρ_3 of ψ_x and ψ_y in (2.14), we find

$$\begin{aligned} D_{2L}^{++} &= \frac{1}{4}\left(9^L + 3\right), \\ D_{2L}^{+-} = D_{2L}^{-+} &= D_{2L}^{--} = \frac{1}{4}\left(9^L - 1\right). \end{aligned} \tag{2.24}$$

We will show the calculation of D_{2L}^{+-} as an example. Let $\{u_1, u_2, u_3\}$ be the standard basis for $\mathbb{C}^3$, and

$$w = u_1^{\otimes k_1} \otimes u_2^{\otimes k_2} \otimes u_3^{\otimes k_3}.$$

In order for $\rho_{9^L}(\Psi_x)w = +w$ and $\rho_{9^L}(\Psi_y)w = -w$, according to (2.14), we must have k_3 odd, k_2 even, and hence k_1 odd. The number of such combinations of (k_1, k_2, k_3) satisfying $k_1 + k_2 + k_3 = 2L$ can be found using the multinomial theorem:

$$\begin{aligned} D_{2L}^{+-} &= \frac{1}{4}\left[(1+1+1)^{2L} - (1+1-1)^{2L}\right. \\ &\qquad \left. +(1-1+1)^{2L} - (1-1-1)^{2L}\right] \\ &= \frac{1}{4}\left(9^L - 1\right). \end{aligned}$$

Using (2.24), we find $\mathrm{tr}(\rho_{9^L}(P_c Q_0)) = D_{2L}^{++} = \left(9^L + 3\right)/4$. Although here we only made use of D_{2L}^{++}, the other D's will be used in Section 2.7.

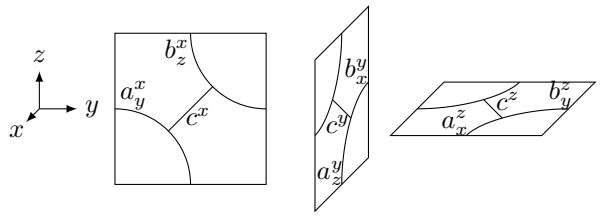

Figure 2.7: Constituents $v^x(a_y^x, b_z^x, c^x)$, $v^y(a_z^y, b_x^y, c^y)$ and $v^z(a_x^z, b_y^z, c^z)$ of an elementary operator in Ising cage-net. Arrows are not drawn since in Ising cage-net, every particle is its own antiparticle.

Putting the $B_0 \cap M'$ and $B_1 \cap M'$ parts together, we conclude that

$$PM' = \mathrm{Mat}_{(9^L+3)/4} \oplus \mathrm{Mat}_1 .$$

This is a semisimple algebra. Similar to what we did in Section 2.5 for condensation in doubled Ising, we can also find matrix representations of e_x, m_x, e_y and m_y and confirm that they have non-zero entries in the "blank" areas of PM', but we omit this calculation here. The semisimple algebra then turns into a matrix algebra

$$A_0 = \mathrm{Mat}_{(9^L+7)/4},$$

and GSD $= \left(9^L + 7\right)/4$ as expected.

2.7 GSD of the Ising cage-net

In this section, we compute the GSD of Ising cage-net, first using a Cartan subalgebra, and then using the full algebra.

We consider a system where we stack L_x, L_y and L_z layers of doubled Ising in the x, y and z directions, respectively. The elementary operators here are products of the 2D elementary operators $v^x(a_y^x, b_z^x, c^x)$ in the yz planes, $v^y(a_z^y, b_x^y, c^y)$ in the zx planes, and $v^z(a_x^z, b_y^z, c^z)$ in the xy planes (Fig. 2.7). We will also use notations such as $\psi_y^x(i)$ to denote the string operator of ψ from the ith plane orthogonal to the x direction (i.e. a yz plane) traversing the y direction. To obtain Ising cage-net from these decoupled layers, we need to condense $\psi\bar{\psi}$ p-loops as discussed in Section 2.1. Since our approach uses the operator algebra on the ground space, we need to combine the condensation operators V_{l_μ} defined in (2.2) into a logical operator (of the decoupled layers). An example of such a logical operator is shown in Fig. 2.8 (a), which looks like a "net" orthogonal to the z direction. We call it a Ψ-net and denote it by Ψ^z. Explicitly, if T^z is a set of principal edges l_z related to

each other by translation in the x and y directions (red edges in Fig. 2.9), then

$$\Psi^z = \prod_{l_z \in T^z} V_{l_z} = \prod_{i=1}^{L_x} (\psi\bar{\psi})^x_y(i) \prod_{j=1}^{L_y} (\psi\bar{\psi})^y_x(j). \tag{2.25}$$

Different choices of T^z at different xy planes give the same Ψ^z when acting on the ground space. Similarly, we can define Ψ^x and Ψ^y.

If we take the net shape of Fig. 2.8 (a) but replace all $\psi\bar{\psi}$'s with $\sigma\bar{\sigma}$'s, then we obtain an operator which we call a Σ-net, or Σ^z in this case, to be more precise. Each Σ^α splits into two operators $\Sigma^\alpha = e^\alpha + m^\alpha$ of the same net shape. In the case of Σ^z, the operators e^z and m^z are distinguished by the parity p^z of the fermion mode

$$\prod_{i=1}^{L_x} (\sigma\bar{\sigma})^x(i) \prod_{j=1}^{L_y} (\sigma\bar{\sigma})^y(j),$$

which is a good quantum number. This is because anyons such as $\sigma^x(i)$ which can change p^z by braiding with Σ^z are confined.

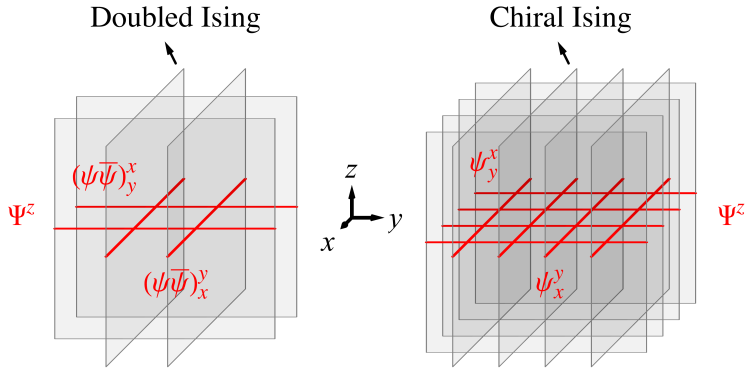

Figure 2.8: Net-shaped logical operator Ψ^z defined in (2.25), which is to be condensed in Ising cage-net. In (a), each plane is a layer of doubled Ising, and the red strings are $(\psi\bar{\psi})^x_y(i)$ and $(\psi\bar{\psi})^y_x(j)$. In (b), equivalently, each plane is a layer of chiral Ising, and the red strings are $\psi^x_y(i)$ and $\psi^y_x(j)$.

The semisimple algebra of the decoupled layers is

$$A = (\mathrm{Mat}_3 \oplus \mathrm{Mat}_1)^{\otimes 2(L_x+L_y+L_z)}.$$

Besides the condensation condition, we need to quotient A by relations due to deconfined excitations. Since Ising cage-net has deconfined fractons, lineons and planons, it is not obvious where exactly the relations come from. Therefore, we

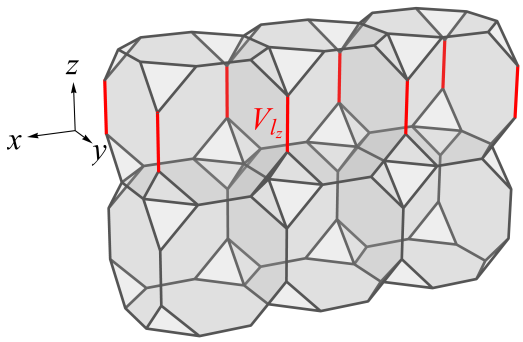

Figure 2.9: Action on the lattice degrees of freedom of the operator Ψ^z, which is to be condensed in Ising cage-net. The product of V_{l_z} on the red edges (the set T^z in (2.25)) is the net-shaped logical operator Ψ^z shown in Fig. 2.8 (a). Note that (2.25) shown here is a logical operator, whereas (2.18) shown in Fig. 2.6 creates excitations.

return to the Hamiltonian (2.3) and construct the relations from the Hamiltonian terms.

Firstly, the Hamiltonian (2.3) contains the doubled Ising plaquette terms $B_p^0 = 1$ and B_p^2, so a ground state must satisfy the projector

$$\frac{1}{2}\left(1 + B_p^2\right) = \frac{1}{2}\left(B_p^1\right)^2 \tag{2.26}$$

In the string-net model of doubled Ising, a 1-loop on a (smallest) plaquette can be viewed as a σ-loop or, equivalently, a $\bar{\sigma}$-loop. Here, we interpret (2.26) as creating a loop of $\sigma\bar{\sigma}$ at a plaquette. Suppose that this plaquette term is placed "around the corner edges" like

$$\frac{1}{2}\left(B_p^1\right)^2 = \quad .$$

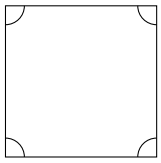

This simplifies to the relation

$$r^\alpha(i)\bar{r}^\alpha(i) = 1 \tag{2.27}$$

in each layer i orthogonal to the α direction, where e.g.

$$r^x(i) = \frac{1}{2}\left(1 + \psi_y^x(i) + \psi_z^x(i) - \psi_y^x(i)\psi_z^x(i)\right),$$

and similarly for $\bar{r}^\alpha(i)$.

Secondly, we can also place a cage term B_c "around the corner edges" (Fig. 2.10). This term involves 1-loops in the xy, yz and zx planes. In the setup of Fig. 2.10, we can bring the 1-loops closer together by enlarging the cube c to size $L_x \times L_y \times 1$. The result is a flat, degenerate cuboid, some of whose edges coincide with each other. This enlargement is allowed since the 1-loops can be deformed individually in each layer of doubled Ising and the enlarged cage term commutes with the condensation terms V_{l_μ}. We can then simplify this large cage term. The red strings give

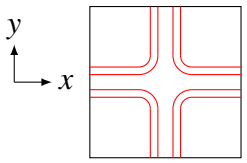

$$= 2r^z(i)r^z(i+1),$$

where the two 1-loops are in different xy planes but drawn in the same plane for illustration, and we draw the degenerate cuboid as a large yet non-degenerate one. We chose to interpret the two 1-loops as two σ-loops; other interpretations such as one σ-loop and one $\bar{\sigma}$-loop are all equivalent due to (2.27). The green strings give

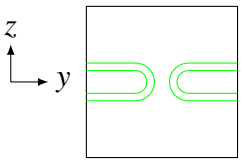

$$= 2,$$

Note that this simplification uses only the fusion rules, F-symbols and R-symbols. Similarly, the blue strings simplify to a constant 2. Therefore, Fig. 2.10 gives a relation $r^z(i)r^z(i+1) = 1$.

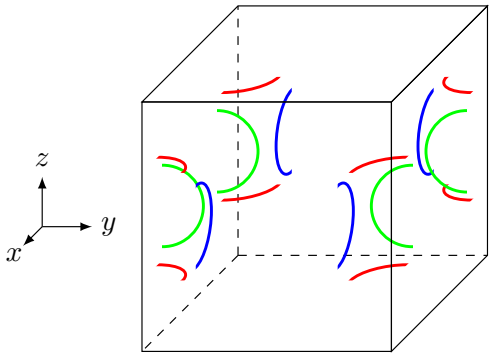

Figure 2.10: Cage term B_c of Ising cage-net placed 'around the corner edges'. The red, green and blue strings are 1-loops in the xy, yz and zx planes, respectively.

In summary, the Hamiltonian (2.3) implies that the product of $r^\alpha(i)$ or $\bar{r}^\alpha(i)$ with any other $r^\alpha(j)$ or $\bar{r}^\alpha(j)$ should be 1, where i and j may or may not be equal. We observe that for the purpose of writing down relations, there is no difference

between anyons with and without bars. Therefore, from now on we will consider the system as $2L_x$, $2L_y$ and $2L_z$ layers of chiral Ising. The names of operators change accordingly, e.g.

$$\Psi^z = \prod_{i=1}^{2L_x} \psi_y^x(i) \prod_{j=1}^{2L_y} \psi_x^y(j),$$

as shown in Figure 2.8 (b). Let M be the subalgebra of A generated by Ψ^x, Ψ^y and Ψ^z, and M' the commutant of M. Inside M', the relations amount to central projectors

$$P_{\mathrm{c}} = \frac{1}{8}(1+\Psi^x)(1+\Psi^y)(1+\Psi^z) \tag{2.28}$$

due to condensation, and

$$P_{ij}^{\alpha} = \frac{1}{2}\left(1 + r^{\alpha}(i) r^{\alpha}(j)\right) \tag{2.29}$$

due to deconfined planons and cage terms. Their product is

$$P = P_c \prod_{\alpha} \prod_{i<j} P_{ij}^{\alpha}. \tag{2.30}$$

With the above setup, we are ready to calculate the GSD.

GSD from Cartan subalgebra

Following Section 2.6, we calculate the GSD of Ising cage-net using a Cartan subalgebra. The semisimple algebra A has a Cartan subalgebra C spanned by the elementary operators with no σ. Just like in Section 2.6, it happens that $C \subset M'$, and the central projectors P_{c} and P_{ij}^{α} all map C to C. We also have the splitting of the Σ-nets, but this does not enlarge the Cartan subalgebra. This is because every Σ^{α} (and hence e^{α} and m^{α}) braids non-trivially with some ψ operator. Therefore, we have GSD $= \mathrm{tr}(P)$, where the underlying vector space is C. Again using the argument in Section 2.6, if P is expanded into a linear combination of elementary operators, then only the constant term $\mu_0 = \mu(1,1,1,1,1,1)$ (which is called $\mu(1,1)$ for 1-F Ising) contributes to $\mathrm{tr}(P)$.

To compute μ_0, we need to expand (2.30). This is very similar to the calculation in Section 2.6. Firstly, we have

$$\prod_{i<j} P_{ij}^{\alpha} = \frac{1}{2^{2L_\alpha}} \left[\prod_{i=1}^{2L_\alpha} (1 + r^{\alpha}(i)) + \prod_{i=1}^{2L_\alpha} (1 - r^{\alpha}(i)) \right].$$

Thus

$$\begin{aligned}P = \frac{1}{8}(1 &+ \Psi^x + \Psi^y + \Psi^z \\ &+ \Psi^y\Psi^z + \Psi^z\Psi^x + \Psi^x\Psi^y + \Psi^x\Psi^y\Psi^z) \\ &\times \prod_\alpha \frac{1}{2^{2L_\alpha}} \left[\prod_{i=1}^{2L_\alpha}(1 + r^\alpha(i)) + \prod_{i=1}^{2L_\alpha}(1 - r^\alpha(i))\right].\end{aligned}$$

We need to find terms in the expansion of $\prod_\alpha(\cdots)$ that combines with one of the eight terms $1, \Psi^x, \ldots, \Psi^x\Psi^y\Psi^z$ to give a constant term. Now, for example, the only four terms in the expansion of $\prod_i(1 + r^z(i))$ that can possibly contribute to μ_0 are

$$\left(\frac{3}{2}\right)^{2L_z}, \prod_i\left(\frac{1}{2}\psi_x^z(i)\right), \prod_i\left(\frac{1}{2}\psi_y^z(i)\right), \prod_i\left(-\frac{1}{2}\psi_x^z(i)\psi_y^z(i)\right).$$

Therefore, we can write

$$\begin{aligned}P = \frac{1}{8}&(1 + \Psi^x + \Psi^y + \Psi^z + \Psi^y\Psi^z + \Psi^z\Psi^x + \Psi^x\Psi^y + \Psi^x\Psi^y\Psi^z) \\ &\times \frac{1}{2^{4L_x}}\left[\left(9^{L_x} + 1\right) + 2\prod_i \psi_y^x(i) + 2\prod_i \psi_z^x(i) + 2\prod_i \psi_y^x(i)\psi_z^x(i)\right] \\ &\times \frac{1}{2^{4L_y}}\left[\left(9^{L_y} + 1\right) + 2\prod_j \psi_z^y(j) + 2\prod_j \psi_x^y(j) + 2\prod_j \psi_z^y(j)\psi_x^y(j)\right] \\ &\times \frac{1}{2^{4L_z}}\left[\left(9^{L_z} + 1\right) + 2\prod_k \psi_x^z(k) + 2\prod_k \psi_y^z(k) + 2\prod_k \psi_x^z(k)\psi_y^z(k)\right] + \cdots,\end{aligned}$$

where "$\cdots$" means terms that cannot possibly contribute to μ_0. Up to permutation of x, y and z, the pairing of the terms works as follows:

$$\begin{aligned}1 &\iff \left(9^{L_x} + 1\right) \times \left(9^{L_y} + 1\right) \times \left(9^{L_z} + 1\right), \\ \Psi^z &\iff \left(9^{L_z} + 1\right) \times 2\prod_i \psi_y^x(i) \times 2\prod_j \psi_x^y(j), \\ \Psi^x\Psi^y &\iff 2\prod_i \psi_z^x(i) \times 2\prod_j \psi_z^y(j) \\ &\qquad \times 2\prod_k \psi_x^z(k)\psi_y^z(k), \\ \Psi^x\Psi^y\Psi^z &\iff 2\prod_i \psi_y^x(i)\psi_z^x(i) \times 2\prod_j \psi_z^y(j)\psi_x^y(j) \\ &\qquad \times 2\prod_k \psi_x^z(k)\psi_y^z(k),\end{aligned}$$

where " $\Longleftrightarrow$ " indicates the pairing. Combining these together, we obtain

$$\begin{aligned}\mathrm{GSD} &= 2^{4(L_x+L_y+L_z)}\mu_0 \\ &= \frac{1}{8}\Big[\left(9^{L_x}+1\right)\left(9^{L_y}+1\right)\left(9^{L_z}+1\right) \\ &\qquad + 4\left(9^{L_x}+1\right) + 4\left(9^{L_y}+1\right) + 4\left(9^{L_z}+1\right) \\ &\qquad + 8 + 8 + 8 + 8\Big] \\ &= \frac{1}{8}(E_3 + E_2 + 5E_1 + 45),\end{aligned}$$

where $E_3 = 9^{L_x+L_y+L_z}$, $E_2 = 9^{L_x+L_y} + 9^{L_y+L_z} + 9^{L_z+L_x}$, and $E_1 = 9^{L_x} + 9^{L_y} + 9^{L_z}$. In Appendix 2.11, we confirm this result for the smallest system size $L_x = L_y = L_z = 1$ with a lattice calculation independent of the operator algebra approach.

GSD from full algebra

To conclude our discussion of Ising cage-net, we calculate its GSD using the full semisimple algebra, as we did in Sections 2.5 and 2.6.

Similar to 1-F Ising, the central projectors P^α_{ij} defined in (2.29) kill most of the components of the semisimple algebra M'. This is because for each α, projection by P^α_{ij} forces the $r^\alpha(i)$'s to be all $+1$ or all -1. We have

$$\prod_\alpha \prod_{i<j} P^\alpha_{ij} A = (B^x_0 \oplus B^x_1) \otimes (B^y_0 \oplus B^y_1) \otimes (B^z_0 \oplus B^z_1),$$

where $B^\alpha_0 \cong \mathrm{Mat}_{9^{L_\alpha}}$ and $B^\alpha_1 \cong \mathrm{Mat}_1$. We can define central projectors

$$Q_{s_x s_y s_z} = \prod_\alpha \left[\frac{1}{2^{2L_\alpha}} \prod_{i=1}^{2L_\alpha} (1 + (-1)^{s_\alpha} r^\alpha(i))\right],$$

where $s_\alpha = 0$ or 1, which project onto the components

$$B_{s_x s_y s_z} = \bigotimes_\alpha B^\alpha_{s_\alpha}.$$

We need to find the action of P_{c} defined in (2.28) on

$$\left[\bigotimes_\alpha (B^\alpha_0 \oplus B^\alpha_1)\right] \cap M'.$$

This intersection has eight components, which are $B_{000} \cap M'$ and so on. Up to permutation of x, y and z, we have four cases, and we discuss them in ascending order of difficulty:

(1) On $B_{111} \cap M' = B_{111}$, every $\psi^\alpha_\beta(i)$ acts as -1, so $P_c Q_{111} M' = B_{111} = \mathrm{Mat}_1$.

(2) On $B_{110} \cap M'$, each of $\psi^x_y(i)$, $\psi^x_z(i)$, $\psi^y_z(j)$ and $\psi^y_x(j)$ acts as -1, while each of $\psi^z_x(k)$ and $\psi^z_y(k)$ has the representation ρ_3 given by (2.14). By Lemma 4, the central projector $P_c Q_{110}$ is primitive. To determine the matrix algebra $P_c Q_{110} M'$, we need the representation ρ_l of $\mathrm{Mat}_1 \otimes \mathrm{Mat}_1 \otimes \mathrm{Mat}_{9^{L_z}}$ where $l = 9^{L_z}$. More precisely, we need the common eigenspace $\{w\}$ such that $\rho_l(\Psi^\alpha)w = +w$ for all α. Now we already have $\rho_l(\Psi^z)w = +w$ because $\psi^x_y(i) = -1$ and $\psi^y_x(j) = -1$. To ensure e.g. $\rho_l(\Psi^x)w = +w$, we must have

$$\left[\bigotimes_k \rho_3[\psi^z_y(k)]\right] w = +w, \tag{2.31}$$

since $\psi^y_z(j) = -1$. Similarly, we must also have

$$\left[\bigotimes_k \rho_3[\psi^z_x(k)]\right] w = +w. \tag{2.32}$$

The dimension of the eigenspace that satisfies (2.31) and (2.32) is precisely $D^{++}_{2L_z}$ defined in (2.24). Therefore, we have $P_c Q_{110} M' = \mathrm{Mat}_{(9^{L_z}+3)/4}$.

(3) On $B_{001} \cap M'$, each of $\psi^z_x(k)$ and $\psi^z_y(k)$ acts as -1, while each of $\psi^x_y(i)$, $\psi^x_z(i)$, $\psi^y_z(j)$ and $\psi^y_x(j)$ has the representation ρ_3. To determine the matrix algebra $P_c Q_{001} M'$, we need the common eigenspace $\{w\}$ such that $\rho_l(\Psi^\alpha)w = +w$ in the representation ρ_l of $\mathrm{Mat}_{9^{L_x}} \otimes \mathrm{Mat}_{9^{L_y}} \otimes \mathrm{Mat}_1$ where $l = 9^{L_x+L_y}$. From $\rho_l(\Psi^x)w = \rho_l(\Psi^y)w = +w$ and $\psi^z_x(k) = \psi^z_y(k) = -1$ we obtain

$$\left[\bigotimes_i \rho_3[\psi^x_z(i)]\right] w = \left[\bigotimes_j \rho_3[\psi^y_z(j)]\right] w = +w.$$

Meanwhile, $\rho_l(\Psi^z)w = +w$ implies two possibilities

$$\left[\bigotimes_i \rho_3[\psi^x_y(i)]\right] w = \left[\bigotimes_j \rho_3[\psi^y_x(i)]\right] w = \pm w. \tag{2.33}$$

If we take the $+w$ in (2.33), then we obtain a subspace of dimension $D^{++}_{2L_x} D^{++}_{2L_y}$. On the other hand, if we take the $-w$ in (2.33), then we obtain a subspace of dimension $D^{-+}_{2L_x} D^{+-}_{2L_y}$. Overall, we have $P_c Q_{001} M' = \mathrm{Mat}_{(9^{L_x+L_y}+9^{L_x}+9^{L_y}+5)/8}$.

(4) On $B_{000} \cap M'$, every $\psi^\alpha_\beta(i)$ has the representation ρ_3. To determine the matrix algebra $P_c Q_{000} M'$, we need the common eigenspace $\{w\}$ such that $\rho_l(\Psi^\alpha)w = +w$

in the representation of $\mathrm{Mat}_{9^{L_x}} \otimes \mathrm{Mat}_{9^{L_y}} \otimes \mathrm{Mat}_{9^{L_z}}$ where $l = 9^{L_x+L_y+L_z}$. This gives the equations

$$\left[\bigotimes_j \rho_3[\psi_z^y(j)]\right] w = \left[\bigotimes_k \rho_3[\psi_y^z(k)]\right] w = \pm w, \tag{2.34}$$

$$\left[\bigotimes_k \rho_3[\psi_x^z(k)]\right] w = \left[\bigotimes_i \rho_3[\psi_z^x(i)]\right] w = \pm w, \tag{2.35}$$

$$\left[\bigotimes_i \rho_3[\psi_y^x(i)]\right] w = \left[\bigotimes_j \rho_3[\psi_x^y(i)]\right] w = \pm w. \tag{2.36}$$

Depending on the choice of $\pm w$ in these equations, we have eight possibilities. For example, we can choose $-w$ in (2.34) and (2.35) and $+w$ in (2.36), which has a contribution of $D^{+-}_{2L_x} D^{-+}_{2L_y} D^{--}_{2L_z}$ to the dimension of the common eigenspace. The total dimension is

$$\begin{aligned} &D^{++}_{2L_x} D^{++}_{2L_y} D^{++}_{2L_z} + \left(D^{-+}_{2L_x} D^{+-}_{2L_y} D^{++}_{2L_z} + \text{perm.}\right) \\ &+ \left(D^{+-}_{2L_x} D^{-+}_{2L_y} D^{--}_{2L_z} + \text{perm.}\right) + D^{--}_{2L_x} D^{--}_{2L_y} D^{--}_{2L_z} \\ &= \frac{1}{8}(E_3 + E_1 + 4), \end{aligned}$$

where "perm." means permutations of x, y and z. Since $D^{+-}_{2L} = D^{-+}_{2L}$, only cyclic permutations are included. Therefore, we have $P_{\mathrm{c}} Q_{000} M' = \mathrm{Mat}_{(E_3+E_1+4)/8}$.

Summarizing all four cases, we have

$$\begin{aligned} PM' = \mathrm{Mat}_{(E_3+E_1+4)/8} &\\ \oplus \left(\mathrm{Mat}_{(9^{L_x+L_y}+9^{L_x}+9^{L_y}+5)/8} \oplus \text{perm.}\right) &\\ \oplus \left(\mathrm{Mat}_{(9^{L_z}+3)/4} \oplus \text{perm.}\right) \oplus \mathrm{Mat}_1. & \end{aligned}$$

Using Protocol 5 with the conjecture of "filling the blanks", we obtain GSD $= (E_3 + E_2 + 5E_1 + 45)/8$. In Appendix 2.11, we confirm this result for the smallest system size $L_x = L_y = L_z = 1$ with a lattice calculation independent of the operator algebra approach.

2.8 Appendix A: additional math details

In this section, we list some definitions and theorems that are used in the main text. They can also be found in mathematics textbooks such as Ref. [75].

Definition 8. An *algebra* is a complex vector space A equipped with associative multiplication and a multiplicative identity 1, such that

$$\begin{aligned}(x+y)z &= xz + yz,\\ z(x+y) &= zx + zy,\\ (\lambda x)(\mu y) &= (\lambda\mu)(xy),\end{aligned}$$

for all $x, y, z \in A$, and $\lambda, \mu \in \mathbb{C}$. An *involution* is an antilinear map $x \mapsto x^*$ on A such that $1^* = 1$, $x^{**} = x$ and $(xy)^* = y^*x^*$ for all $x, y \in A$. The involution is *positive* if $x^*x \neq 0$ for all $x \neq 0$.

For a semisimple algebra A in 2D, the involution is defined on elementary operators by replacing anyons a, b, c with their respective antiparticles a^*, b^*, c^*, and extended to A antilinearly, i.e. $(\lambda x)^* = \lambda^* x^*$ where $\lambda \in \mathbb{C}$, $x \in A$ and λ^* is the complex conjugate of λ. In the examples in this paper, all anyons are self-dual, so the involution acts trivially on the elementary operators. We can check explicitly for chiral Ising that this map is indeed an involution and is positive. Note that this check is performed manually on elementary operators for the definition of involution, and on an arbitrary operator for positivity. We cannot trivialize this check by identifying the operators with block-diagonal matrices, which would require Theorem 12. Although the check is tedious, we do not know an easier method.

In an algebra, the structures that can be quotiented out are called ideals.

Definition 9. A subset $I \subset A$ is an *ideal* if I is a vector subspace of A and for all $r \in I$, $x \in A$, we have $rx \in I$, $xr \in I$. In the presence of an involution, an ideal $I \subset A$ is *involutive* if it is closed under the involution.

Basically, an involutive ideal is a set of elements that can be identified with 0 consistently, since if r is identified with 0 then so are r^*, rx and xr for all $x \in A$. If I is an involutive ideal, then the quotient algebra A/I is defined in the same way as for quotients of vector spaces. If A is finite dimensional, then A/I is also an algebra with positive involution (positivity is a consequence of Theorem 12). When we reduced A to A_0 in Section 2.3, we found relations among the elementary operators from physical argument, generated an ideal I from the relations, and then took the quotient A/I. Here, if $\Omega \subset A$ is a subset, e.g. $\Omega = \{\omega_1, \omega_2\}$, then the ideal generated by Ω is written as

$$\langle \omega_1, \omega_2 \rangle_{\mathrm{id},\, A} = \{x_1\omega_1 y_1 + x_2\omega_2 y_2 \,|\, x_i, y_i \in A\},$$

where the subscript A indicates the overall algebra. In other words, the ideal generated by Ω is the smallest ideal of A containing Ω, as we need to multiply ω_i on both the left and the right, and then take linear combinations to make it an ideal. In all of the physical examples in this paper, such ideals happen to be involutive. When it is clear from context, we will drop the word "involutive" and simply say "ideal".

The fact that matrix algebras do not have non-trivial ideals can be summarized as follows:

Definition 10. An algebra A_0 is *simple* if its only (not necessarily involutive) ideals are $\{0\}$ and A_0 itself.

Lemma 11. A finite dimensional algebra is simple if and only if it is a matrix algebra.

Note that the notions of simplicity and semisimplicity (Definition 1) do not rely on an involution. The following theorem relates semisimple algebras to algebras with positive involution:

Theorem 12. Let A be a finite dimensional algebra with positive involution. Then A is semisimple, and can be written in the form of (2.5) where the involution acts as Hermitian conjugation of matrices.

This is why positivity of the involution is important, and the theorem fails if the involution is not positive (see example in Appendix 2.8). The ideals of a semisimple algebra (2.5) are of the form $A_{i_1} \oplus \cdots \oplus A_{i_k}$ where $1 \le i_1 < \cdots < i_k \le m$. In other words, to write down an ideal I of A, we simply throw away some of the summands in (2.5) and keep the rest. Therefore, to make the quotient A/I simple, we need to throw away precisely one A_i and put the rest into the ideal I, and A/I is isomorphic to this A_i.

To generate an ideal from relations, we need to use the primitive central projectors $\{P_i\}$. Suppose we want an ideal $I = \langle\{x_k\}\rangle_{\mathrm{id},\,A}$ where $\{x_k\}$ are some general elements. Let

$$S = \{i \mid P_i x_k \neq 0 \text{ for some } k\}.$$

Then we have

$$I = \bigoplus_{i\in S} A_i, \quad A/I = \bigoplus_{i\notin S} A_i = \left(\sum_{i\notin S} P_i\right) A.$$

The proof is straightforward, and the idea is that if x_k has a non-trivial component in some A_i, then the entirety of A_i must be in I. We can view this statement as a more general version of (2.11).

Finally, we have a more rigorous version of Lemma 4:

Lemma 13. Let B be a finite dimensional simple algebra with positive involution, N an abelian, involutive subalgebra of B, and N' the commutant of N. Then we have $Z(N') = N$.

This can be derived from the so-called von Neumann Bicommutant Theorem:

Theorem 14. Let B, N and N' be as in Lemma 4, and N'' the commutant of N'. Then we have $N'' = N$.

Using this theorem, we have $N'' = N \subset Z(N') \subset N''$, so $N = Z(N')$.

When discussing Definition 6, we mentioned that a Cartan subalgebra must satisfy an extra condition. Here is a rigorous definition of a Cartan subalgebra:

Definition 15. A subalgebra C of an algebra A is a *Cartan subalgebra* if it is abelian, diagonalizable and maximal. Diagonalizable means that every $x \in C$ is diagonalizable in its (faithful) block-diagonal matrix representation; maximal means that if any subalgebra $C' \subset A$ is abelian and diagonalizable and $C \subset C'$, then $C' = C$.

Diagonalizability can also be characterized intrinsically: An element $x \in A$ is diagonalizable if and only if its minimal polynomial has distinct linear factors [76]. This statement can be used to show that the Cartan subalgebras we chose for 1-F Ising and Ising cage-net are indeed diagonalizable, since their operators all satisfy the polynomial $t^2 - 1 = (t+1)(t-1)$, which has distinct linear factors $(t+1)$ and $(t-1)$. Diagonalizability is needed for Lemma 7 to hold since e.g. the subalgebra of Mat_4 consisting of elements of the form

$$\begin{pmatrix} a & 0 & b & c \\ & a & d & e \\ & & a & 0 \\ & & & a \end{pmatrix}$$

is abelian, contains non-diagonalizable elements, and has dimension 5.

Examples of non-semisimple algebras

In this section, we give three examples of non-semisimple algebras and thus highlight the premises of Theorem 12.

(1) Let $A \subset \mathrm{Mat}_2$ be the algebra of 2×2 upper triangular matrices. Since $\dim(A) = 3$, if A is semisimple then it must be $3\mathrm{Mat}_1$. However, this implies that A is abelian, which is false. Therefore, A is not semisimple. Intuitively, this can be understood as due to the lack of an involution, since A is not closed under Hermitian conjugation.

(2) Let A be the involutive algebra generated by two formal elements 1 and a, where 1 is the multiplicative identity, $a^2 = 0$ and $a^* = a$. This involution is not positive, so Theorem 12 does not apply here. Indeed, since $\dim(A) = 2$, if A is semisimple then it must be $2\mathrm{Mat}_1$. However, we have an element $a \neq 0$, $a^2 = 0$, but there is no such element in $2\mathrm{Mat}_1$. Therefore, A is not semisimple.

(3) Let V be a complex vector space, possibly infinite dimensional. The *tensor algebra* over V is

$$T(V) = \bigoplus_{k=0}^{\infty} V^{\otimes k},$$

where $V^{\otimes 0} = \mathbb{C}$. The multiplication is formal, i.e. if $x \in V^{\otimes m}$ and $y \in V^{\otimes n}$ then $xy \in V^{\otimes(m+n)}$. The tensor algebra is always infinite dimensional regardless of $\dim(V)$, so Theorem 12 also does not apply here. Indeed, A is semisimple if and only if $V = \{0\}$ (we allow infinite direct sum in Definition 1). Suppose, for example, that V is spanned by a single element a. Then the quotient

$$T(V)/\langle a^2 \rangle_{\mathrm{id}, T(V)}$$

is precisely the A in the previous example, which is not semisimple. However, we know that a quotient of a semisimple algebra is also semisimple. Therefore, $T(V)$ is not semisimple. Since semisimplicity does not rely on an involution, here we do not need to assign an involution to $T(V)$ even though we could.

Incidentally, the finite dimensional semisimple algebra A in the operator algebra approach discussed in this paper can also be viewed as a quotient $T(V)/K$ of the tensor algebra. Here, V is the formal vector space over the elementary operators, and K is the ideal generated by multiplication rules which themselves are due to fusion rules, F-symbols and R-symbols.

Matrix representation of simple algebra

In this section, we answer the following question: Given an abstract finite dimensional simple algebra A_0 with positive involution, how do we find a matrix representation for it? Of course we have an isomorphism $\rho_n : A_0 \to \mathrm{Mat}_n$ for some n, such that the involution on A_0 maps to Hermitian conjugation on Mat_n. However, we want to determine ρ_n while only assuming knowledge of the structure constants $f_{\alpha\beta}^{\gamma}$ with respect to some basis $\{v_\alpha\}$, as defined in (2.9), as well as the action of the involution. This will lead to the representation (2.14) of chiral Ising operators without prior knowledge.

In our construction of ρ_n, we will make several claims without proof, and the proofs can be found in Ref. [75]. To start with, we solve the following set of linear and quadratic equations in the variables $\varepsilon_\alpha, \lambda_\alpha \in \mathbb{C}$:

$$\begin{aligned} \varepsilon^* &= \varepsilon, \\ \varepsilon^2 &= 1, \\ \varepsilon v_\alpha \varepsilon &= \lambda_\alpha \varepsilon \text{ for all } \alpha, \end{aligned} \tag{2.37}$$

where $\varepsilon = \sum_\alpha \varepsilon_\alpha v_\alpha$. We claim that (2.37) always has solutions. In fact, if $n > 1$ then there are many solutions, in which case we choose one solution. We can think of ε as the elementary matrices whose only non-zero entry is the $(1,1)$ entry, which is 1. The variables λ_α will be of no use for us.

Let V be the vector space spanned by $\{v_\alpha \varepsilon\}$. We claim that $\dim(V) = n$ even though we defined it as the span of n^2 elements. Clearly V is closed under left multiplication by A_0, and indeed it is the vector space that affords the representation ρ_n of A_0. Practically, we may reduce the overcomplete set $\{v_\alpha \varepsilon\}$ to obtain a basis for V. We want an inner product $\langle x, y\rangle$ for all $x, y \in V$, which then defines Hermitian conjugation of matrices. By the definition of V, there exist $a, b \in A_0$ (not unique) such that $x = a\varepsilon$, $y = b\varepsilon$. By (2.37), we have

$$x^* y = \varepsilon a^* b \varepsilon = \lambda \varepsilon$$

for some $\lambda \in \mathbb{C}$. Since $\varepsilon \neq 0$, this λ does not depend on the choice of a, b. We define $\langle x, y\rangle = \lambda$, and we claim that this is an inner product.

The Hermitian conjugation derived from this inner product is compatible with the involution on A_0. This is because for all $z \in A_0$ and $x, y \in V$, we have

$$\langle x, z^* y\rangle \varepsilon = x^* z^* y \varepsilon = (zx)^* y \varepsilon = \langle zx, y\rangle \varepsilon = \left\langle x, z^\dagger y\right\rangle \varepsilon,$$

which implies $z^* = z^\dagger$. Therefore, the action of A_0 on V by left multiplication serves as a representation ρ_n.

2.9 Appendix B: string-net models

In Appendix, we review the basics of the string-net models that are relevant for our purposes, and discuss the string-net models on the minimal lattice on the torus.. We follow the original construction as introduced in Ref. [68]. For more comprehensive introductions, we refer the readers to Ref. [68, 77–79].

String-net models

The input data of a string-net model is a unitary fusion category [80], which includes an index set $\{0, 1, ..., N\}$ and the associated data set $(\delta_{ijk}, d_s, F^{ijm}_{k\ell n})$. A string-net model is defined on a trivalent lattice, where the local DOF live on the edges. Each edge has a Hilbert space of $\text{span}_{\mathbb{C}}\{|0\rangle, |1\rangle ..., |N\rangle\}$. Usually, an edge of the string-net is represented by a directed line. For a directed edge, i^* represents the edge in the state i pointing in the opposite direction. That is

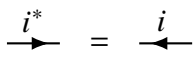

(2.38)

In particular, $0^* = 0$.

The δ-symbol specifies the vertex rules. δ_{ijk} takes values in $\{0, 1\}$ and it is symmetric under permutation of the indices. δ_{ijk} determines the allowed states on edges at a trivalent vertex. A vertex is stable[78] if

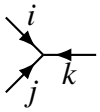

(2.39)

satisfies $\delta_{ijk} = 1$. A vertex is not stable if $\delta_{ijk} = 0$.

The d- and F-symbols define the graphical rules. The d-symbols evaluate loops to real numbers as

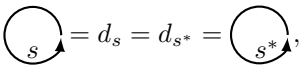

(2.40)

where $d_0 = 1$. They satisfy the equation

$$d_i d_j = \sum_k \delta_{ijk^*} d_k. \tag{2.41}$$

The F-symbols define the transformations

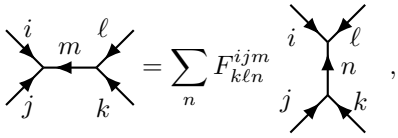

(2.42)

where the F-symbols are nonzero if all the vertices satisfy the vertex rules. They are normalized as

$$F^{ijk}_{j^*i^*0} = \sqrt{\frac{d_k}{d_i d_j}}\delta_{ijk}\,. \tag{2.43}$$

For the cases of interest in this paper, the F-symbols satisfy the tetrahedral symmetry

$$F^{ijm}_{k\ell n} = F^{\ell km^*}_{jin} = F^{jim}_{\ell kn^*} = F^{imj}_{k^*n\ell}\sqrt{\frac{d_m d_n}{d_j d_\ell}}, \tag{2.44}$$

as well as *the pentagon equation*

$$\sum_n F^{ijm}_{k\ell n} F^{ps\ell^*}_{inq} F^{pqn}_{jkr^*} = F^{ps\ell^*}_{m^*kr^*} F^{rsm^*}_{ijq}\,. \tag{2.45}$$

From the pentagon equation, we can derive the orthogonality relation of the F-symbols that

$$\sum_n F^{ijm'}_{k\ell n}\left(F^{ijm}_{k\ell n}\right)^* = \delta_{mm'}, \tag{2.46}$$

where the complex conjugation on the F-symbol is given by

$$\left(F^{ijm}_{k\ell n}\right)^* = F^{i^*j^*m^*}_{k^*\ell^*n^*}. \tag{2.47}$$

The ground state wave-function of the string-net model $|\Psi\rangle$ is given by

$$|\Psi\rangle = \sum_{|X\rangle\in\mathcal{H}^{\mathrm{SN}}_{Q_v}} \Psi(X)\,|X\rangle\,, \tag{2.48}$$

where $\Psi(X) = \langle X|\Psi\rangle$, and $|X\rangle$ denotes a string-net configuration in the stable vertex subspace $\mathcal{H}^{\mathrm{SN}}_{Q_v}$. A vector $|X\rangle$ is a product state. Note that the set of all different $|X\rangle$'s form an orthonormal basis for this subspace. The graphical rules define a set of relations between the amplitudes

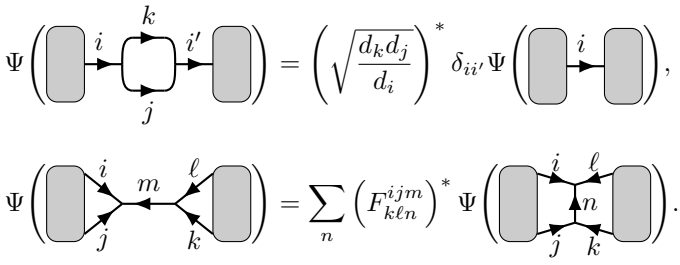

(2.49)

Moreover, the graphical rules can be used to define transformations for a generic string-net configuration ket-vector. Eq. (2.51) and Eq. (3.6) are examples.

The commuting projector Hamiltonian, which has the above wave-function as the ground state, is given by

$$H_{\mathrm{SN}} = -\sum_v Q_v - \sum_p B_p, \tag{2.50}$$

where Q_v is the vertex projector enforcing the vertex rules δ_{ijk}, and $B_p = \sum_s (d_s/D) B_p^s$ with $D = \sum_s (d_s)^2$ being the total quantum dimension is the plaquette projector. Each B_p^s adds a counter-clockwise directed loop of s in the interior of a plaquette. Its action can be evaluated by the F-symbols as for example,

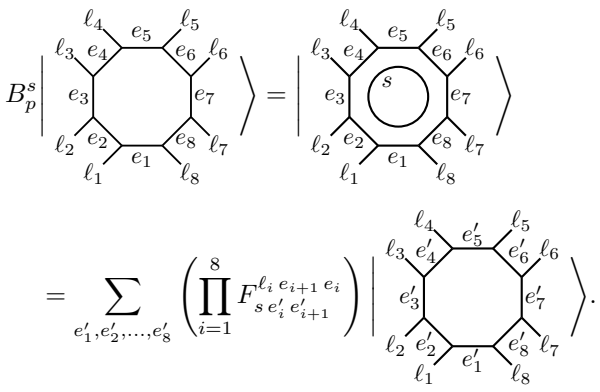

(2.51)

Eq. (2.41) implies that the B_p^s's satisfy

$$B_p^i B_p^j = \sum_k \delta_{ijk^*} B_p^k. \tag{2.52}$$

The ground state satisfies

$$Q_v |\Psi\rangle = |\Psi\rangle\,, \quad B_p |\Psi\rangle = |\Psi\rangle \tag{2.53}$$

for all v and p.

The minimal lattice

A string-net model can be defined on the minimal trivalent lattice on the torus. The minimal lattice consists of three edges, two vertices, and one plaquette as shown in Fig. 2.11. The ground states first have to satisfy the vertex constraints Q_v. Recall that a vertex is called stable if the vertex constraint is satisfied. We denote a basis vector of the stable vertex subspace on the minimal lattice by

$$|ijk\rangle = \Big| \; j \;\; i \;\; k \;\; j \;\; i \; \Big\rangle \in \mathcal{H}^{\mathrm{SN}}_{Q_v}. \tag{2.54}$$

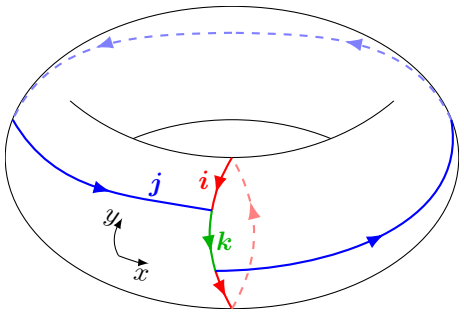

Figure 2.11: The minimal trivalent lattice on the torus. The lattice has three edges colored by red, blue, and green; two vertices; and one plaquette. i, j, and k are state labels on the colored edges.

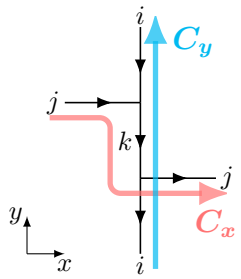

Figure 2.12: An illustration of the two non-contractible loops C_x and C_y on the minimal lattice, taken by the logical operators $W_\alpha^{C_i}$ where α is the excitation label.

The logical operators act within $\mathcal{H}_{Q_v}^{\mathrm{SN}}$. Illustrated in Fig. 2.12 are the two different paths taken by the logical operators $\{W_\alpha^{C_i}\}$ where $i \in \{x, y\}$ and $\alpha \in \{\text{excitations}\}$. The action of the logical operators on a basis vector $|ijk\rangle$ can be computed by the method introduced in Ref. [68], which we will not discuss in this paper. We will review a string-operator construction for the double-Ising in Appendix 2.10.

Next, the ground states need to satisfy the one plaquette term on the minimal lattice. Consider the action of B_p^s on a basis vector $|abc\rangle$. Instead of directly fusing the s-loop into the edges, we can first fuse different parts of the s-loop together and map it into a trivalent diagram

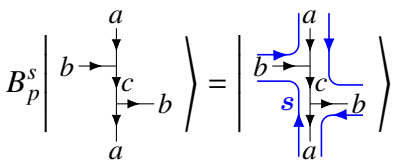

$$= \Big|$$ 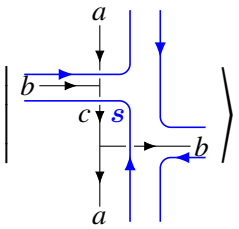

$$\Big\rangle$$

$$= \sum_{h,g} F^{s^*s0}_{s^*sh^*} F^{s^*s0}_{s^*sg} \Big|$$ 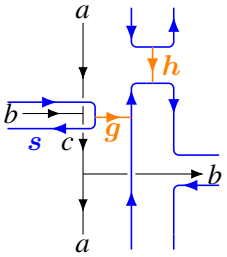

$$\Big\rangle$$

$$= \sum_{h,g} F^{s^*s0}_{s^*sh^*} F^{s^*s0}_{s^*sg} \Big|$$ 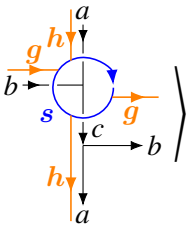

$$\Big\rangle$$

$$= \sum_{\substack{h,g,\\ t_1,t_2}} F^{s^*s0}_{s^*sh^*} F^{s^*s0}_{s^*sg} F^{s^*hs}_{gst_1} F^{sg^*s^*}_{h^*s^*t_2^*} \Big|$$ 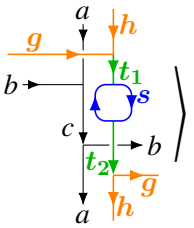

$$\Big\rangle$$

$$= \sum_{h,g,t_1} \frac{d_s}{(d_s)^2} \sqrt{\frac{d_h d_g}{d_{t_1}}} F^{s^*hs}_{gst_1} F^{sg^*s^*}_{h^*s^*t_1^*} \Big|$$ 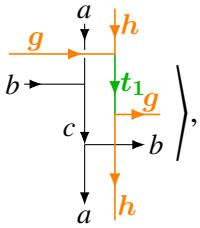

$$\Big\rangle, \tag{2.55}$$

where in the second equality, we have brought the s-loop over the lattice. We can also bring the loop below the lattice. The choice does not matter. The action of the B_p^s term can then be determined by fusing the trivalent diagram (orange) into the underlying lattice (black).

This will help us to show that for abelian string-net models, the plaquette term on the minimal lattice is trivial. For abelian string-net models, the fusion of s and s^* is

0. So, the above equation reduces to

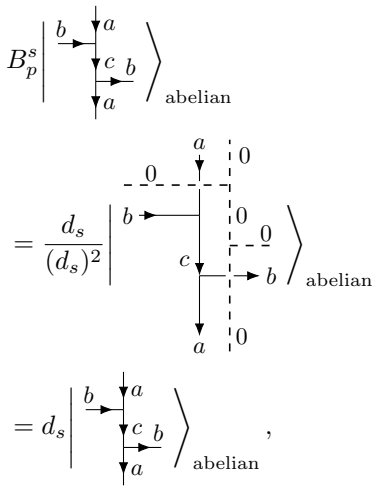

(2.56)

where to get to the last line, we have used $(d_s)^2 = 1$ for abelian models. Hence, we see that B_p acts as identity on $\mathcal{H}_{Q_v}^{\mathrm{SN}}$ in abelian models. In other words, on the minimal lattice, $\mathcal{H}_{Q_v}^{\mathrm{SN}}$ is the ground space of the abelian models.

2.10 Appendix C: the doubled-Ising string-net model

In this Appendix, we discuss the ground states of the doubled-Ising string-net on the minimal lattice. We show that when we put the doubled-Ising state on a lattice with smooth boundary, $\psi\bar{\psi}$ and $\sigma\bar{\sigma}$ are condensed on the boundary. The condensation is relevant to Chapter 3.

Doubled-Ising on minimal lattice

The doubled-Ising string-net on the minimal lattice has a 10-dimensional stable vertex subspace $\mathcal{H}_{Q_v}^{\mathrm{D.I.}}$, spanned by $|000\rangle$, $|220\rangle$, $|202\rangle$, $|022\rangle$, $|110\rangle$, $|112\rangle$, $|101\rangle$, $|011\rangle$, $|211\rangle$, and $|121\rangle$.

One of the dimensions is not part of the ground space, because the projector B_p has the eigenvalue of 0 on this state. To find the ground space, we calculate the action of B_p^1. Following from Eq. (2.55) (the actions of B_p^0 and B_p^2 are trivial), we find

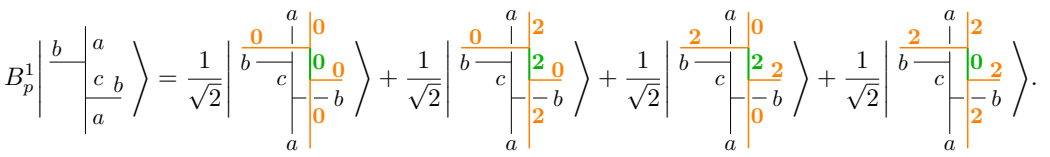

(2.57)

That is,

$$\begin{aligned} B_p^1 \left|abc\right\rangle &= \frac{1}{\sqrt{2}} \left(\mathbb{I} + W_\psi^{C_y} + W_\psi^{C_x} - W_\psi^{C_x} W_\psi^{C_y} \right) \left|abc\right\rangle \\ &= \frac{1}{\sqrt{2}} \left(\mathbb{I} + W_{\bar{\psi}}^{C_y} + W_{\bar{\psi}}^{C_x} - W_{\bar{\psi}}^{C_x} W_{\bar{\psi}}^{C_y} \right) \left|abc\right\rangle , \end{aligned} \tag{2.58}$$

where we have identified the logical operators by the construction discussed in Appendix 2.10, and the second equality follows from that we can bring the s-loop below the lattice in Eq. (2.55). We can further compute the action of B_p^1 by fusing the orange trivalent diagram into the underlying lattice. At this point, it is clear that a product state $\left|abc\right\rangle$ is generally not an eigenstate of B_p^1.

An explicit calculation shows that $\left|\psi\bar{\psi}_{\text{min}}^{\text{D.I.}}\right\rangle = -\frac{1}{2}\left|000\right\rangle + \frac{1}{2}\left|202\right\rangle + \frac{1}{2}\left|022\right\rangle + \frac{1}{2}\left|220\right\rangle$ has the eigenvalue $-\sqrt{2}$ under B_p^1. Hence, it is an excited state, which carries a $\psi\bar{\psi}$ fluxon. The other 9 dimensions have the eigenvalue $\sqrt{2}$ under B_p^1 and are, thus, ground states on the minimal lattice.

An orthonormal basis for the nine-dimensional ground space can be chosen to be the common eigenstates of logical operators $W_\psi^{C_x}$, $W_\psi^{C_y}$, $W_{\bar{\psi}}^{C_x}$, and $W_{\bar{\psi}}^{C_y}$, which all commute with each other. The nine common eigenstates are

$$\begin{aligned} \left|\Psi_{\text{min}}^{\text{D.I.}}\right\rangle_1 &= \frac{1}{2}\left|000\right\rangle + \frac{1}{2}\left|202\right\rangle + \frac{1}{2}\left|022\right\rangle - \frac{1}{2}\left|220\right\rangle , \\ \left|\Psi_{\text{min}}^{\text{D.I.}}\right\rangle_2 &= \frac{1}{\sqrt{2}}\left|011\right\rangle + \frac{i}{\sqrt{2}}\left|211\right\rangle , \\ \left|\Psi_{\text{min}}^{\text{D.I.}}\right\rangle_3 &= \frac{1}{\sqrt{2}}\left|101\right\rangle - \frac{i}{\sqrt{2}}\left|121\right\rangle , \\ \left|\Psi_{\text{min}}^{\text{D.I.}}\right\rangle_4 &= \frac{1}{\sqrt{2}}\left|011\right\rangle - \frac{i}{\sqrt{2}}\left|211\right\rangle , \\ \left|\Psi_{\text{min}}^{\text{D.I.}}\right\rangle_5 &= \frac{1}{2}\left|000\right\rangle - \frac{1}{2}\left|202\right\rangle + \frac{1}{2}\left|022\right\rangle + \frac{1}{2}\left|220\right\rangle , \\ \left|\Psi_{\text{min}}^{\text{D.I.}}\right\rangle_6 &= \frac{e^{-\frac{i\pi}{8}}}{\sqrt{2}}\left|110\right\rangle + \frac{ie^{-\frac{i\pi}{8}}}{\sqrt{2}}\left|112\right\rangle , \\ \left|\Psi_{\text{min}}^{\text{D.I.}}\right\rangle_7 &= \frac{1}{\sqrt{2}}\left|101\right\rangle + \frac{i}{\sqrt{2}}\left|121\right\rangle , \\ \left|\Psi_{\text{min}}^{\text{D.I.}}\right\rangle_8 &= \frac{e^{\frac{i\pi}{8}}}{\sqrt{2}}\left|110\right\rangle - \frac{ie^{\frac{i\pi}{8}}}{\sqrt{2}}\left|112\right\rangle , \\ \left|\Psi_{\text{min}}^{\text{D.I.}}\right\rangle_9 &= \frac{1}{2}\left|000\right\rangle + \frac{1}{2}\left|202\right\rangle - \frac{1}{2}\left|022\right\rangle + \frac{1}{2}\left|220\right\rangle . \end{aligned}$$

The 10th dimension $\left|\psi\bar{\psi}_{\text{min}}^{\text{D.I.}}\right\rangle$ is also a common eigenstate of $W_\psi^{C_x}$, $W_\psi^{C_y}$, $W_{\bar{\psi}}^{C_x}$, and

$W_{\bar{\psi}}^{C_y}$. In this basis, the logical operators takes the diagonal form

$$W_{\psi}^{C_x} = \left[\begin{pmatrix} 1 & 0 & 0 \\ 0 & 1 & 0 \\ 0 & 0 & -1 \end{pmatrix} \otimes \mathbb{I}_{3\times 3}\right] \oplus (-1), \tag{2.59}$$

$$W_{\psi}^{C_y} = \left[\begin{pmatrix} 1 & 0 & 0 \\ 0 & -1 & 0 \\ 0 & 0 & 1 \end{pmatrix} \otimes \mathbb{I}_{3\times 3}\right] \oplus (-1), \tag{2.60}$$

$$W_{\bar{\psi}}^{C_x} = \left[\mathbb{I}_{3\times 3} \otimes \begin{pmatrix} 1 & 0 & 0 \\ 0 & 1 & 0 \\ 0 & 0 & -1 \end{pmatrix}\right] \oplus (-1), \tag{2.61}$$

$$W_{\bar{\psi}}^{C_y} = \left[\mathbb{I}_{3\times 3} \otimes \begin{pmatrix} 1 & 0 & 0 \\ 0 & -1 & 0 \\ 0 & 0 & 1 \end{pmatrix}\right] \oplus (-1). \tag{2.62}$$

The aforementioned 10 states are obtained by directly diagonalizing the logical operators within the stable vertex space. Besides a computation using the F and the R symbols (see the next subsection for details), another way to compute the matrix elements of the logical operators is to use the Ω symbols or the half-braid tensors as in the original string-net paper [68]. We will not review them here. The reader should refer to Ref. [68, 78] for definition and details. However, for completeness, we present a solution to these Ω symbols for the doubled-Ising string-net:

Type	(n_0, n_1, n_2)	θ	Ω			
$\mathbb{1}\bar{\mathbb{1}}$	$(1,0,0)$	1	$\bar{\Omega}^0_{000} = 1$	$\bar{\Omega}^2_{002} = 1$	$\bar{\Omega}^1_{001} = 1$	
$\psi\bar{\psi}$	$(1,0,0)$	1	$\bar{\Omega}^0_{000} = 1$	$\bar{\Omega}^2_{002} = 1$	$\bar{\Omega}^1_{001} = -1$	
$\psi\bar{\mathbb{1}}$	$(0,0,1)$	-1	$\bar{\Omega}^0_{222} = -1$	$\bar{\Omega}^2_{220} = 1$	$\bar{\Omega}^1_{221} = i$	
$\mathbb{1}\bar{\psi}$	$(0,0,1)$	-1	$\bar{\Omega}^0_{222} = -1$	$\bar{\Omega}^2_{220} = 1$	$\bar{\Omega}^1_{221} = -i$	
$\sigma\bar{\psi}$	$(0,1,0)$	$-e^{i\pi/8}$	$\bar{\Omega}^0_{111} = \frac{1}{\sqrt{2}}(-e^{i\pi/8})$	$\bar{\Omega}^2_{111} = \frac{1}{\sqrt{2}}(ie^{i\pi/8})$	$\bar{\Omega}^1_{112} = i$	$\bar{\Omega}^1_{110} = 1$
$\sigma\bar{\mathbb{1}}$	$(0,1,0)$	$e^{i\pi/8}$	$\bar{\Omega}^0_{111} = \frac{1}{\sqrt{2}}(e^{i\pi/8})$	$\bar{\Omega}^2_{111} = \frac{1}{\sqrt{2}}(-ie^{i\pi/8})$	$\bar{\Omega}^1_{112} = i$	$\bar{\Omega}^1_{110} = 1$
$\psi\bar{\sigma}$	$(0,1,0)$	$-e^{-i\pi/8}$	$\bar{\Omega}^0_{111} = \frac{1}{\sqrt{2}}(-e^{-i\pi/8})$	$\bar{\Omega}^2_{111} = \frac{1}{\sqrt{2}}(-ie^{-i\pi/8})$	$\bar{\Omega}^1_{112} = -i$	$\bar{\Omega}^1_{110} = 1$
$\mathbb{1}\bar{\sigma}$	$(0,1,0)$	$e^{-i\pi/8}$	$\bar{\Omega}^0_{111} = \frac{1}{\sqrt{2}}(e^{-i\pi/8})$	$\bar{\Omega}^2_{111} = \frac{1}{\sqrt{2}}(ie^{-i\pi/8})$	$\bar{\Omega}^1_{112} = -i$	$\bar{\Omega}^1_{110} = 1$
$\sigma\bar{\sigma}$	$(1,0,1)$	1	$\bar{\Omega}^0_{000} = 1$	$\bar{\Omega}^2_{220} = 1 = \bar{\Omega}^0_{222}$	$\bar{\Omega}^1_{021} = 1 = \bar{\Omega}^1_{201}$	$\bar{\Omega}^2_{002} = -1$

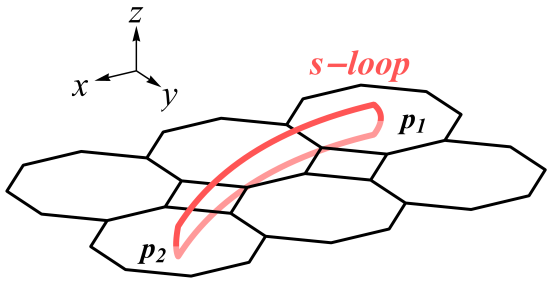

Figure 2.13: An illustration of an open ended fluxon string-operator $W^{\text{path}}_{\text{fluxon}}$ acting on a wave-function of the doubled-Ising string-net. $W^{\text{path}}_{\text{fluxon}}$ creates the fluxon and its antiparticle on the plaquettes p_1 and p_2. It does not create any excitations along the path. $W^{\text{path}}_{\text{fluxon}}$ is constructed by a loop of s-string that vertically penetrates the square-octagon lattice at the two plaquettes. The string-operators of $\psi\bar{\psi}$ and $\sigma\bar{\sigma}$ are given by a loop of 2-string and a loop of 1-string respectively.

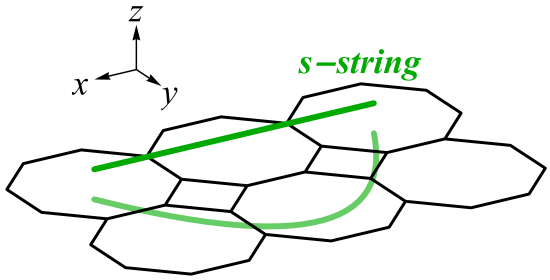

Figure 2.14: The open ended chargeon string-operators of the doubled-Ising string-net. They are constructed by line segements of the strings, which can be either above or below the lattice depending on the type of the chargeon excitations. On a ground state of the doubled-Ising, An open chargeon string-operator creates a vertex violation at each end. The ψ and σ string-operators correspond to a 2-string and a 1-string above the lattice respectively. The string-operators for $\bar{\psi}$ and $\bar{\sigma}$ correspond to those below the lattice.

Condensation on smooth boundary

Using the string-operator construction discussed in Ref. [77, 81], we can readily show that on the smooth boundary, the bosonic fluxons $\psi\bar{\psi}$ and $\sigma\bar{\sigma}$ condense.

Let us start with a review of the fluxon string-operators. Consider a large square-octagon lattice placed on the xy-plane as shown in Fig. 2.13. An open ended fluxon string-operator is given by a loop of s-string which vertically penetrates the lattice through the center of the plaquettes p_1 and p_2. The fluxon excitations are created at p_1 and p_2 respectively. The $\psi\bar{\psi}$ string-operator is given by a loop of 2-string, and that of $\sigma\bar{\sigma}$ is given by a loop of 1-string.

An open ended string-operator of a chargeon is constructed by a line segement,

which can be either above or below the lattice, as shown in Fig. 2.14.

To compute the action of the string-operators, we need the R-symbols and the S-matrix [49, 82]. The R-symbols define the braiding transformations

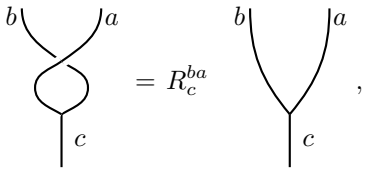

(2.63)

where $R_c^{ba} \in \mathbb{C}$. The inverse transformations are defined by

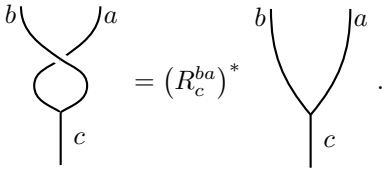

(2.64)

Same as the F-symbols, $R_c^{ba} \neq 0$ if $\delta_{bac} \neq 0$. Elements of the S-matrix are given by

$$S_{ab} = \frac{1}{\sqrt{D}} \sum_c d_c R_c^{ba} R_c^{ab}, \tag{2.65}$$

where $\sqrt{D} = \sqrt{\sum_s (d_s)^2} = 2$ is the total quantum dimension of the Ising unitary modular tensor category. The full S-matrix is

$$S = \frac{1}{2} \begin{pmatrix} 1 & \sqrt{2} & 1 \\ \sqrt{2} & 0 & -\sqrt{2} \\ 1 & -\sqrt{2} & 1 \end{pmatrix}. \tag{2.66}$$

Using the R- and F-symbols, we can always fuse the chargeon string-operators into the lattice at the cost of violating the vertex constraints at the ends. On the other hand, the fluxon string-operators can be fused into the lattice without introducing any vertex violations. For example, consider the action of a non-trivial fluxon

string-operator on the string-net wave-function

$$
\begin{aligned}
&\left|\ \right\rangle \\
&= \sum_j F^{ss0}_{eej} \left|\ \right\rangle \\
&= \sum_j F^{ss0}_{eej} \left(R^{es}_j\right)^* \left(R^{se}_j\right)^* \left|\ \right\rangle \\
&= \sum_j \frac{d_j}{d_e} \left(R^{es}_j\right)^* \left(R^{se}_j\right)^* \left|\ \right\rangle \\
&= \frac{\sqrt{D}}{d_e} S_{se} \left|\ \right\rangle .
\end{aligned}
\tag{2.67}
$$

Note that the expression above differs from that of Ref. [77] by a normalization factor, which is not important for our purposes. For an example of a chargeon string-operator, let us consider a line segment below the lattice. We compute

$$
\begin{aligned}
&\left|\ \right\rangle \\
&= \sum_j F^{ss0}_{eej} \left|\ \right\rangle \\
&= \sum_j F^{ss0}_{eej} \left(R^{es}_j\right)^* \left|\ \right\rangle \\
&= \sum_j F^{ss0}_{eej} \left(R^{es}_j\right)^* \left|\ \right\rangle ,
\end{aligned}
\tag{2.68}
$$

where in the last step we have removed the s-strings. So, we see that an open chargeon string-operator always creates violations to the vertex constraints.

Moreover, different fluxons correspond to different sets of eigenvalues of B_p^a. To determine these eigenvalues, we need the graphical rule

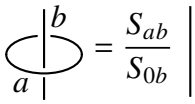

$$= \frac{S_{ab}}{S_{0b}} \, . \tag{2.69}$$

As an example, let us compute

$$\begin{aligned} & B_p^a W_{\psi\bar{\psi}}^{\text{path}} |\Psi_{\text{D.I.}}\rangle \\ & = B_p^a \Big| \Big\rangle_{\Psi_{\text{D.I.}}} = \Big| \Big\rangle_{\Psi_{\text{D.I.}}} \\ & = \frac{S_{a2}}{S_{02}} \Big| \Big\rangle_{\Psi_{\text{D.I.}}} , \end{aligned} \tag{2.70}$$

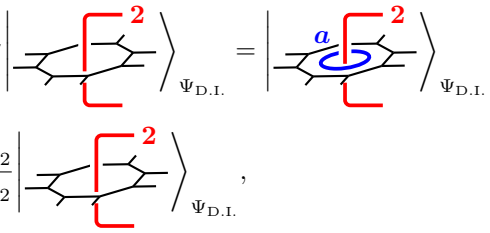

from which we see that the $\psi\bar{\psi}$ fluxon has the eigenvalues of 1, $-\sqrt{2}$, and 1 for B_p^0, B_p^1, and B_p^2 respectively. This result is exactly what we found for the $\psi\bar{\psi}$ fluxon state in Appendix 2.10. It is easy to see that the $\sigma\bar{\sigma}$ fluxon has $B_p^0 = 1$, $B_p^1 = 0$, and $B_p^2 = -1$.

We now show that, on the smooth boundary, the fluxons $\psi\bar{\psi}$ and $\sigma\bar{\sigma}$ are condensed. Without loss of generality, let us consider the doubled-Ising string-net with a single plaquette and everywhere else is set to $|0\rangle$. Consider the action of an open ended fluxon string-operator passing through the lattice just outside the plaquette

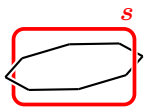

Since the s-loop does not pass through the region enclosed by the plaquette, the string-operator does not create any fluxon excitation on the plaquette. Via the F- and R-symbols, we can fuse the s-loop into the edges of the plaquette without changing any of the edges outside the plaquette or introducing any vertex violations. Therefore, we see that the fluxons all condense on the smooth boundary. On the other hand, because the chargeon string-operators necessarily introduce vertex violations, the chargeons remain as excitations on the boundary. Thus, we reach the conclusion that, on the smooth boundary, the condensed excitations are the fluxons $\psi\bar{\psi}$ and $\sigma\bar{\sigma}$.

2.11 Appendix D: GSD of the minimal Ising cage-net

In this appendix, we use the Hamiltonian (2.3) to calculate the GSD of Ising cage-net with system size $L_x = L_y = L_z = 1$ in terms of doubled Ising layers. This calculation does not involve the operator algebra approach and therefore serves as an independent check of (2.1) for the minimal system size. Indeed, we find GSD = 144 in agreement with (2.1).

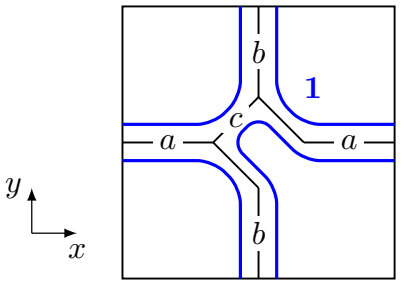

Figure 2.15: A minimal trivalent lattice, a state vector $|abc\rangle$, and the plaquette term B_p^1 (the blue 1-loop).

Recall from the last section that the string-net model of doubled Ising can be written on a minimal trivalent lattice (Fig. 2.15). State vectors are written as $|abc\rangle$, where $a, b, c = 0, 1$ or 2. The subspace of the Hilbert space that satisfies the vertex terms A_v has dimension 10. It is spanned by (note that the vectors below form a different basis of the ground space than those in Appendix 2.9)

$$\begin{aligned}
&w_1 = |101\rangle\,,\ w_2 = |011\rangle\,,\ w_3 = |110\rangle\,,\\
&w_4 = |121\rangle\,,\ w_5 = |211\rangle\,,\ w_6 = |112\rangle\,,\\
&w_7 = \frac{1}{2}|000\rangle + \frac{1}{2}|202\rangle + \frac{1}{2}|022\rangle - \frac{1}{2}|220\rangle\,,\\
&w_8 = \frac{1}{2}|000\rangle - \frac{1}{2}|202\rangle + \frac{1}{2}|022\rangle + \frac{1}{2}|220\rangle\,,\\
&w_9 = \frac{1}{2}|000\rangle + \frac{1}{2}|202\rangle - \frac{1}{2}|022\rangle + \frac{1}{2}|220\rangle\,,\\
&w_{10} = -\frac{1}{2}|000\rangle + \frac{1}{2}|202\rangle + \frac{1}{2}|022\rangle + \frac{1}{2}|220\rangle\,.
\end{aligned} \tag{2.71}$$

The only nontrivial plaquette term is B_p^1 (Fig. 2.15), which is a 1-loop that traverses each edge twice. It can also be viewed as a σ-loop (or equivalently, a $\bar{\sigma}$-loop) placed "around the corners". Using the method of (2.8), we find $B_p^1 = \sqrt{2}\,r$, whose eigenvalues are $\pm\sqrt{2}$. We then find

$$\begin{aligned}
&B_p^1 w_i = +\sqrt{2}\,w_i \quad \text{for} \quad i = 1, \ldots, 9,\\
&B_p^1 w_{10} = -\sqrt{2}\,w_{10}.
\end{aligned}$$

The details of this calculation are not important and we omit it here, as B_p^1 does not appear in the minimal Ising cage-net since it does not commute with the condensation operators V_{l_μ}. We conclude that the ground space of the minimal doubled Ising is spanned by $w_1, \ldots, w_9$.

The minimal Ising cage-net

The minimal Ising cage-net is obtained by condensing $\psi\bar{\psi}$ p-loops in three copies of minimal doubled Ising which are pairwise orthogonal. We label the states in e.g. the doubled Ising perpendicular to the z direction by $|a_x^z b_y^z c^z\rangle$, where a_x^z is on the edge in the x direction, etc. The Hamiltonian consists of condensation operators V_{l_μ}, vertex terms A_v and a single cube term B_c, but with an important caveat: B_c acts on a "degenerate" cube, whose opposite faces are identified. For example, its upper and lower faces are both proportional to

$$r^z = \frac{1}{2}(1 + \psi_x^z + \psi_y^z - \psi_x^z\psi_y^z).$$

Since $(r^z)^2 = 1$, the product of these two faces is a constant. Thus B_c is a constant and we can ignore it.

The subspace of the Hilbert space that satisfies the vertex terms is spanned by $w_i^x \otimes w_j^y \otimes w_k^z$, where w_i^α are given by (2.71) and $i, j, k = 1, \ldots, 10$. According to (2.2), in order for a state to satisfy the condensation operators V_{l_μ}, we must have

$$(a_x^z, b_x^y), (a_y^x, b_y^z), (a_z^y, b_z^x) = (1, 1) \text{ or contain no } 1. \tag{2.72}$$

Therefore, we need to count the number of states $w_i^x \otimes w_j^y \otimes w_k^z$ that satisfy (2.72). Up to permutation of x, y and z, we have four cases:

(1) If none of the a's or b's (and hence c's) is 1, then the states are $w_i^x \otimes w_j^y \otimes w_k^z$ where $i, j, k = 7, 8, 9$ or 10. There are $4 \times 4 \times 4 = 64$ possibilities.

(2) If $(a_z^y, b_z^x) = (1, 1)$ and $(a_x^z, b_x^y), (a_y^x, b_y^z)$ contain no 1, then we can take $i = 2$ or 5, $j = 1$ or 4, and $k = 7, 8, 9$ or 10. There are $2 \times 2 \times 4 = 16$ possibilities.

(3) If $(a_x^z, b_x^y), (a_y^x, b_y^z) = (1, 1)$ and (a_z^y, b_z^x) contains no 1, then we can take $i = 1$ or 4, $j = 2$ or 5, and $k = 3$ or 6. There are $2 \times 2 \times 2 = 8$ possibilities.

(4) If all a's and b's are 1, then we can take $i, j, k = 3$ or 6. There are $2 \times 2 \times 2 = 8$ possibilities.

Summarizing these cases, we have

$$\text{GSD} = 64 + 3 \times 16 + 3 \times 8 + 8 = 144,$$

where the factors of 3 account for permutations of x, y and z. The result agrees with (2.1).

Chapter 3

FRACTON PHASES: GENERALIZED FOLIATION

In Chapter 2, we have shown that the Ising cage-net is not foliated according to the definition of (original) foliation [32, 52]. Yet, the Ising cage-net model shares many features with the X-cube model, which is known to be foliated (we review this in Sec. 3.1). Both models host fractons, lineons, and planons, and can be built by coupling intersecting stacks of 2D topologically ordered systems [41, 42]. A natural question then arises: can we find a generalized RG scheme such that the Ising cage-net is a fixed-point model? In this Chapter, we answer this question in the affirmative. We find that the original foliation can be naturally extended to *the generalized foliation scheme*, under which the Ising cage-net is a fixed-point.

This Chapter is organized as follows. After a review of the original foliation in Sec. 3.1, we point out some unnatural restrictions within the (original) foliated RG in Sec. 3.2, and proposes the generalized foliated RG where these restrictions are removed. In Sec. 3.3, we show that the Ising cage-net model is foliated in terms of a generalized foliated RG defined by planon condensation. Then, in Sec. 3.4, we demonstrate that the generalized foliated RG can also be implemented by a planar linear depth circuit. The linear depth circuit has a special structure, and we dub it a sequential circuit; in Sec. 3.5 we show how the sequential circuit we use is closely related to the condensation of planons via gapped boundaries.

3.1 (Original) foliation and the X-cube model

Before our discussion of the 'generalized foliation', it is instructive to review the original notion of foliation and see how the corresponding RG procedure is carried out for the X-cube. The X-cube model has a foliated structure, where layers of the toric code can be added to or removed from the X-cube via a finite depth circuit $\mathcal{S}$ [52]. Given an X-cube ground state $|\Psi_{\text{X.C.}}\rangle$ of the system size $L_x \times L_y \times L_z$ and a toric code ground state $|\Psi_{\text{T.C.}}\rangle$, $\mathcal{S}$ yields a $|\Psi_{\text{X.C.}}\rangle$ of the size $L_x \times L_y \times (L_z + 1)$. In rest of this section, we review the finite depth circuit $\mathcal{S}$ on the three-torus.

Let us consider the X-cube Hamiltonian defined on a cubic lattice on the three-torus; and one copy of the toric code Hamiltonian defined on a square lattice on the two-torus. For both models, the local qubit DOFs are placed on the edges. The X-cube

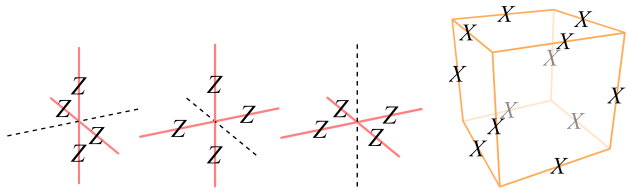

(a) (b)

Figure 3.1: (a) The three types of vertex terms in the X-cube Hamiltonian A_v^x, A_v^y, and A_v^z, which are tensor products of Pauli-Z operators. (b) The cube term B_c.

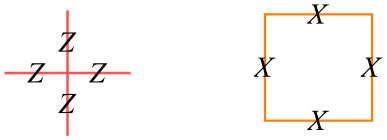

(a) (b)

Figure 3.2: (a) The vertex term Q_v in the toric code Hamiltonian. (b) The plaquette term B_p.

Hamiltonian [25]

$$H_{\text{X.C.}} = -\sum_v \left(A_v^x + A_v^y + A_v^z\right) - \sum_c B_c \tag{3.1}$$

contains three types of vertex terms A_v^x, A_v^y, and A_v^z; and one type of cube term B_c, as shown in Fig. 3.1. The toric code Hamiltonian [17]

$$H_{\text{T.C.}} = -\sum_v Q_v - \sum_p B_p \tag{3.2}$$

is a sum of local terms as shown in Fig. 3.2.

To construct the circuit, we first insert a decoupled toric code into the X-cube. As depicted in Fig. 3.3, when the inserted toric code lies in the xy-plane, it bisects the z-direction edges in the X-cube model, thus creating new qubit edges k' colored in orange. These new k' edges are added to the system as product states whose Hamiltonian is chosen to be $H_0 = -\sum_{\{k'\}} Z_{k'}$. For each bisected edge i in the X-cube Hamiltonian, we substitute $Z_i \to Z_{i'}$ and $X_i \to X_{i'}$.

The circuit $\mathcal{S}$ is a product of two finite depth circuits $\mathcal{S}_2$ and $\mathcal{S}_1$, $\mathcal{S} = \mathcal{S}_2\mathcal{S}_1$. Each is a product of the controlled-NOT (CNOT) gates. The circuit $\mathcal{S}_1$ acts on the edges of the modified X-cube Hamiltonian, as shown in Fig. 3.4a. Every CNOT gate in $\mathcal{S}_1$ has an i' edge serving as the controlled qubit and the corresponding k' edge as the target. On the other hand, $\mathcal{S}_2$ acts on both edges of the X-cube and those of the toric code. Every edge of the toric code serves as the controlled qubit for the CNOT

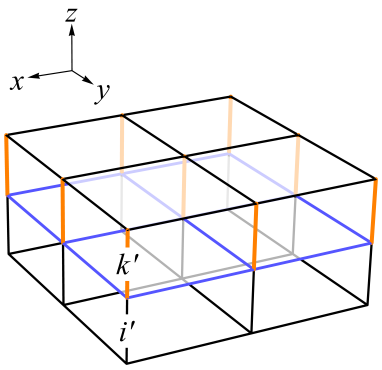

Figure 3.3: The insertion of a layer of toric code living on an xy-plane (blue colored square lattice) into a cubic lattice, which hosts the X-cube. The inserted layer bisects an edge i near the inserted plane into edges labeled by i' and k'. For every bisected edge, the X-cube Hamiltonian is modified by replacing $Z_i \to Z_{i'}$ and $X_i \to X_{i'}$. The new edges k' are product states with the Hamiltonian of $H_0 = -\sum_{\{k'\}} Z_{k'}$.

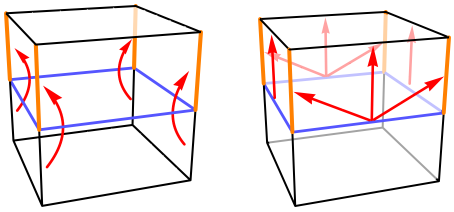

(a) (b)

Figure 3.4: An illustration of the finite depth circuit $\mathcal{S} = \mathcal{S}_2\mathcal{S}_1$. (a) The action of the circuit $\mathcal{S}_1$ when focus on an elementary cube of the original cubic lattice. The arrows, representing the CNOT gates, point from the controlled qubits to the targets. (b) $\mathcal{S}_2$'s action viewed at a cube.

gates whose targets are edges in the modified X-cube. An illustration of $\mathcal{S}_2$ is given in Fig. 3.4b. The CNOT gate, acting by conjugation, has the actions of

$$\begin{aligned} ZI &\mapsto ZI, \quad IZ \leftrightarrow ZZ, \\ XI &\leftrightarrow XX, \quad IX \mapsto IX, \end{aligned} \tag{3.3}$$

where the first qubit is the control and the second is the target. All the CNOT gates in $\mathcal{S}_1$ or $\mathcal{S}_2$ commute with each other. Therefore, $\mathcal{S}$ is a finite depth circuit. By direct computation, we see that

$$\mathcal{S}\left(\tilde{H}_{\text{X.C.}}^{(L_x,L_y,L_z)} + H_{\text{T.C.}} + H_0\right)\mathcal{S}^\dagger \cong H_{\text{X.C.}}^{(L_x,L_y,L_z+1)}, \tag{3.4}$$

where $\tilde{H}_{\text{X.C.}}$ is the modified X-cube Hamiltonian, and the symbol $\cong$ denotes that the L.H.S. and the R.H.S. share the same ground space.

3.2 Generalizing the notion of foliation

The calculation of the GSD for Ising cage-net model shows that it is not foliated in the usual sense (recall from Chapter 2). However, from its construction in terms of stacks of 2D topological orders, it is reasonable to expect that it may be foliated in some generalized sense. Indeed, once we examine the original defnition of foliation in more detail, we can uncover two parallel ways in which it is unnaturally restrictive.

First, let us formulate the original foliated RG process purely in terms of quantum circuits. Recall that foliated RG in the X-cube model involves adding a topologically ordered layer and then coupling it to the X-cube bulk with a finite-depth quantum circuit. The topological layer cannot itself be created with a finite-depth circuit from a product state. However, it is now well-understood that it can be created with a linear-depth circuit [83, 84]. Therefore, if we view foliated RG as a generalization of usual entanglement RG [85, 86], in which one is allowed to add ancillary degrees of freedom in a product state and then apply finite-depth circuits, moving to foliated RG corresponds to additionally allowing linear-depth circuits within a 2D subsystem of the 3D model. However, from this perspective, the current definition of foliated RG is restricted, in that we only allow the linear-depth circuit to act on the ancillae qubits and not on the 3D bulk. A more natural definition would be to allow the linear-depth circuit to act arbitrarily within a 2D layer on both the ancillae and the bulk. We remark that the kinds of linear-depth circuits involved here have a special structure that preserves the area law of entanglement, as discussed in more detail in Sec. 3.5.

Second, we can also view foliated RG in terms of condensation. Namely, suppose we want to implement the inverse process of removing a single layer from the X-cube model, reducing its size in one direction. This can be achieved by condensing a planon within a single layer, corresponding to disentangling the toric code layer and then trivializing that layer by condensing a boson. In this case, the planon which we condense is very special: it can be viewed as being part of a 2D theory that is decoupled from the rest of the excitation spectrum of the 3D bulk. To be more general, if we allow condensation of planons in RG, we should allow condensation of arbitrary planons, not only those that are part of decoupled 2D theories.

In light of the above, there are two natural ways to extend the notion of foliated RG: linear-depth circuits and planon condensation. In what follows, we will show that both approaches lead to a generalized foliated RG that is applicable to the Ising cage-net model. Then, in Sec. 3.5, we argue that these two approaches, while

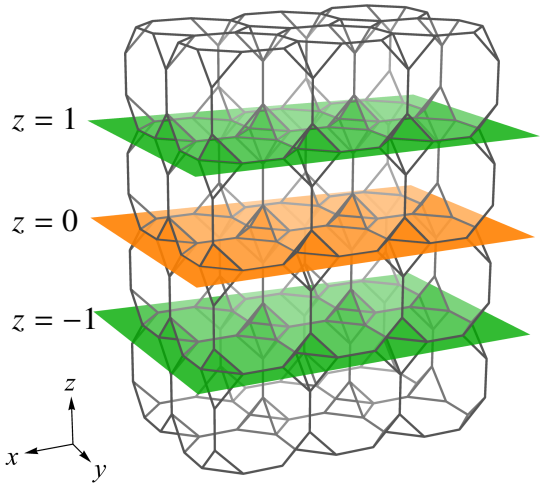

Figure 3.5: An illustration of the relevant xy-planes of a $L_x \times L_y \times L_z$ Ising cage-net. Via the condensation process described in the text, we remove the $z = 0$ plane and obtain a $L_x \times L_y \times (L_z - 1)$ Ising cage-net.

seemingly distinct, are in fact very closely related to each other.

3.3 RG via condensation

How can the system size of the Ising cage-net model be increased / decreased? In this section, we show that it can be changed through condensation and un-condensation of bosonic planons. This is closely tied to the topic of anyon condensation in 2D systems, which we briefly review in Appendix 3.7. For a comprehensive review, we refer the reader to Ref. [87] and references therein.

Let us begin by considering the process of condensing planons in an xy-plane to decrease the system size in the z direction by one (Fig. 3.5). Recall from the last section that for each xy-plane there is a bosonic planon $\psi\bar{\psi}$ which can be condensed. When $\psi\bar{\psi}$ in plane $z = 0$ is condensed, the quasi-particle content of the model changes as follows:

1. Since $\psi\bar{\psi}$ is the fracton dipole, fractons between planes $z = 0$ and $z = 1$ are identified with the corresponding fracton between planes $z = -1$ and $z = 0$.

2. The planons ψ and $\bar{\psi}$ on the $z = 0$ plane are identified.

3. The $\sigma\bar{\sigma}$ planon on the $z = 0$ plane splits into two abelian bosonic planons e and m with a mutual -1 braiding statistics.

4. The lineons in the $z = 0$ plane composed of $\sigma_{xy}\sigma_{xz}$, $\bar{\sigma}_{xy}\sigma_{xz}$, $\sigma_{xy}\bar{\sigma}_{xz}$, and $\bar{\sigma}_{xy}\bar{\sigma}_{xz}$ are all confined.

5. Planons and lineons on other planes are unchanged.

After this step, we can further condense either e or m. This gets rid of the remaining planons on the $z = 0$ plane without affecting other quasi-particle excitations. Now, we see that the quasi-particle content of the model is the same as that of an Ising cage-net model with the $z = 0$ plane removed. The planons and lineons on planes other than $z = 0$ are left intact. Moreover, the fracton between $z = 0$ and $z = 1$, which is now identified with the fracton between $z = -1$ and $z = 0$, becomes the new fracton between $z = -1$ and $z = 1$. Therefore, the size of the Ising cage-net model can be decreased by one in the z direction by first condensing the $\psi\bar{\psi}$ planon in a plane, and then by condensing one of the split channels of the $\sigma\bar{\sigma}$ planon on the same plane.

We see that if we allow condensation of bosonic planons as a RG operation, we obtain a generalized foliated RG under which the Ising cage-net model is a fixed point. As noted in Sec. 3.2, the original foliated RG for the X-cube model can also be viewed in terms of such condensation.

The condensation of planons is, of course, a singular process where the bulk gap needs to close and then reopen, corresponding to a phase transition between different phases. This means that, similar to the original foliated RG, the generalized foliated RG operations can move across certain phase boundaries. However, only certain phase boundaries can be crossed; the singularity involved in planon condensation is localized to a selected plane and is hence a “subsystem" singularity, not one in the full 3D bulk.

A useful way to think about the condensation process is to use the fact that the Ising cage-net model can be obtained by gauging the planar Z_2 symmetries of a subsystem symmetry protected topological (SSPT) model protected by the planar symmetries[1]. Note that, subsystem symmetries usually contain generators associated with rigid subsystems like x, y, z planes in the 3D bulk. They are different from higher-form symmetries [88] with generators associated with deformable subsystems. The planons being condensed correspond to the symmetry charges of the planar symmetries in the SSPT model. Hence the condensation of the planons in a given plane corresponds to breaking / removing that planar symmetry and reducing the size of the model. On the other hand, if we want to increase the size of the system by adding

[1] to be discussed in future work

a plane at $z = 0$, we need to add the planar symmetry and the corresponding planar state back to the SSPT model and 're-gauge' the planar symmetry.

3.4 RG via planar linear depth circuit

The planar linear depth circuit we construct for the Ising cage-net model is a direct generalization of a RG scheme that maps product states to ground states of a string-net model, introduced by Liu Y. *et al.* [84]. We review this RG procedure for the string-net models. We describe carefully an initialization step that is nontrivial for non-abelian string-net models, which was not discussed in detail in Ref. [84]. Then, we describe the RG scheme as a linear depth circuit for the Ising cage-net model. We will see that the initialization step is also important and nontrivial.

String-net RG

In this section, we will first describe an important step in the RG procedure – the 'controlled gate' which adds a plaquette to the string-net wave-function. After that, we will describe the full RG procedure starting from the string-net wave-function on the minimal lattice on a torus and then adding plaquettes row by row. A brief review of the string-net models is given in Appendix 2.9.

Adding plaquettes via the controlled gate

The controlled gate can be used to add a plaquette to the string-net wave-function. We present the definition and properties of the gate in this sub-section. Computational details of the results discussed here can be found in Appendix 3.6.

Suppose that on a trivalent lattice, a plaquette is added by adding an edge (the red edge in the diagrams below), and we want to extend the string-net wave-function from the original lattice to that including this new plaquette. When the edge is added, it is not entangled with the rest of the lattice and is in the state $|0\rangle$. To merge the added edge into the lattice, first, map it to $\sum_s \frac{d_s}{\sqrt{D}}|s\rangle$ where D is the total quantum dimension of the string-net.

$$|0\rangle \mapsto \sum_s \frac{d_s}{\sqrt{D}}|s\rangle \tag{3.5}$$

Then, we use this edge as the control to draw loops around the added plaquette. More specifically, we can represent the controlled gate $G_p = \sum_s G_p^s$ graphically as in Eq. (3.6). The action of G_p^s is similar to the action of B_p^s which adds a loop s to a plaquette, but for the graphical evaluation of G_p^s, we treat the control edge as if it

is in the state $|0\rangle$, i.e.

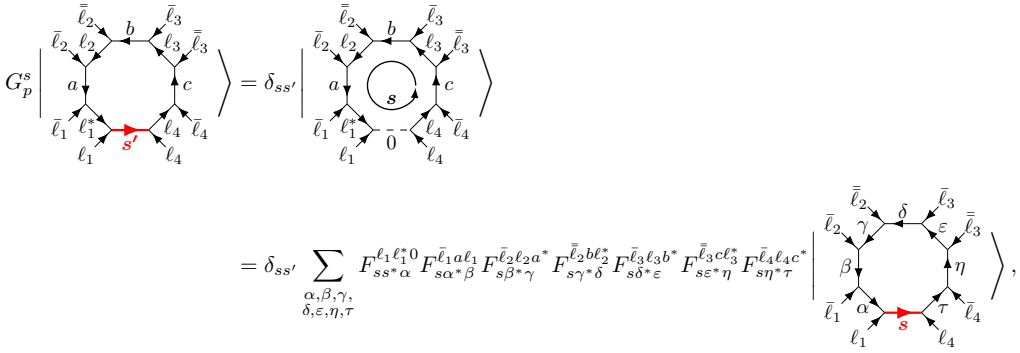

(3.6)

where the red line with an arrow marks the control edge. We carry out the explicit graphical evaluation in Appendix 3.6. Note that G_p^s can be defined on any polygonal plaquette.

G_p^s is not a unitary on the full Hilbert space, but only between subspaces. More specifically, it is an isometry from $\mathcal{V}_{p,s}^{\mathrm{SN}}$ to $\mathcal{H}_{p,s}^{\mathrm{SN}}$, both of which involve the DOF around a plaquette p. In $\mathcal{V}_{p,s}^{\mathrm{SN}}$, the control edge is set to $|s\rangle$ while the other edges come from the string-net wave-function on the lattice with the control edge missing (pretending that it is set to $|0\rangle$). The vertices containing the control edge, then, involve configurations like

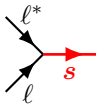

(3.7)

In $\mathcal{H}_{p,s}^{\mathrm{SN}}$, all edges, including the control edge, come from the string-net wave-function with the control edge set to $|s\rangle$.

In Appendix 3.6, we prove that G_p^s is an isometry from $\mathcal{V}_{p,s}^{\mathrm{SN}}$ to $\mathcal{H}_{p,s}^{\mathrm{SN}}$ by demonstrating

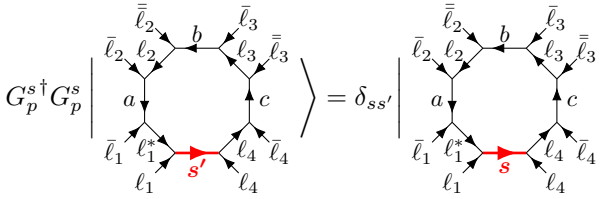

(3.8)

The controlled gates commute with each other

$$\left[G_p^s, G_{p'}^{s'}\right] = 0 = \left[G_p^{s\,\dagger}, G_{p'}^{s'}\right], \tag{3.9}$$

as long as they do not act on each other's controlled edge. Moreover, we can show

$$\left[G_p^s, B_{p'}^{s'}\right] = 0 = \left[G_p^{s\,\dagger}, B_{p'}^{s'}\right], \tag{3.10}$$

provided that $B_{p'}^{s'}$ does not act on the control edge of G_p^s. We prove these commutation relations in Appendix 3.6.

In Appendix 3.6, we prove a useful equation, which we call *the central equation*

$$G_p^s \left(|s\rangle \langle s'|\right)_{\text{ct}} G_p^{s'\dagger} = P_{\text{ct}}^s \left(\sum_k \frac{d_k}{d_s d_{s'}} B_p^k \right) P_{\text{ct}}^{s'}, \tag{3.11}$$

where $\left(|s\rangle \langle s'|\right)_{\text{ct}}$ acts on the control edge and $P_{\text{ct}}^s = |s\rangle \langle s|$ is a projector on the control edge. With the central equation, we can show that the controlled gate does what we claimed – it adds a plaquette to the string-net wave-function. In particular, we show below that under conjugation by $G_p = \sum_s G_p^s$, the projector on the control edge $P_{\text{ct}} = \sum_{s,s'} \frac{d_s d_{s'}}{D} |s\rangle\langle s'|$ is mapped to the plaquette projector $B_p = \sum_s \frac{d_s}{D} B_p^s$.

$$\begin{aligned} G_p P_{\text{ct}} G_p^\dagger &= \sum_{s,s'} \frac{d_s d_{s'}}{D} G_p^s \left(|s\rangle\langle s'|\right)_{\text{ct}} G_p^{s'\dagger} \\ &= \sum_{s,s',k} \frac{d_k}{D} P_{\text{ct}}^s B_p^k P_{\text{ct}}^{s'} \\ &= \sum_k \frac{d_k}{D} B_p^k = B_p \end{aligned} \tag{3.12}$$

The RG circuit

Using the controlled gate as a building block, we can construct the full linear depth circuit that maps a product state to the string-net wave-function. We present the linear depth circuit in two steps: 1. from a product state to a string-net wave-function on the minimal lattice on torus; 2. from the string-net wave-function on the minimal lattice to the full lattice by adding plaquettes. We are going to focus on the trivalent square-octagon lattice, although the general procedure applies to other trivalent graphs as well.

The minimal lattice on the torus consists of three edges, two vertices, and one plaquette, as shown in Fig. 2.11. On the square-octagon lattice, we start from the product state $\otimes_l |0\rangle_l$. Pick three edges around a vertex as shown in Fig. 3.6. Apply a local unitary transformation on the three edges so that they become one of the ground states on the minimal lattice. Note that for abelian string-net states, the ground states can be chosen to be a product state of the three edges. In fact, the $\otimes_l |0\rangle_l$ state is a legitimate state already, because it satisfies the vertex term while the plaquette term is trivial for abelian strings on the minimal lattice (for proof see Appendix 2.9). However, for non-abelian string-nets, the B_p^s term for a non-abelian s-string acts

non-trivially in the stable vertex subspace, and the ground states generally become entangled. In the case of the doubled-Ising on the minimal lattice, ten configurations satisfy the vertex constraints. Of this ten-dimensional space, only nine dimensions belong to the ground space, where $B_p^0 = 1$, $B_p^1 = \sqrt{2}$, and $B_p^2 = 1$. The remaining one dimension carries a $\psi\bar{\psi}$ fluxon excitation such that $B_p^0 = 1$, $B_p^1 = -\sqrt{2}$, and $B_p^2 = 1$. One possible choice of the nine doubled-Ising ground states on the minimal lattice is given in Appendix 2.10.

Now, we need to grow this minimal structure so that it reaches the full extent of the lattice. To do this, we 'copy' the states on the i and j edges along the non-contractible loops in the y and x directions. To achieve this, we use controlled gates of the form $\sum_i |i\rangle|i\rangle\langle i|\langle 0|$, and apply them sequentially along the non-contractible loops, as shown in Fig. 3.6. As this step has to be done sequentially along the loop, its depth increases linearly with the size of the lattice. This completes step 1 of the linear depth circuit, which we call initialization.

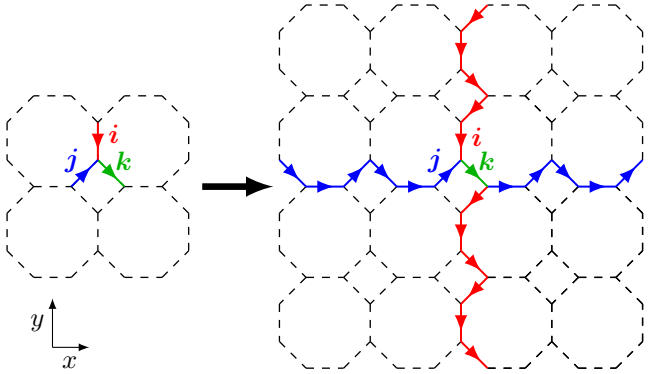

Figure 3.6: The initialization step in the RG circuit for generating the string-net wave-function. Left: pick three edges around a vertex and map them into one of the ground states of the string-net on the minimal lattice. Right: grow the minimal structure by copying the string states $|i\rangle$ and $|j\rangle$ along non-contractible loops so that they reach the full extent of the lattice.

Step 2 is also of linear depth. The minimal lattice has only one plaquette. In step 2, we add more plaquettes to the lattice using the controlled gate introduced in Sec. 3.4. The plaquettes cannot be added all at once, because the controlled gates commute only when they do not act on each other's control edge. A linear depth circuit is hence needed to add all the plaquettes to the square-octagon lattice. A particular sequence for adding these plaquettes is shown in Fig. 3.7. Firstly, all the square plaquettes (red circles) can be added at the same time because they do not overlap with each other. The small circle indicates the control edge while the big circle

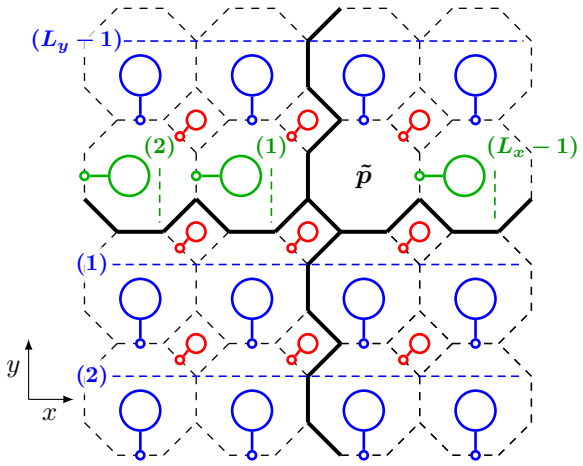

Figure 3.7: Adding loops to plaquettes in step 2 of the RG circuit for generating the string-net wavefunction. The state has been initialized into one of the ground states on the minimal lattice (black lines). First, loops are added to the square plaquettes (shown in red) in a single step. Then, loops are added to octagon plaquettes in row (1), (2), ... $(l_y - 1)$ sequentially. For the last row, loops are added to octagon plaquette in column (1), (2), ..., $(L_x - 1)$ sequentially. No action is needed in the last plaquette $\tilde{p}$.

indicates the action of G_p^s. Secondly, we add the square-octagon lattice in row one (labeled (1) in Fig. 3.7). All controlled gates in row one commute with each other so they can be added in one step. Then we add row two, row three, etc., until the next to last row (labeled $(L_y - 1)$ in Fig. 3.7). For the last row, we need to choose the control edges side ways because we need un-entangled edges to be used as control edge. Due to this change, the plaquettes in the last row need to be added sequentially as the controlled gates do not commute any more. As shown in the figure, we can add them in the order of (green labels) (1), (2), ..., $(L_x - 1)$. We do not need to act in the last plaquette (labeled $\tilde{p}$) as the constraint due to the last plaquette is already implied by that of the largest plaquette that we started from combined with all the small plaquettes added so far. Therefore, at this point, we have finished the linear depth RG procedure that starts from a product state and maps it to the the string-net wave-function on the square-octagon lattice.

Ising cage-net

In this section, we use the controlled gate of Eq. (3.6) to build up the RG circuit to enlarge an Ising cage-net ground state on the three-torus by one layer. We will start, in Sec. 3.4, by introducing finite depth circuits that grow cages on the cage-net ground state. They serve as the building blocks of the full planar linear depth RG

circuit, which we discuss in Sec. 3.4.

Adding cages via the controlled gate

In 2D, we have seen that a plaquette can be added to the string-net wave function, via the controlled gates, after an edge is added to the lattice. We can extend this procedure to 3D cage-net states.

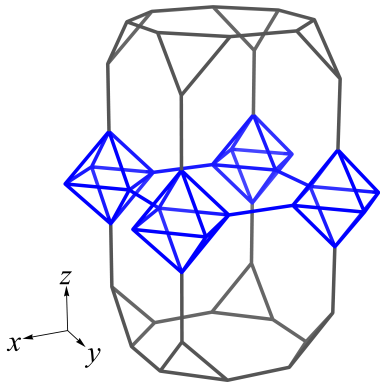

Figure 3.8: Insertion of an xy-plane bisects a cube in the original cage-net lattice into two cubes. Each intersection point between the xy-plane and the z-principal edges is expanded into an octahedron to preserve the trivalent structure in the xy, yz and zx planes.

Suppose that we start with the Ising cage-net ground state on the truncated cubic lattice (Fig. 2.2) and add a plane in the xy direction. At each point where the added plane bisects the z direction edges, an octahedron is added, as shown in Fig. 3.8, to ensure the trivalent structure in each of the coupled planes. In the added plane, octagonal plaquettes fill in the space between the octahedrons. Every edge of the added octahedrons carries a three dimensional Hilbert space spanned by $\{|0\rangle, |1\rangle, |2\rangle\}$. We start with these edges all set to the state $|0\rangle$. The principal edges on the octagons each carry a five dimensional Hilbert space spanned by $\{|00\rangle, |02\rangle, |20\rangle, |22\rangle, |11\rangle\}$, which is a subspace of the tensor product Hilbert space of two three dimensional DOFs $\{|0\rangle, |1\rangle, |2\rangle\} \otimes \{|0\rangle, |1\rangle, |2\rangle\}$ that come from the two intersecting planes. We start with these principal edges in the state $|00\rangle$.

We describe first the process to add one cube into the new layer, which consists of two steps: 1. add the octahedrons to the cage-net wave-function; 2. grow a cage structure in the upper truncated cube of Fig. 3.8. In step one, we first need to copy the state of the bisected z-principal edge onto some of the octahedron edges so that the vertex rules are satisfied at the octahedrons' vertices. Suppose the bisected edge is in the state $|xy\rangle$. The copying process can be achieved with

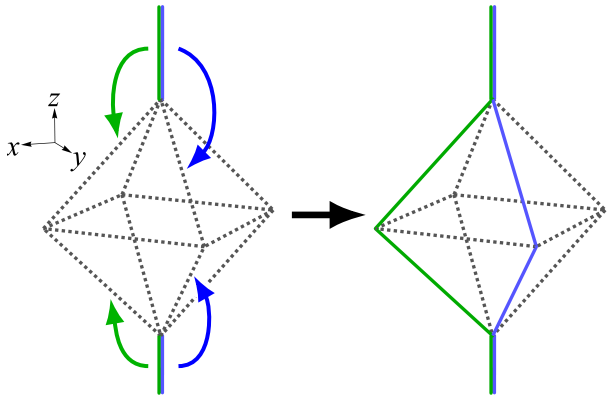

Figure 3.9: 'Copying' the states on the bisected z-principal edges onto edges of the added octahedron to satisfy vertex rules in the xz and yz planes. The copying process can be performed by controlled gates of the form $\sum_{xy} |xy\rangle\langle xy| \otimes |x\rangle\langle 0|$ and $\sum_{xy} |xy\rangle\langle xy| \otimes |y\rangle\langle 0|$, indicated by the arrows pointing from the control to the target.

the controlled gates $\sum_{xy} |xy\rangle\langle xy| \otimes |x\rangle\langle 0|$ and $\sum_{xy} |xy\rangle\langle xy| \otimes |y\rangle\langle 0|$ as indicated by the blue and green arrows in Fig. 3.9. Then, we add the square plaquettes to the cage-net wave-function. This can be done as described in the previous section on how to add a square plaquette to the doubled-Ising string-net wave function, as the square plaquettes remain unaffected when the doubled-Ising layers are coupled into Ising cage-net. More specifically, for each square plaquette, we pick an edge in the state $|0\rangle$ as the control edge, map it to $\sum_s \frac{d_s}{\sqrt{D}}|s\rangle$, and use it as the control in the controlled gate G_p that adds loops into the plaquette.

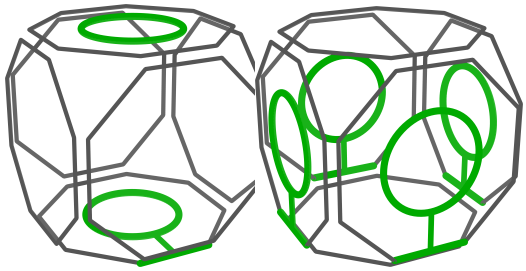

(a) (b)

Figure 3.10: Growing a cage structure in an added cube. (a) First, using an edge from the bottom face (colored green) as control, add loops to the bottom and top faces, (b) then use the edges on the side faces (colored green) as control to add loops to the side face.

Step 2, which adds a cage structure to the cube, is more complicated. As shown in Fig. 3.10, first we add loops to the bottom and top faces and then to the side faces. More specifically, first we pick a principal edge on the bottom face in the state $|00\rangle$ as the control. We will use the convention where the first $|0\rangle$ comes from

the xy plane while the second $|0\rangle$ comes from the vertical xz and yz planes. Map the control edge as

$$|00\rangle \mapsto \sum_s \frac{d_s}{\sqrt{D}} |s0\rangle\,, \tag{3.13}$$

Note that this takes the controlled edge out of the five dimensional subspace of $\{|00\rangle, |02\rangle, |20\rangle, |22\rangle, |11\rangle\}$ but keeps it in the nine dimensional space of $\{|0\rangle, |1\rangle, |2\rangle\}^{\otimes 2}$. This will also happen to other principal edges as we implement the procedure, but at the end of the process of growing a cube, all principal edges will be back to the five dimensional subspace.

Now, using the $|s\rangle$ state as the control, apply the controlled gate to the bottom face p_b and top face p_t as

$$G^0_{p_b} + G^2_{p_b} + \frac{1}{\sqrt{2}} G^1_{p_b} B^1_{p_t} \tag{3.14}$$

as shown in Fig. 3.10 (a). Note that $G^s_{p_b}$ and $B^s_{p_t}$ act on the first part of the principal edges (the part that comes from horizontal planes). After these controlled gates, the projector on the control edge $|0\rangle\langle 0|$ (the first part) gets mapped to

$$\begin{aligned} (|0\rangle\langle 0|)_{\text{ct}} &\mapsto \sum_{ss'} \frac{d_s d_{s'}}{D} (|s\rangle\langle s'|)_{\text{ct}} \\ &\mapsto B^0_{p_b} + B^2_{p_b} + B^1_{p_b} B^1_{p_t}, \end{aligned} \tag{3.15}$$

where in deriving the last line, we used the fact that the top face is part of the original cage-net wave-function and $B^0_{p_t} = B^2_{p_t} = 1$. Note that it might seem that the operator in Eq. (3.14) is not unitary as B^1_p is not. But since $B^1_{p_t} {B^1}^\dagger_{p_t} = B^0_{p_t} + B^2_{p_t} = 2$, the action of the operator restricted to the ground space of the original cage-net model is indeed unitary.

Next, we need to add loops to the side faces. To do this, we take the principal edges on the bottom face, which are now in the states $|s0\rangle$ and send them to $|s\alpha_s\rangle$, where α_s comes from the xz or yz planes and $\alpha_s = 0$ if s is even, $\alpha_s = 1$ if s is odd. This brings the principal edges on the bottom face back to the five dimensional Hilbert space. Then map the $|\alpha_s\rangle$ states to

$$|0\rangle \mapsto \frac{1}{\sqrt{2}} (|0\rangle + |2\rangle)\,,\ |1\rangle \mapsto |1\rangle \tag{3.16}$$

Use the $|\alpha_s\rangle$ states as the control to draw loop on the side faces by applying $\sum_{\alpha_s} G^{\alpha_s}_{p_s}$ as shown in Fig. 3.10 (b) to each side face. Let us see how the Hamiltonian terms in Eq. (3.15) transforms. We show the step by step calculation for the third term $B^1_{p_b} B^1_{p_t}$. The $B^1_{p_t}$ part is not affected by the transformation and will be omitted from

the following equation. Let us focus on the transformation induced by on principal edge. We label the two three-dimensional DOFs on the principal edge as 1 and 2 respectively, where 1 comes from the bottom face whose state is labeled by s and 2 comes from the side face whose state is labeled by α_s.

$$\begin{aligned}
&\left[(P_1^0+P_1^2)B_{p_b}^1P_1^1+P_1^1B_{p_b}^1(P_1^0+P_1^2)\right]\otimes(|0\rangle\langle 0|)_2\\
\mapsto&\frac{1}{\sqrt{2}}(P_1^0+P_1^2)B_{p_b}^1P_1^1\otimes(|0\rangle_2+|2\rangle_2)\,{}_2\langle 1|\\
&+\frac{1}{\sqrt{2}}P_1^1B_{p_b}^1(P_1^0+P_1^2)\otimes|1\rangle_2\,({}_2\langle 0|+{}_2\langle 2|)\\
\mapsto&\frac{1}{\sqrt{2}}(P_1^0+P_1^2)B_{p_b}^1P_1^1\otimes\left(P_2^0+P_2^2\right)B_{p_s}^1P_2^1\\
&+\frac{1}{\sqrt{2}}P_1^1B_{p_b}^1(P_1^0+P_1^2)\otimes P_2^1B_{p_s}^1\left(P_2^0+P_2^2\right)
\end{aligned}\tag{3.17}$$

The result is the product of $B_{p_b}^1$ and $B_{p_s}^1$ projected onto the five dimensional subspace of the principal edge, as promised. This works for all side faces. Similar calculations can be carried out for the first two terms in Eq. (3.15). If we put everything together and omit the projection onto the five dimensional subspace of the principal edges, we see the Hamiltonian terms in Eq. (3.15) becomes

$$\left(B_{p_b}^0+B_{p_b}^2\right)\prod_{p_s}\left(B_{p_s}^0+B_{p_s}^2\right)+B_{p_b}^1B_{p_t}^1\prod_{p_s}B_{p_s}^1,\tag{3.18}$$

which is a sum over the desired plaquette terms on the bottom and side faces as well as the cube term on the cube.

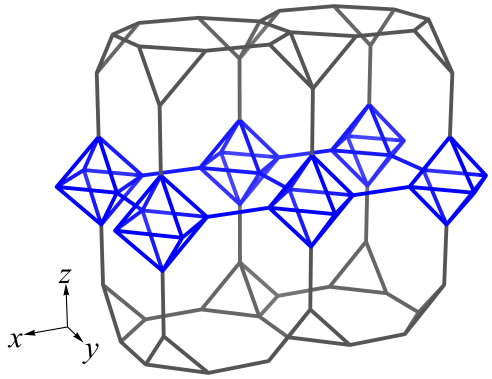

Figure 3.11: Adding a row of cubes to the cage-net state, step 1: the inserted xy-plane bisects the cubes into two; octahedrons are added at the intersection point.

In the RG circuit to be discussed in the next section, we need to grow cubes in the same row at the same time. This works in a similar way as growing a single cube

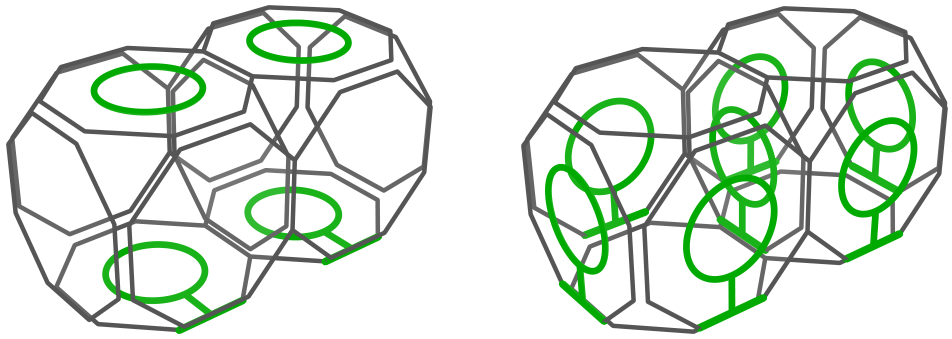

(a) (b)

Figure 3.12: Adding a row of cubes to the cage-net state, step 2: (a) first, we simultaneously add loops to the bottom and the top faces of all cubes in the row; (b), use the edges on the side face (colored green) as control to add loops to all the side faces at the same time.

and we describe the procedure here. First, as shown in Fig. 3.11 which illustrates the situation with two cubes in the row, a new plane is added which bisects the row of cubes into two. Octahedrons are added to the intersection points to preserve the trivalent structure in the coupled xy, yz and zx planes. The 'copying' process illustrated in Fig. 3.9 is then used to restore vertex rules at the vertices of the octahedrons and then the square plaquettes in the octahedrons are added to the cage-net wave-function. The next step is illustrated in Fig. 3.12, which adds cage structures to a whole row of cubes at the same time. This is done by first picking the principal edge in, for example, the x direction and use them as controls to add loops in the bottom and top faces as described above for each cube in the row (Fig. 3.12 (a)). The operations in each cube commute with that in another cube, and hence they can be done all at the same time. Next, loops are added to the side faces using the principal edges on the bottom face as control, as shown in Fig. 3.12 (b). Again, the operations on each side face commute with each other, so they can be done at the same time. As a result of this process, all the cubes in the row are now added to the cage-net wave-function. Note that the process illustrated in Fig. 3.12 applies to the first row in the added plane. When we try to add subsequent rows, some of the side faces would have been added to the cage-net state already. Those side faces can be treated in the same way as the top face. That is, apply $B^1_{p_s}$ in step Fig. 3.12 (a) when the x-principal edge is in the state $|10\rangle$, instead of applying $\sum_{\alpha_s} G^{\alpha_s}_{p_s}$ controlled by the bottom principal edge of the side face in the state $|s\alpha_s\rangle$. A similar procedure applies to the cubes in the last row of the added plane as well, which have to be added one by one.

RG circuit – Ising cage-net

The processes for adding single cubes and a row of cubes are building blocks for the full RG circuit that adds a full plane to the cage-net state. Similar to the case of the doubled-Ising, we first need to initialize the added plane into proper eigenstates of the non-local logical operators before adding the local structures of cubic cages (plaquettes in the case of doubled-Ising).

A commuting set of logical operators of the Ising cage-net ground space can be chosen to be generated by the string-operators of $\psi, \bar{\psi}$ planons in each $\mu\nu$ plane along the μ and ν directions respectively. We can choose the original cage-net state (before adding the plane) to be an eigenstate of all such logical operators. The added xy plane can be initialized into an eigenstate of $\psi^x, \psi^y, \bar{\psi}^x$ and $\bar{\psi}^y$ on that plane. The circuit described in the last section on how to add cubic cages and plaquette terms to the wave-function does not affect these nonlocal logical operators. Therefore, the resulting cage-net state after the RG circuit remains an eigenstate of all the $\psi, \bar{\psi}$ logical operators.

But the choice of the eigenvalue for the $\psi, \bar{\psi}$ logical operators is not arbitrary as the operators are related to each other and hence their eigenvalues are constrained. In Chapter 2, we study carefully the relations among these operators, which allowed us to derive the ground state degeneracy of the Ising cage-net model. The relations are listed below. For derivation, see the discussion in Sec. 2.7. For $\{\mu, \nu, \lambda\} = \{x, y, z\}$

$$\begin{aligned} \prod_i \left(\psi\bar{\psi}\right)^{\mu}_{\mu\lambda}(\nu = i) \prod_j \left(\psi\bar{\psi}\right)^{\nu}_{\nu\lambda}(\mu = i) = 1 \\ r_{\mu\nu}(\lambda = i)\bar{r}_{\mu\nu}(\lambda = i) = 1, \forall i, \forall\{\mu, \nu\} \\ r_{\mu\nu}(\lambda = i)r_{\mu\nu}(\lambda = i + 1) = 1, \forall i, \forall\{\mu, \nu\} \end{aligned} \tag{3.19}$$

where $r_{\mu\nu} = \frac{1}{2}\left(1 + \psi^{\mu}_{\mu\nu} + \psi^{\nu}_{\mu\nu} - \psi^{\mu}_{\mu\nu}\psi^{\nu}_{\mu\nu}\right)$, $\bar{r}_{\mu\nu} = \frac{1}{2}\left(1 + \bar{\psi}^{\mu}_{\mu\nu} + \bar{\psi}^{\nu}_{\mu\nu} - \bar{\psi}^{\mu}_{\mu\nu}\bar{\psi}^{\nu}_{\mu\nu}\right)$. As we started from a ground state of the cage-net model, the original set of $\psi, \bar{\psi}$ operators satisfy the relations in Eq. (3.19). When we add a new xy-plane, we need to make sure that after the new $\psi^x_{xy}, \psi^y_{xy}, \bar{\psi}^x_{xy}, \bar{\psi}^y_{xy}$ operators are added to the original set, the total set still satisfy the relations in Eq. (3.19). This can be guaranteed when the added string-operators satisfy

$$\psi^x_{xy}\bar{\psi}^x_{xy} = 1, \ \psi^y_{xy}\bar{\psi}^y_{xy} = 1 \tag{3.20}$$

$$r_{xy} = \bar{r}_{xy} = \pm 1 \tag{3.21}$$

The choice of ± 1 in the last relation depends on whether $r_{xy}(z = i) = 1$ or -1 in the original set. Compared to the eigenstates listed in Appendix 2.10, $|\Psi^{\text{D.I.}}_{\text{min}}\rangle_1$, $|\Psi^{\text{D.I.}}_{\text{min}}\rangle_5$, $|\Psi^{\text{D.I.}}_{\text{min}}\rangle_9$ satisfy the relations in Eq. (3.20) and $r_{xy} = 1$ while $|\psi\bar{\psi}^{\text{D.I.}}_{\text{min}}\rangle$ satisfies the relations in Eq. (3.20) and $r_{xy} = -1$. Therefore, we can initialize the added layer into one of these states.

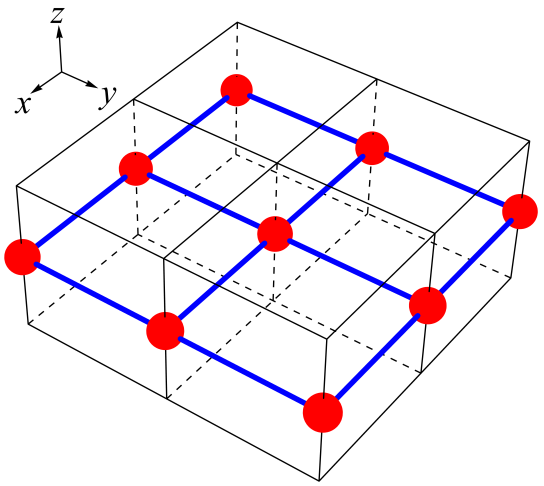

Figure 3.13: Inserting an xy-plane into the original cage-net lattice. Each red ball represents an octahedron. The new principal edges are shown in blue.

In particular, consider the added xy-plane in Fig. 3.13. Each red ball represents an octahedron. The added DOF are initially set to be either in state $|0\rangle$ (on edges of the octahedron) or $|00\rangle$ (on principal edges). Now initialize the trivalent lattice in the xy-plane into one of $|\Psi^{\text{D.I.}}_{\text{min}}\rangle_1$, $|\Psi^{\text{D.I.}}_{\text{min}}\rangle_5$, $|\Psi^{\text{D.I.}}_{\text{min}}\rangle_9$ and $|\psi\bar{\psi}^{\text{D.I.}}_{\text{min}}\rangle$ following the procedure described in Fig. 3.6. This linear depth process set up the stage for the next step of the RG circuit: adding cage structures to the cubes.

Now we can use the procedure described in the last section to add cage structures to the cubes. As shown in Fig. 3.14, on top of the minimal structure set up in the initialization step (red lines), cage structures are added to the cubes in the 1st row, the 2nd row, ... the $(L_y - 1)$th row in each step. In the last row, cage structures are added to the cube in the 1st column, 2nd column, ..., $(L_x - 1)$th column in each step. No action is required in the last cube. This process has depth $\sim (L_x + L_y)$ and completes the addition of a new layer into the cage-net wave-function.

3.5 Relating condensation and linear-depth circuits via gapped boundaries

General discussion

In Sec. 3.3, we discussed the RG process in terms of condensation of planons. In Sec. 3.4, we discussed the RG process in terms of a linear depth circuit. In this

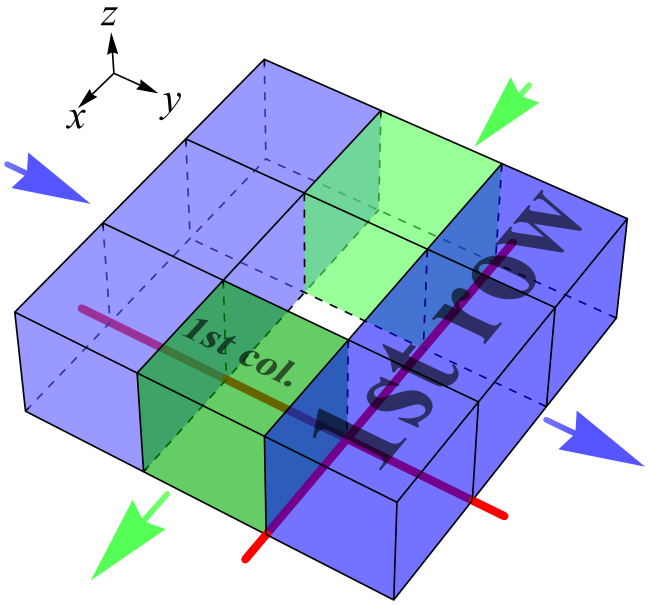

Figure 3.14: Adding cage structures to the cubes in step 2 of the RG circuit for the cage-net state. The red lines indicate the minimal lattice state determined by the initialization step. Cage structures are added to the cubes in the 1st row, the 2nd row, ... the $(L_y - 1)$th row in each step. In the last row, cage structures are added to the cube in the 1st column, 2nd column, ..., $(L_x - 1)$th column in each step. No action is required in the last cube.

section, we show that these two are closely related to each other by understanding each in terms of gapped boundaries.

We first consider a gapped boundary between a 2D topological order and vacuum. If an excitation moves from the bulk to the boundary, it may become trivial in the sense that it can be destroyed by a local operator on the boundary. This phenomenon is referred to as condensation at the boundary. On the other hand, some excitations remain non-trivial as they approach the boundary. These phenomena can be characterized precisely in a category-theoretic language [89–92]; in the abelian case, this amounts to specifying a maximal subset of bosons that can simultaneously condense at the boundary [93–96]. It is believed the universality class of a gapped boundary is fully determined by its category-theoretic characterization.

The above discussion allows us to *define* distinct types of anyon condensation (to vacuum) in a precise way, as distinct types of gapped boundaries (to vacuum). Such a definition is natural if we view the vacuum as a condensate of certain anyons in the 2D topological order. For instance, creating a puddle of anyon condensate within the bulk 2D topological order amounts to creating a puddle of trivial state (vacuum) separated from the bulk by a gapped boundary. This discussion, and the definition

of anyon condensation in terms of gapped boundaries, can be generalized to gapped boundaries between arbitrary 2D topological orders.

In the context of generalized foliated RG, we consider condensation of planons. Condensation of a single planon can similarly be associated with – and defined in terms of – certain gapped boundaries between two fracton orders, with the property that the boundary should be transparent to mobile excitations away from the selected plane where the condensation occurs. It will be an interesting problem for future work to fully characterize those boundaries between fracton phases that correspond to planon condensation. We note that there has been some related prior work discussing gapped boundaries of fracton models in terms of condensation [97, 98].

It turns out that the kind of linear-depth circuits considered here can also be associated with a type of gapped boundary. A linear depth circuit has the general form $\mathcal{U} = \prod_{\ell=1}^{K} U_\ell$ where each layer U_ℓ consists of a number of local unitary gates with non-overlapping support, and the number of layers K is proportional to the linear system size L. In general, U_ℓ can contain gates acting across the entire system. However, for the circuits we employed for RG, each layer U_ℓ only contains gates acting in a lower dimensional subsystem of the entire system, such as the rows in Figs. 3.7 and 3.14. Such circuits are much more restrictive than generic dense linear-depth circuits, particularly because they preserve the area law when acting on a state. We call this class of circuits *sequential circuits*.

Again we first focus on the 2D case, where as we have discussed, sequential circuits can be used to generate topologically ordered ground states from an initial product state (the topological "vacuum"). In order to avoid complications associated with periodic boundary conditions, we make a simplification as compared to the circuits discussed in Sec. 3.4; namely, we work with an infinite system and consider circuits that generate a disc of 2D topological order from vacuum. If desired, the size of the disc can later be taken to infinity. This allows us to drop the initialization step, whose role is to take care of the non-trivial ground state degeneracy on a 2-torus. We can also drop the final linear-depth sequence of gates needed to stitch two gapped boundaries together in a manner consistent with periodic boundary conditions.

With these simplifications, the circuits operate in the following way. We slice the 2D space into 1D concentric circles surrounding the center of the disc, and order these subspaces according to their radial coordinate. The ℓth layer of the circuit is assumed to be supported near (but not entirely within) the ℓth circle. After applying some number of layers of the circuit, one is left with a disc of topological order

which has a gapped boundary to the vacuum region which has not yet been acted on by the circuit. Then, the next layer in the circuit acts only within the vicinity of the one-dimensional gapped boundary between the topological order and the vacuum. The action of the unitary in this layer is to "grow" the topological order by a small amount, pushing the gapped boundary further into the vacuum region. Continuing in this way allows one to grow the topologically ordered region arbitrarily.

Based on the above, given a sequential circuit, we can associate the universality class of the gapped boundary to vacuum which emerges when the circuit is truncated at some radius. This association is well-defined in the following sense. We can define a truncation of the circuit $\bar{\mathcal{U}} = \prod_{\ell=1}^{K_0} U_\ell$ where $K_0 < K$. This will create a disc of topological order with a particular gapped boundary to vacuum. Now, consider a different truncation $\bar{\mathcal{U}}' = \prod_{\ell=1}^{K_0} V_\ell$ where each V_ℓ again consists of non-overlapping gates such that $V_\ell = U_\ell$ for ℓ sufficiently less than K_0, but the layers near the boundary may differ. By definition, the two truncated circuits differ only by a finite-depth circuit near the boundary. But a 1D finite depth circuit cannot change the universality class of the gapped boundary, *i.e.* it cannot change the set of anyons which can condense on the boundary. So the gapped boundary type is independent of how the sequential circuit is truncated. We note this conclusion only holds for truncations that are compatible with the 1D layer structure of concentric circles; the key property is that the truncation only cuts through a finite number of 1D layers, which is bounded above as the size of the disc increases.

We emphasize that this discussion can be generalized to gapped boundaries between two different 2D topological orders. That is, given two topological orders referred to as A and B that admit a gapped boundary, an A-ground-state can be converted into a B-ground-state by applying a sequential circuit. Or, if we apply a truncated version of the same sequential circuit, we can create a puddle of B within the bulk topological order A, separated by a gapped boundary whose universality class does not depend on how the circuit is truncated.

In formulating the generalized foliated RG in terms of quantum circuits, we apply sequential circuits within 2D layers of a 3D fracton model. Truncating such a sequential circuit (along its 1D layer structure) results in a gapped boundary between two different fracton orders, where some of the mobile excitations may condense along the layer where the circuit is applied. This is how we described planon condensation above, and thus we propose that planon condensation and applying 2D sequential circuits are different ways to realize the same operation in generalized

foliated RG.

Condensation in the Ising cage-net circuit

In accordance with the above discussion, we now identify the type of gapped boundary that is associated with the sequential circuits used to create Ising cage-net model. To accomplish this, we are going to apply the circuit only to a finite disc-shaped region within a plane; we will not take the limit that the size of the disc goes to infinity. Inside the region, we get the fracton order as expected. Outside of the region, the added degrees of freedom remain unentangled. There is a gapped boundary between the two sides. We show that the gapped boundary and the region outside can be obtained by condensing bosonic planons starting from a complete fractonic state.

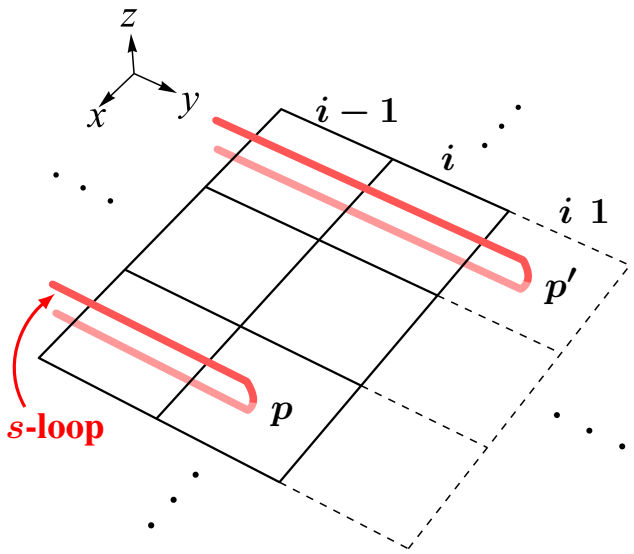

Figure 3.15: Condensation of the $\psi\bar{\psi}$ and the $\sigma\bar{\sigma}$ fluxons on the smooth boundary of the doubled-Ising model. The vertex details are omitted. The dashed lines represent the unentangled edges. An open ended fluxon string-operator is constructed from a loop of s-string that passes through the lattice plane vertically at a plaquette. If the plaquette (for example, the one labeled p) lies within the doubled-Ising region, it creates a fluxon excitation. If the plaquette (for example, the one labeled p') falls outside the string-net region, then no excitation is generated. Thus, all fluxons condense on the smooth boundary. For computational details on the condensation, see Appendix 2.10.

First, let's see how a similar relation works in the doubled-Ising string-net state. We imagine a very large disc of string-net state, and we ignore the curvature of the disc's boundary to simplify the following discussion. Recall that in the RG circuit, the plaquettes are added row by row. Suppose that we stop the process at row i.

The boundary between row i and row $i+1$ is a smooth boundary on the lattice. As the Hamiltonian terms remain commuting throughout the process, the boundary is gapped.

The gapped boundary can be induced by the condensation of 'fluxon excitations'[77] $\psi\bar{\psi}$ and $\sigma\bar{\sigma}$ on the boundary and beyond. To see that, consider a string-operator of the form shown in Fig. 3.15, which consists of a string segment above the lattice, a parallel segment under the lattice and the two are connected by segments that vertically go through the lattice plane. Note that, while embedded in the 3D space, the string-operator is a closed loop, from the 2D perspective, it ends at the locations where the string goes through the lattice plane and can create excitations at those points. In particular, such string-operators in general violate the plaquette term at their ends, as the plaquette terms correspond to a loop operator that links with the string-operator and the linking generates nontrivial action. Therefore, in the bulk of the string-net state, the string-operator generates 'fluxon excitations' at its ends. In the doubled-Ising model, there are two string-operators of this type, corresponding respectively to a loop of string type 1 and a loop of string type 2. The two string-operators generate the $\psi\bar{\psi}$ and $\sigma\bar{\sigma}$ excitations, respectively. If the string-operator ends (goes vertically through the lattice plane) outside of the smooth boundary (Fig. 3.15), there are no more plaquette terms to violate and the string-operator does not generate any excitations. Detailed calculations can be found in Appendix 2.10. Therefore, the $\psi\bar{\psi}$ and $\sigma\bar{\sigma}$ excitations condense on the boundary and beyond, thus demonstrating the connection between anyon condensation and the linear depth circuit for the doubled-Ising string-net state.

The situation is very similar in the Ising cage-net model. The RG circuit is again implemented row by row in a sequential manner. Suppose that we stop the process at row i, there will be a gapped boundary between row i and row $i+1$. As shown in Fig. 3.16, like for the string-nets, a vertical loop operator that goes through the lattice plane at two points generates planon excitations $\psi\bar{\psi}$ and $\sigma\bar{\sigma}$ in the bulk of the cage-net state (in rows $j \leq i$). Beyond row i, however, it does not generate any excitations and hence the $\psi\bar{\psi}$ and $\sigma\bar{\sigma}$ are condensed. This agrees with the RG procedure driven by condensation described in Sec. 3.3. Therefore, the process of sequential application in the linear depth circuit can be interpreted as moving the boundary between the cage-net state and the condensed state, hence enlarging or shrinking the fracton order in the plane.

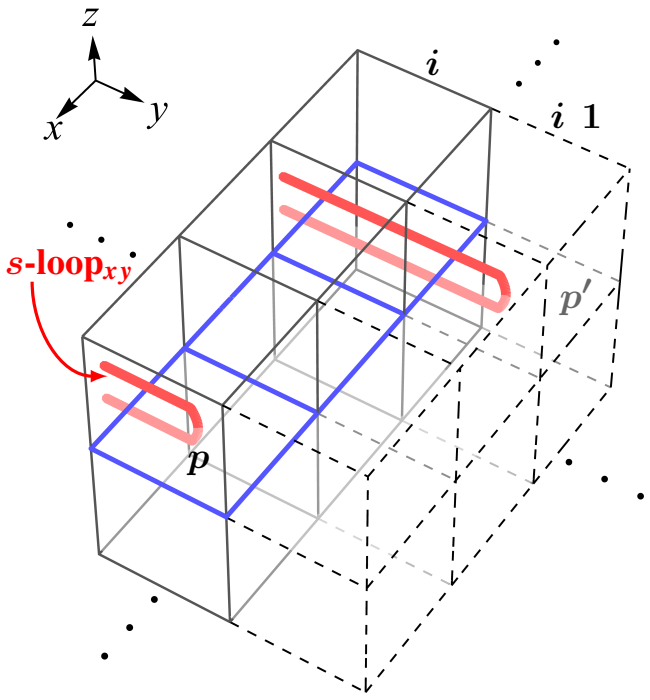

Figure 3.16: Condensation of the $\psi\bar{\psi}$ and the $\sigma\bar{\sigma}$ fluxon excitations in the half xy-plane (shown in blue) in the Ising cage-net. If the end of the the fluxon string operator falls within the Ising cage-net region (for example at the plaquette p), a fluxon excitation is created. If the end falls outside of the Ising cage-net region (for example at the plaquette p'), then no excitation is generated. Therefore, both $\psi\bar{\psi}$ and $\sigma\bar{\sigma}$ planons condense on the boundary.

3.6 Appendix A: controlled gate details

In this Appendix, we present the details of the graphical definition of G_p^s, its inverse, the commutation relations, and the proof for the central equation. See Appendix 2.9 for a condensed review of the string-net models.

Graphical definition

We perform the graphical calculation that leads to the last line in Eq. (3.6). We compute

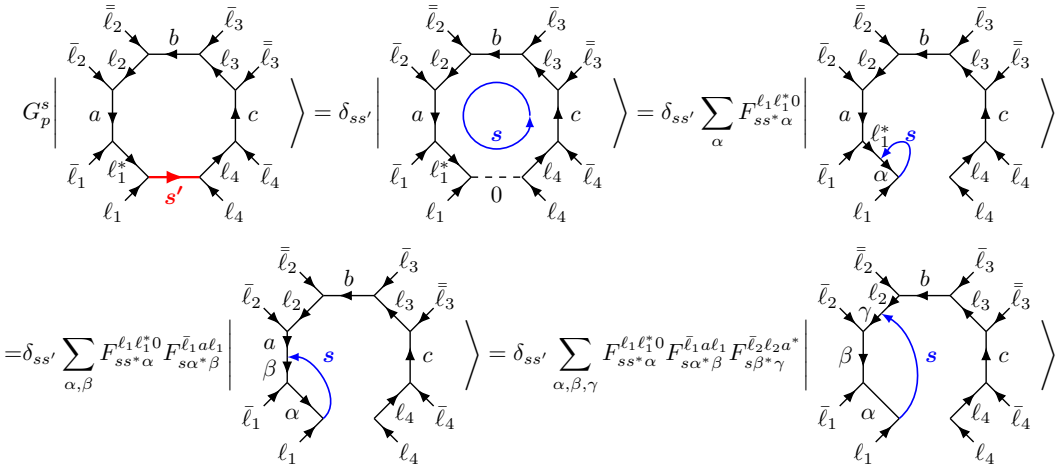

$= \cdots$ (repeat similar steps across the subsequent vertices around the plaquette)

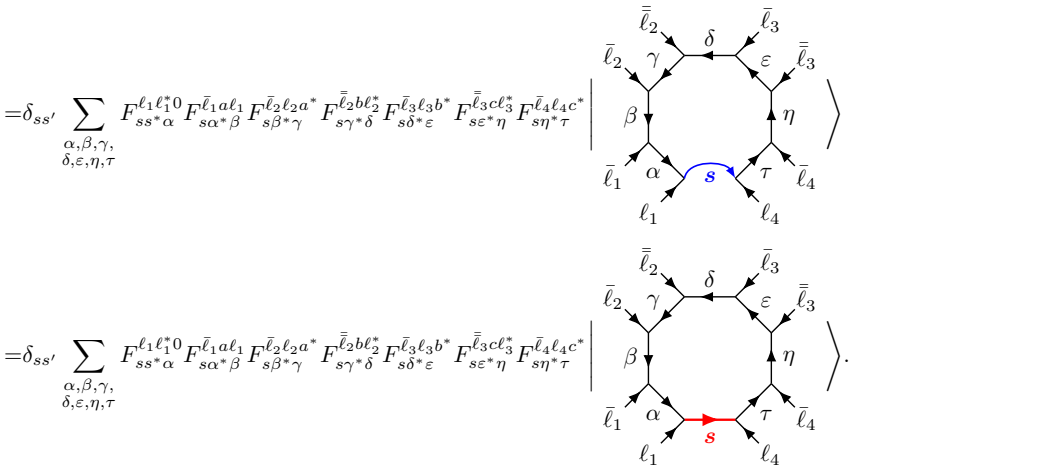

(3.22)

Isometric property

We now show that G_p^s is an isometry. That is, ${G_p^s}^\dagger G_p^s$ equals identity on the input space, which we called $\mathcal{V}_{p,s}^{\mathrm{SN}}$ in section 3.4.

Graphically, ${G_p^s}^\dagger$ removes a string of s from the edges of the plaquette when the controlled edge is in the state $|s\rangle$. Let us denote the matrix elements of G_p^s by

$$\begin{aligned}&[G_p^s]^{(s,\alpha,\beta,\gamma,\delta,\varepsilon,\eta,\tau)}_{(s',\ell_1^*,a,\ell_2,b,\ell_3,c,\ell_4)}(\ell_1,\bar{\ell}_1,\bar{\ell}_2,\bar{\bar{\ell}}_2,\bar{\ell}_3,\bar{\bar{\ell}}_3,\bar{\ell}_4,\ell_4)\\ &= \delta_{ss'} F^{\ell_1\ell_1^*0}_{ss^*\alpha} F^{\bar{\ell}_1 a\ell_1}_{s\alpha^*\beta} F^{\bar{\ell}_2\ell_2 a^*}_{s\beta^*\gamma} F^{\bar{\bar{\ell}}_2 b\ell_2^*}_{s\gamma^*\delta} F^{\bar{\ell}_3\ell_3 b^*}_{s\delta^*\varepsilon} F^{\bar{\bar{\ell}}_3 c\ell_3^*}_{s\varepsilon^*\eta} F^{\bar{\ell}_4\ell_4 c^*}_{s\eta^*\tau}\,.\end{aligned} \tag{3.23}$$

Then, $G_p^{s\,\dagger}$ has an algebraic expression of

$$G_p^{s\,\dagger}\Big|\;\raisebox{-0.5em}{ 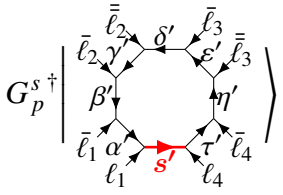 }\;\Big\rangle$$

$$= \sum_{\substack{t_1,t_2,t_3,\\ t_4,t_5}} \left([G_p^s]^{(s',\alpha',\beta',\gamma',\delta',\varepsilon',\eta',\tau')}_{(s,\ell_1^*,t_5,t_4,t_3,t_2,t_1,\ell_4)}(\ell_1,\bar{\ell}_1,...,\ell_4)\right)^* \times \tag{3.24}$$

$$\Big|\;\raisebox{-0.5em}{ 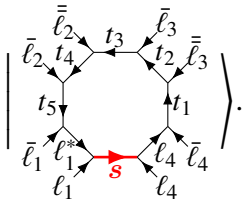 }\;\Big\rangle.$$

Using the orthogonality relation Eq. (2.46), we find

$$G_p^{s\dagger}G_p^s\Big|\;\raisebox{-0.5em}{ 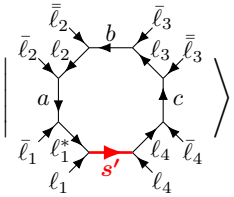 }\;\Big\rangle$$

$$= \delta_{ss'} \sum_{\substack{t_1,t_2,t_3,\\ t_4,t_5}} \delta_{t_1 c}\delta_{t_2\ell_3}\delta_{t_3 b}\delta_{t_4\ell_2}\delta_{t_5 a}\Big|\;\raisebox{-0.5em}{ 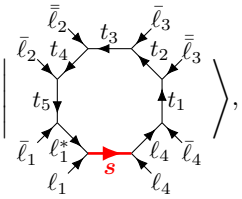 }\;\Big\rangle, \tag{3.25}$$

thereby establishing G_p^s as an isometry. Hence, $G_p = \sum_s G_p^s$ is also an isometry.

Commutation relations

The commutation relations of the G_p^s operators immediately follow from the graphical definition. Any two G_p^s and $G_{p'}^{s'}$ commute, provided that they do not act on each other's controlled edge. When p and p' are the same plaquette, G_p^s and $G_p^{s'}$ commute trivially, because they act on orthogonal spaces with the control edge in $|s\rangle$ and $|s'\rangle$ respectively. If the plaquettes p and p' are not next to each other, G_p^s and $G_{p'}^{s'}$ obviously commute. When p and p' are adjacent, the proof of commutation amounts to showing the order, in which the string s and s' are fused into the bordering edges, does not matter.

Consider G_p^s and $G_{p'}^{s'}$ acting on two adjacent plaquettes p and p'. We focus on the bordering edges of these two plaquettes. We will show that the F-symbols associated with the two diagrams (the thickened red arrows indicate the direction of motion of the s- and s'-strings),

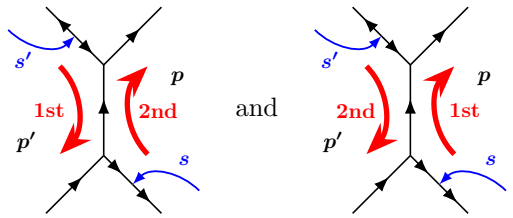

are equal. The left diagram corresponds to computing $G_p^s G_{p'}^{s'}$ on a reference ket-vector, and the right diagram corresponds to $G_{p'}^{s'} G_p^s$.

In the case where s' moves first, we find

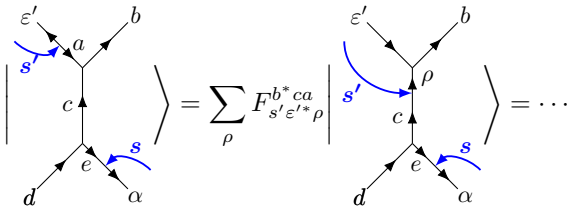

$$= \sum_q \left(\sum_\rho F^{b^* c a}_{s' \varepsilon'^* \rho} F^{e^* d c^*}_{s' \rho^* \tau'} F^{\tau' \rho^* e^*}_{s \alpha^* q^*} F^{\varepsilon'^* b^* \rho}_{s q \gamma} \right)$$

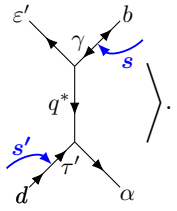

(3.26)

In the case where s moves first, we have

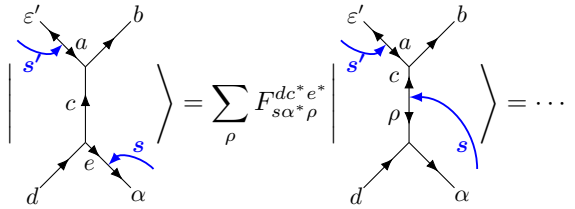

$$= \sum_q \left(\sum_\rho F^{dc^* e^*}_{s \alpha^* \rho} F^{ab^* c}_{s \rho^* \gamma} F^{\gamma \rho^* a}_{s' \varepsilon'^* q} F^{\alpha^* d \rho}_{s' q^* \tau'} \right)$$

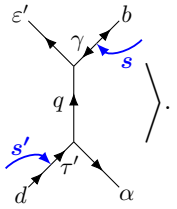

(3.27)

For each fixed q, we want to show that the coefficients, i.e. free sums over ρ, in Eq. (3.26) and Eq. (3.27) are equal. To do this, we consider an alternative way of

moving the strings s and s'. We will show that this alternative expression can be simplified, via the pentagon equation, to produce either Eq. (3.26) or Eq. (3.27). The alternative expression is obtained by moving both s and s' to the central edge,

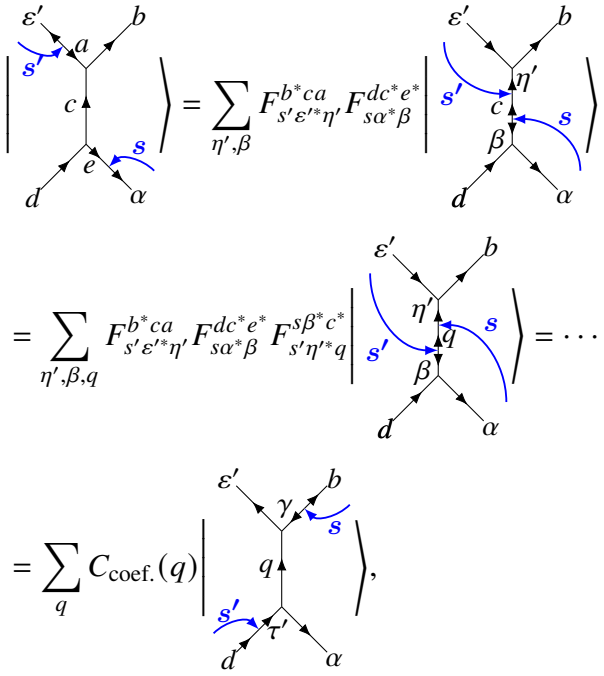

where, for each q, the coefficient of the alternative expression is

$$C_{\text{coef.}}(q) = \sum_{\eta',\beta} F^{b^*ca}_{s'\varepsilon'^*\eta'} F^{dc^*e^*}_{s\alpha^*\beta} F^{s\beta^*c^*}_{s'\eta'^*q} F^{\alpha^*d\beta}_{s'q^*\tau'} F^{\varepsilon'^*b^*\eta'}_{sq\gamma}. \tag{3.28}$$

Manipulating the F-symbols via the tetrahedral symmetry Eq. (2.44) and performing the above sum over either η' or β via the pentagon equation Eq. (2.45), we obtain

$$\begin{cases} \sum_{\rho} F^{b^*ca}_{s'\varepsilon'^*\rho} F^{e^*dc^*}_{s'\rho^*\tau'} F^{\tau'\rho^*e^*}_{s\alpha^*q^*} F^{\varepsilon'^*b^*\rho}_{sq\gamma} & \text{if sum over } \beta, \\ \sum_{\rho} F^{dc^*e^*}_{s\alpha^*\rho} F^{ab^*c}_{s\rho^*\gamma} F^{\gamma\rho^*a}_{s'\varepsilon'^*q} F^{\alpha^*d\rho}_{s'q^*\tau'} & \text{if sum over } \eta', \end{cases} \tag{3.29}$$

which are exactly the coefficients in Eq. (3.26) and Eq. (3.27) for fixed q. Hence, the order, in which the strings s and s' are fused into the bordering edges does not matter. That is, $[G^s_p, G^{s'}_{p'}] = 0$, as long as they do not act on each other's controlled edge. The proofs for the remaining commutation relations in Eq. (3.9) and Eq. (3.10) are similar.

The central equation

Let us prove the central equation on a triangular plaquette. The proof on any polygon-shaped plaquette is similar. With the graphical definitions, we find

$$G_p^{\gamma}\,(|\gamma\rangle\langle c|)_{\rm ct}\,G_p^{c\,\dagger}\Big|$$
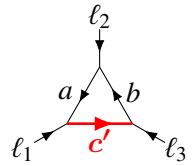

$$\Big\rangle$$

$$=G_p^{\gamma}\,(|\gamma\rangle\langle c|)_{\rm ct}\,\delta_{cc'}\sum_{t_1}F^{\ell_2 a^* b}_{c\ell_3 t_1^*}\Big|$$
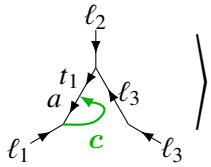

$$\Big\rangle$$

$$=G_p^{\gamma}\,(|\gamma\rangle\langle c|)_{\rm ct}\,\delta_{cc'}\sum_{t_1}F^{\ell_2 a^* b}_{c\ell_3 t_1^*}F^{\ell_1 c^* a}_{ct_1 0}\delta_{t_1\ell_1^*}\Big|$$
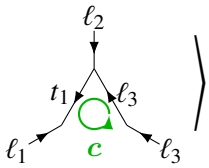

$$\Big\rangle$$

$$=\delta_{cc'}\left(F^{\ell_2 a^* b}_{c\ell_3\ell_1}F^{\ell_1 c^* a}_{c\ell_1^* 0}\right)\Big|$$
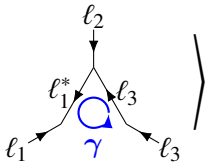

$$\Big\rangle$$

$$=\delta_{cc'}\left(F^{\ell_2 a^* b}_{c\ell_3\ell_1}F^{\ell_1 c^* a}_{c\ell_1^* 0}\right)\sum_{\alpha}F^{\ell_1^*\ell_1 0}_{\gamma^*\gamma\alpha^*}\Big|$$
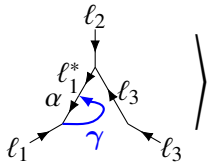

$$\Big\rangle$$

$$=\delta_{cc'}\sum_{\alpha,\beta}F^{\ell_2 a^* b}_{c\ell_3\ell_1}F^{\ell_1 c^* a}_{c\ell_1^* 0}F^{\ell_1^*\ell_1 0}_{\gamma^*\gamma\alpha^*}F^{\ell_2\ell_3\ell_1}_{\gamma\alpha^*\beta}\Big|$$
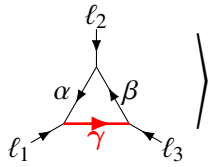

$$\Big\rangle, \tag{3.30}$$

Now, it remains to show that the coefficient for every basis ket-vector (i.e. fixing α and β) is the same as that of $\sum_k P^{\gamma}_{\rm ct}\left(\frac{d_k}{d_\gamma d_c}B_p^k\right)P^{c}_{\rm ct}$. To do this, first, let us write the pentagon equation Eq. (2.45) in a different form via the tetrahedral symmetry Eq. (2.44)

$$F^{ijp}_{kq^*r}F^{iq^*r}_{\ell^* sm}=\sum_n F^{rj^*k^*}_{n\ell s^*}F^{ipj}_{nsm}F^{q^*kp^*}_{nm^*\ell^*}\frac{d_n d_r}{\sqrt{d_k d_s d_j d_\ell}}. \tag{3.31}$$

Focusing on the F-symbols of Eq. (3.30), we find

$$\begin{aligned} & F^{\ell_2 a^* b}_{c\ell_3\ell_1} F^{\ell_1 c^* a}_{c\ell_1^* 0} F^{\ell_1^*\ell_1 0}_{\gamma^*\gamma\alpha^*} F^{\ell_2\ell_3\ell_1}_{\gamma\alpha^*\beta} \\ &\qquad = \sqrt{\frac{d_\alpha}{d_{\ell_1} d_\gamma}} \sqrt{\frac{d_a}{d_{\ell_1} d_c}} F^{\ell_2 a^* b}_{c\ell_3\ell_1} F^{\ell_2\ell_3\ell_1}_{\gamma\alpha^*\beta} \\ &\qquad = \sum_k \frac{d_k}{d_\gamma d_c} F^{\ell_1 a c^*}_{k\gamma^*\alpha} F^{\ell_2 b a^*}_{k\alpha^*\beta} F^{\ell_3 c b^*}_{k\beta^*\gamma}, \end{aligned} \tag{3.32}$$

The first equality follows from the normalization of F-symbols in Eq. (2.43), and we have used Eq. (3.31) in the second equality to get the last line. The last line is exactly the coefficient of $\sum_k P^\gamma_{\text{ct}} \left(\frac{d_k}{d_\gamma d_c} B^k_p\right) P^c_{\text{ct}}$ on the same ket-vector. Hence, we have proven the central equation on the triangular plaquette.

3.7 Appendix B: anyon condensation on a lattice

In this section, we briefly review the lattice realization of anyon condensation as discussed in Ref. [73, 99, 100]. Specifically, we review condensation of abelian bosonic anyons through two examples: condensation of $\psi\bar{\psi}$ in the doubled-Ising string-net and condensation of e or m in the toric code model. For a comprehensive review, we refer the reader to Ref. [87] and references therein.

Condensation of $\psi\bar{\psi}$ in doubled-Ising

After condensing the abelian boson $\psi\bar{\psi}$ in the doubled-Ising string-net, the resultant system has a topological order that is the same as the toric code.[89] For the lattice model, the condensation is achieved as follows [73, 99].

First, we couple the doubled-Ising Hamiltonian with the shortest open-ended string-operator of $\psi\bar{\psi}$. That is, we add the operator $W_l^{\psi\bar{\psi}}$ for every edge l as

$$H_{\text{D.I.}} - J \sum_l W_l^{\psi\bar{\psi}}, \tag{3.33}$$

where $H_{\text{D.I.}}$ is string-net Hamiltonian for the doubled-Ising theory, $J > 0$ is a real parameter controlling the strength of the coupling, and $W_l^{\psi\bar{\psi}} = (-1)^{n_1(l)}$ with $n_1(l) = 1$ if l is in the state $|1\rangle$ and $n_1(l) = 0$ otherwise (see Section 2.10 for a derivation). $W_l^{\psi\bar{\psi}}$ creates a pair of $\psi\bar{\psi}$ excitations, each at a plaquette bordering l (see Fig. 2.1).

Next, we energetically favor the creation of $\psi\bar{\psi}$ excitations by increasing J. The system is then driven across a phase transition. The ground state of the resultant phase is a condensate of $\psi\bar{\psi}$ excitations.

To see the $\psi\bar{\psi}$-condensed phase has the topological order of the toric code, let us take the $J \to +\infty$ limit. The coupling term $W_l^{\psi\bar{\psi}}$ imposes energy costs for every edge in the state $|1\rangle$. Taking the limit essentially removes every string-net configuration that contains a 1-string. Treating $H_{\text{D.I.}}$ as a perturbation, we find a commuting projector Hamiltonian

$$H = -\sum_v PQ_vP - \sum_p \frac{1}{2}\left(B_p^0 + B_p^2\right), \tag{3.34}$$

where $P = \prod_l \frac{1}{2}\left(\mathbb{I} + W_l^{\psi\bar{\psi}}\right)$ is the projector onto the Hilbert space of the condensed phase. This Hamiltonian is exactly that of the toric code [68].

Condensation of e or m in toric code

Condensing either the e or the m boson in the toric code model leads to the trivial phase without any topological order. On the lattice level, this is analyzed extensively in Ref. [100]. Here, we quickly review the results of Ref. [100].

Let us start by considering the condensation of the e excitations. The condensation can be induced by coupling the toric code Hamiltonian (see Eq. (3.2)) with $W_l^e = X_l$, the shortest open-ended string-operator of e. That is, we consider the Hamiltonian

$$H_{\text{T.C.}} - J\sum_l W_l^e. \tag{3.35}$$

To see the condensed phase has the trivial topological order, we again take the $J \to +\infty$ limit. We see that the ground state is a product state given by $\otimes_l |+\rangle_l$, where $|+\rangle = \frac{1}{\sqrt{2}}(|0\rangle + |1\rangle)$ is the $+1$ eigenstate of X. Hence, no topological order.

Similarly, for the condensation of m excitations, we consider the Hamiltonian

$$H_{\text{T.C.}} - J\sum_l W_l^m, \tag{3.36}$$

where $W_l^m = Z_l$. At the $J \to +\infty$ limit deep inside the condensed phase, we find the ground state is again a product state given by $\otimes_l |0\rangle_l$.

Chapter 4

CONSTRUCTION OF FRACTONS FROM GAUGING COMPOSITE SUBSYSTEM SYMMETRIES

In the generalized foliation scheme, a fracton model of different sizes are related via sub-dimensional sequential linear-depth circuits, or from the perspective of excitations, via condensation of planons, to reach a model of a smaller size, and "uncondensation" of them i.e. gauging, to reach a larger size. This naturally induces an equivalence relation for fracton orders: fracton models are in the same generalized foliated fracton order if they can be transformed into each other via a circuit, which is a finite-depth of sequential linear-depth circuits acting near sub-dimensional manifolds (recall Fig. 1.6), or via the equivalent planon condensation process. In this Chapter, we show that the Ising cage-net can be obtained by decorating the X-cube model with the Ising anyons via gauging composite subsystem symmetries, which has an equivalent picture as condensation of planons (Sec. 4.7). Therefore, the Ising cage-net and the X-cube model belong to the same generalized foliated fracton order. Moreover, we discover a new Type-I non-abelian fracton model whose fractons are non-abelian with quantum dimensions of $(\sqrt{2})^3$ (Sec. 4.5). We call this model the tri-Ising-fracton model.

4.1 Overview of gauging composite symmetry

In gauge theories of global symmetries, it is well understood that if we start with two independent global symmetries and condense the composite of the two gauge charges, their corresponding fluxes bind together to remain deconfined in the condensate. Consider, for example, two 2D planes, each with a global $\mathbb{Z}_2$ symmetry, as shown in Fig. 4.1. When the planes are coupled to $\mathbb{Z}_2$ gauge fields separately, they each have a $\mathbb{Z}_2$ gauge charge (e_1 and e_2) and a corresponding $\mathbb{Z}_2$ flux (m_1 and m_2). If, instead, only the composite global symmetry is gauged (the two planes are coupled to the same gauge field), the composite of the two symmetry charges e_1e_2 is no longer a symmetry charge. In the gauge theory, this corresponds to the condensation of the gauge charge pair. As a result, individual gauge fluxes become confined, while the flux pair remains deconfined, meaning that m_1, and m_2 always appear together. Such a mechanism is, of course, well understood and plays a vital role in, for example, coupled layer construction of 3D models such as the 3D toric

code and twisted gauge theories.

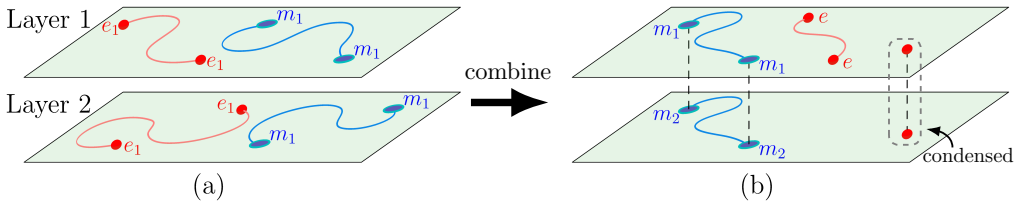

Figure 4.1: Gauging two planes with $\mathbb{Z}_2$ global symmetries. (a): gauging the two layers separately. We have two copies of the $\mathbb{Z}_2$ gauge theory with planon charges e_i and planon fluxes m_i. (b): gauging the combined symmetry of the two planes. The gauge fluxes m_1 and m_2 now bind together, becoming a new planon flux. Individual charge e_1 or e_2 remains deconfined planon excitations while the charge pair e_1e_2 is condensed.

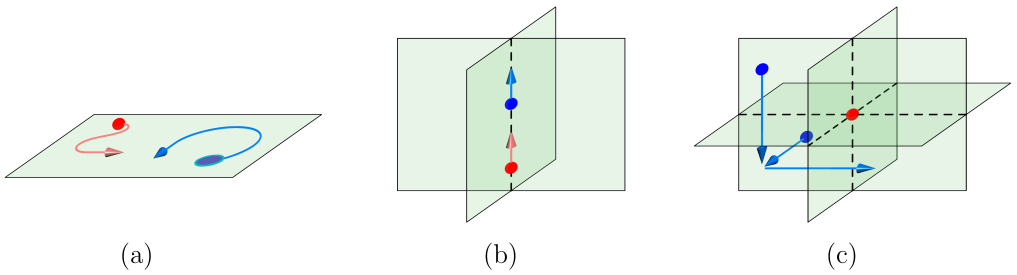

Figure 4.2: Gauging correspondence for planar subsystem symmetries. (a) planon charge (red, transforming under one planar symmetry) and the corresponding planon flux (blue); (b) lineon charge (transforming under two planar symmetries) and the corresponding lineon flux; (c) fracton charge (transforming under three planar symmetries) and the corresponding lineon fluxes.

What happens if we have subsystem symmetries instead of global 0-form symmetries? For simplicity, we will focus on planar symmetries in 3D systems in this paper. There are several possibilities. First, the symmetry charges can be planons, lineons, fractons, which are point excitations that move in 2D, 1D, and 0D submanifolds in the system. The planons, lineons, and fractons transform under one, two, and three sets of (intersecting) planar symmetries, respectively, as shown in Fig. 4.2. When the symmetries are gauged, the corresponding gauge flux of a planon charge is a planon in the same plane; the gauge flux of a lineon charge is a lineon along the same line; the gauge fluxes of a fracton charge are lineons in x, y, z directions that fuse into identity, as shown in Fig. 4.2. This set of correspondence was shown explicitly in Ref. [32]. When we combine the subsystem symmetries of different charges, there are several potential outcomes. One possibility is when we have charges of the same type, and all their overlapping planar symmetry generators are

respectively combined to give the new symmetries. For example, given two fracton charges, we can combine their planar symmetries in xy, yz, zx planes, respectively. If separately gauged, the two charges correspond to the same type of flux, and it is natural to expect that when such a combined symmetry is gauged, the two fluxes bind together to give the new flux with the same mobility. The second possibility is a composite symmetry combination, which happens when we have charges of potentially different types such that not all of their planar symmetry generators can or are one-to-one combined. For example, we may have a fracton charge with planar symmetry in xy, yz, and zx planes and a planon charge in the xy plane, and their xy planar symmetries are combined. If gauged separately, the fracton charge corresponds to lineon fluxes in x, y, and z directions, while the planar charge corresponds to planar flux in the xy plane. When the combined symmetry is gauged, what is the new flux like? Do the original x, y, z lineon, and xy planon fluxes bind into new lineon fluxes, planon fluxes, or fracton fluxes?

We address this problem in the following sections. We find that the way the original fluxes bind to give the new fluxes depends not only on the mobility of the original fluxes and the plane where symmetries are combined but also sensitively on how the symmetries are combined exactly. In particular, we are going to show in section 4.2, two examples, both of which start with one set of fracton charges and three sets of planon charges in xy, yz, zx planes, and the three sets of planar symmetries of the fracton charge are respectively combined with the planar symmetries of the planon charges. However, the way the original lineon fluxes and planon fluxes bind together to give the new fluxes are very different. In Model FP1, two original planon fluxes from intersecting planes attach to an original lineon flux along the intersection line to give a new lineon flux. In Model FP2, the lineon flux disappears, and the lineon dipole binds with an original planon flux to give a new planon flux. We obtain this result by solving the gauge theory lattice model. Can we arrive at the result without doing lattice level calculation? In section 4.3, we use the principle of "remote detectability": *For fractional (charge) excitations, there exist operators that detect their existence at a large distance; for non-fractional (charge) excitations, no operator can detect their existence at a large distance.* Applying this principle to the subsystem symmetry cases we are interested in, we can see directly why Models FP1 and FP2 work differently, as described above. This understanding is helpful because we can design models where subsystem symmetry fluxes are bound to planon fluxes in specific ways and acquire nontrivial statistics or non-abelian features through the process. We discuss in section 4.4, how lineon and fracton fluxes can be decorated in

this way, reproducing nontrivial fracton order like semionic X-cube, Ising cage-net, etc. In section 4.5, we construct new fracton models. We establish the connection between this gauging approach and the cage-net construction in section 4.6.

4.2 Fracton + planon: two examples Model FP1 and Model FP2

In this section, we present examples of 'gauging composite symmetry' and demonstrate the phenomenon of flux binding. We present two classes of models, Model FP1 and Model FP2. The construction of these models uses a fracton-charge system and stacks of planon-charge systems. The former is associated with $\mathbb{Z}_2$ fracton charges transforming under xy, yz, and zx planar symmetries, and the latter is associated with $\mathbb{Z}_2$ planon charges that transform under the planar symmetries of the layers in the stacks. We consider the stacks of planon-charge systems along three directions, i.e., the xy, yz, and zx planes. Thus, in both the fracton-charge and planon-charge systems, we have a planar symmetry associated with each lattice plane. We now consider a symmetry of the combined system generated by products of planar symmetries of the fracton-charge system and the planon-charge system. In particular, in each xy plane, the planar $\mathbb{Z}_2$ symmetry associated with the fracton charge is combined with the xy planar $\mathbb{Z}_2$ symmetry associated with the xy planons to yield a symmetry generator of the combined system. The symmetry generators in the yz and zx planes are defined similarly for the combined system. We refer to this symmetry of the combined system as the composite symmetry. This general description of the composite symmetry holds for both Model FP1 and Model FP2. However, as we will see below, the exact structures of the planar-charge system and the planar symmetry are different for Model FP1 and Model FP2. This leads to a difference in the gauge fluxes of Model FP1 and Model FP2.

For both examples, we start from the paramagnetic product state where all matter qubits are in the $|+\rangle = \frac{1}{\sqrt{2}}(|0\rangle + |1\rangle)$ state. Our goal is to study the exact solvable model obtained by gauging the composite symmetry [25, 32] and compare it to the models obtained by gauging the individual symmetries of the fracton-charge and planon-charge systems separately; in particular, we observe how the fluxes of the model obtained by gauging the composite symmetry are a composite of the fluxes of the decoupled gauged models. For instance, gauging the fracton-charge system alone gives a model with lineon fluxes, while gauging the planon-charge system alone gives planon fluxes. In Model FP1 obtained by gauging the composite symmetry, the lineon flux of the gauged fracton charge system binds with two planon fluxes of the gauged planon charge system to form a new lineon flux. In Model FP2

obtained by gauging the composite symmetry of a different nature, each lineon flux gets confined, but a lineon dipole binds with a planon flux to form a new planon flux.

Below, we first illustrate the procedure of gauging the composite symmetry with a simple example. In particular, we consider a 2D bilayer Ising paramagnet, such that two global planar symmetries of the two layers can be combined into a planar composite symmetry (see Fig. 4.1) and gauged. Following that, we discuss Model FP1 and Model FP2.

Warm-up: Bilayer Planon Model

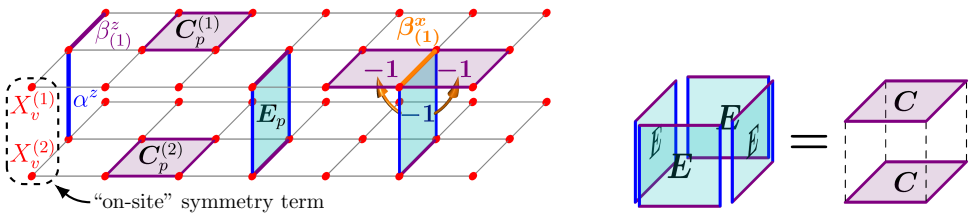

(a) (b)

Figure 4.3: Bilayer Planon model. (a): from left to right, the "on-site" symmetry term $X_v^{(1)} X_v^{(2)}$; the minimal coupling terms and the flux terms $\boldsymbol{C}^{(1)}$, $\boldsymbol{C}^{(2)}$ and $\boldsymbol{E}$. The $\boldsymbol{E}$-type flux term does not contribute to superselection sectors because its excitation can be converted into $\boldsymbol{C}$-type excitations on either the top or the bottom plane by the action of a Pauli-X operator, e.g. $\beta^x_{(1)}$. Hence, we can set $\boldsymbol{E}_p = \mathbb{I}$. (b): Consider the product of four $\boldsymbol{E}$ terms. The same product is equal to that of $\boldsymbol{C}_p^{(1)}$ and $\boldsymbol{C}_p^{(2)}$. Hence, these two $\boldsymbol{C}$ terms must be simultaneously excited since $\boldsymbol{E}_p = \mathbb{I}$. Notice that the $\boldsymbol{C}$ terms are exactly the original flux terms had we gauged the planes individually. Constructing the string operator, we find that the original fluxes must bind together to remain deconfined.

We consider a 2D bilayer Ising system, consisting of two layers of 2D Ising paramagnets, each with a $\mathbb{Z}_2$ on-site global symmetry $\prod_v X_v^{(1|2)}$ where 1 and 2 are the layer indices. On gauging the planar symmetry of each layer individually, the minimal couplings are intralayer 2-qubit terms, which we denote as β. The resulting pure gauge theory is just two decoupled copies of the 2D Toric Code, with the Hamiltonian,

$$H = -\sum_{\ell\in\{1,2\}} \sum_{p\in P_\ell} \boldsymbol{C}_p^{(\ell)} - (\text{charge terms}). \tag{4.1}$$

where ℓ is a layer index, P_ℓ denotes the plaquettes in each layer and $\boldsymbol{C}$ denote the 4-qubit flux terms of β gauge qubits around a plaquette; see Fig. 4.3(a). Here, we write only the flux terms in notation form, as our goal is to demonstrate flux binding.

We are now interested in gauging the composite symmetry $\prod_v X_v^{(1)} X_v^{(2)}$ of the bilayer system. For this composite symmetry, we again have the 2-qubit intralayer minimal couplings in each plane; we denote these as β. However, there is now an additional 2-body coupling that acts on one qubit on the bottom layer and one qubit on the top layer; we label these as α. For gauging, we add the corresponding β and α gauge qubits on the edges defining the minimal couplings. We get the aforementioned $\boldsymbol{C}$-flux terms from the β minimal couplings. Due to the additional minimal coupling, a new flux term arises, a 4-qubit term acting on two α gauge qubits and two β gauge qubits; we dub these the $\boldsymbol{E}$-flux terms.

We integrate out the original matter qubits, i.e., by setting their states to $|+\rangle$ in this case, to obtain a pure gauge theory. This pure gauge theory has one vertex term per matter spin and two kinds of flux terms $\boldsymbol{C}$ and $\boldsymbol{E}$, see (a) of Fig. 4.3. The Hamiltonian is given by

$$H = -\sum_{\ell\in\{1,2\}} \sum_{p\in P_\ell} \boldsymbol{C}_p^{(\ell)} - \sum_{p'} \boldsymbol{E}_{p'} - (\text{charge terms}), \tag{4.2}$$

where P_ℓ stands for the planes and p' denotes plaquettes connecting the two layers. As mentioned, the $\boldsymbol{C}$-type flux terms are also the flux terms obtained from gauging the individual symmetries of the layers. In contrast, the $\boldsymbol{E}$ flux terms are purely due to the gauging of the composite symmetry[1].

We now observe that the flux in the model given by Eq. 4.1 is a composite of the original fluxes. We see this through a relation between the original fluxes and new fluxes. We consider an excitation of a single $\boldsymbol{E}_p$ flux; by applying a Pauli X operator, we can convert this single $\boldsymbol{E}_p$ excitation to either a pair of $\boldsymbol{C}_p^{(1)}$ or a pair of $\boldsymbol{C}_p^{(2)}$ excitations (see Fig. 4.3(a)). Hence, the $\boldsymbol{E}$ terms do not contribute to the superselection sectors. In other words, this equivalence allows us to set the $\boldsymbol{E}$-type fluxes equal to the identity ($\boldsymbol{E}_p = \mathbb{I}$), so the new $\boldsymbol{E}$-type fluxes give rise to a relation between the $\boldsymbol{C}$-type fluxes: the product of a pair of $\boldsymbol{C}$-type fluxes with one flux in each plane is equivalent to a product of four $\boldsymbol{E}$-type fluxes around the side faces of a cube; see Fig. 4.3(b). If $\boldsymbol{E}_p = \mathbb{I}$, the two $\boldsymbol{C}$-type flux terms must be simultaneously excited, as the product of the two $\boldsymbol{C}$ fluxes must have eigenvalue +1. In this sense,

[1] In our examples, we'll use a choice of gauge fields that also produces the original flux terms; this is a particular choice that is of interest to us because we want to see the relation between the new and original fluxes from the decoupled theories. One could gauge the composite symmetry differently so the original fluxes no longer appear.

the two C planon fluxes bind together to give the planon flux of the model with gauged composite symmetry[2].

Fracton+Planon: Model FP1

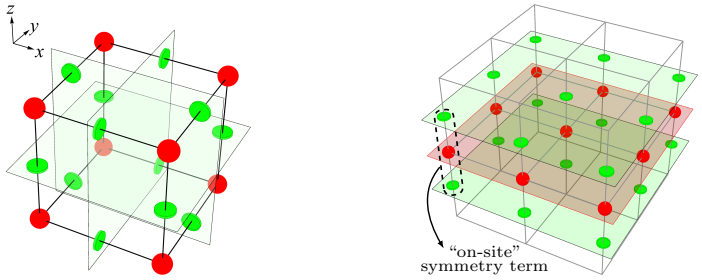

(a) (b)

Figure 4.4: Model FP1. (a): lattice setup. We consider a 3D Ising paramagnet with planar subsystem symmetries on a cubic lattice with the qubits living on the vertices (red spheres). For the stacks of the 2D Ising paramagnet systems (indicated by the planes) with 2D global symmetry, we place the qubits (green disks) at the centers of the edges. (b): the sandwiched structure of the composite symmetry in Eq. (4.3).

We now introduce our first nontrivial example. As mentioned above, the model is built by combining a fracton-charge system and planon-charge systems and gauging a symmetry of the integrated system generated by composite planar symmetries. Below we show that the gauge theory obtained from gauging the composite symmetry has a lineon flux composed of planon and lineon fluxes from the decoupled gauge theories.

We consider a cubic lattice where the matter qubits of a classical Ising model live on the vertices as shown in (a) of Fig. 4.4. We call this the fracton-charge system due to the symmetries we consider for this model. The fracton-charge system has planar subsystem symmetries given by $\prod_{v\in P^\mu_{i_\mu}} X_v$ for every plane $P^\mu_{i_\mu}$ with $\mu \in \{x, y, z\}$ and i_μ being the position index of the plane. We then insert three stacks of Ising paramagnets (planon-charge systems) such that their qubits are located on the edges. Each planon-charge system has a 2D global symmetry given by $\prod_{\rho\in P^\mu_{(i_\mu,i_\mu+1)}} X_\rho$ where $(i_\mu, i_\mu + 1)$ indicates the edges on which the qubits of the planon-charge systems live. We gauge the composite subsystem symmetry whose generators as shown in Fig. 4.4 (b) are given by

$$\mathcal{S}^\mu_{i_\mu} = \prod_{\rho\in P^\mu_{(i_\mu,i_\mu+1)}} \prod_{v\in P^\mu_{i_\mu}} \prod_{\rho'\in P^\mu_{(i_\mu-1,i_\mu)}} X_\rho X_v X_{\rho'}. \tag{4.3}$$

[2]This binding can be verified by explicitly writing the string operators for the fluxes.

Recall each symmetry generator is a “sandwich" involving 2 planon-charge symmetry generators and 1 fracton-charge symmetry generator. Hence taking the product of all symmetry generators orthogonal to a given axis should leave only the product of all fracton symmetry generators orthogonal to that axis. Hence we notice a relation among the symmetry generators of this model.

$$\prod_{i_x} \mathcal{S}^x_{i_y} = \prod_{i_y} \mathcal{S}^x_{i_y} = \prod_{i_z} \mathcal{S}^x_{i_z} \tag{4.4}$$

We note that this composite symmetry group for Model FP1 is isomorphic to the symmetry group of the undecorated plaquette Ising model.

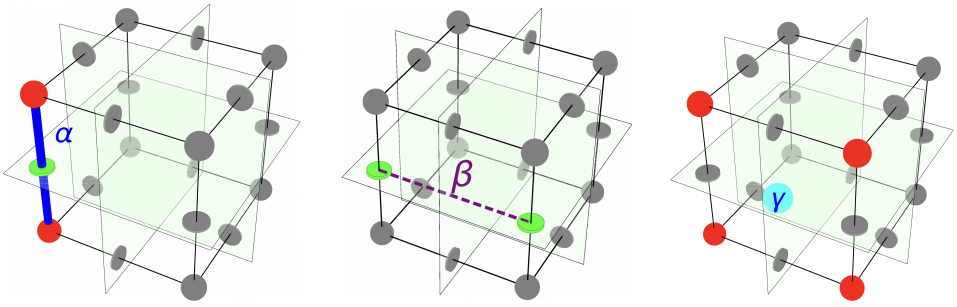

(a) (b) (c)

Figure 4.5: Model FP1: the minimal coupling terms. (a): A 3-qubit minimal coupling term of $\mathcal{S}^\mu_{i_\mu}$. We add a $\mathbb{Z}_2$ gauge qubit to the edge connecting the three matter qubits; we label this gauge qubit as α corresponding to the α-coupling. The charges associated with the α-coupling are the ‘composite condensate’ of this model. It requires a planon charge to fuse with a fracton dipole into the topological vacuum. (b): A 2-qubit minimal coupling term of $\mathcal{S}^\mu_{i_\mu}$. The β gauge qubit lives on the edge shown by the dashed line. Apart from a directional label, β has a plane label in the square brackets. We suppress the position index of the plane. The β’s are also the original minimal coupling terms for the planon-charge systems. (c): A 4-qubit minimal coupling term of the fracton-charge system. γ, however, is not a minimal coupling term for $\mathcal{S}^\mu_{i_\mu}$.

We consider three types of coupling terms associated with $\mathcal{S}^\mu_{i_\mu}$. There are the 3-qubit coupling terms (red and green qubits shown in Fig. 4.5(a)), which we label as α. There are the 2-qubit coupling terms (green qubits shown in Fig. 4.5(b)), which we label as β. Lastly, there are the 4-qubit coupling terms (red qubits shown in Fig. 4.5(c)), which we label as γ. Even though the γ couplings are generated by the α and β coupling terms, we consider them in our gauging process since we are interested in demonstrating how the fluxes from decoupled gauged models bind together and form fluxes for the model obtained by gauging the composite symmetry.

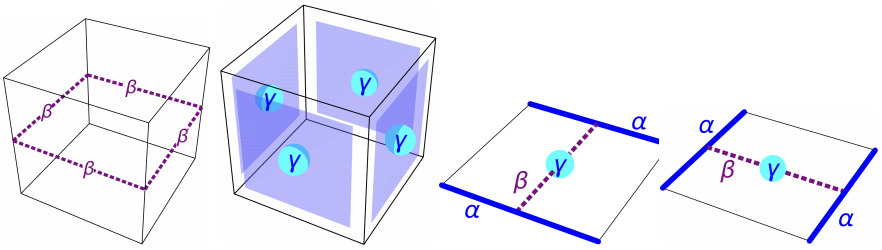

(a) (b) (c) (d)

Figure 4.6: Model FP1: The three types of flux terms: $\boldsymbol{C}_p^\mu$, $\boldsymbol{\Gamma}_p^\mu$, and $\boldsymbol{E}_p^{[\mu](\nu)}$. (a) & (b): A $\boldsymbol{C}_p^z$ flux term and a $\boldsymbol{\Gamma}_p^z$ flux term. They are those of the 2D planon-charge and the 3D fracton-charge systems respectively. (c) & (d): there are two kinds of $\boldsymbol{E}$-type flux terms on the face of a cube of the cubic lattice. Drawn here are (c) $\boldsymbol{E}_p^{[z](y)}$ and (d) $\boldsymbol{E}_p^{[z](x)}$ on the same face p.

To gauge the composite symmetry, we add a gauge qubit for each type of coupling term [25, 32] as shown in Fig. 4.5. We label the gauge qubits as α, β, and γ corresponding to the minimal couplings they are associated with. Following the gauging procedure, we obtain the Hamiltonian for Model FP1 as [3],

$$H^{FP1} = -\sum_{\mu,\{i_\mu\}} \left(\sum_{p\in P^\mu_{i_\mu}} \boldsymbol{\Gamma}_p^\mu + \sum_{p\in P^\mu_{(i_\mu,i_\mu+1)}} \boldsymbol{C}_p^\mu + \sum_{\nu,p\in P^\mu_{i_\mu}} \boldsymbol{E}_p^{[\mu](\nu)} \right) - (\text{charge terms}). \quad (4.6)$$

Here, the $\boldsymbol{C}$-type flux terms are the original fluxes of the planon-charge systems, and the $\boldsymbol{\Gamma}$-type flux terms are the original flux terms of the fracton-charge system. The $\boldsymbol{E}$-type flux terms are the new flux terms that arise in the model obtained from gauging composite symmetries. Similar to the bilayer model, we observe that the $\boldsymbol{E}$ terms do not contribute to the superselection sectors. For an excitation of the $\boldsymbol{E}$-type flux term i.e., $\boldsymbol{E}_p^{[\mu](\nu)} = -1$, we can act a Pauli X operator to turn it into two $\boldsymbol{C}$-type fluxes with the two corresponding $\boldsymbol{C}$ terms having the eigenvalue of -1. Hence, we can set all $\boldsymbol{E}_p^{[\mu](\nu)} = \mathbb{I}$. This gives a relation between the $\boldsymbol{\Gamma}$ and the $\boldsymbol{C}$ terms. The product of four $\boldsymbol{E}$ terms around the side faces of a cube must be identity, but the product is also equal to the product of a $\boldsymbol{\Gamma}$ and a $\boldsymbol{C}$ flux terms; see Fig. 4.7.

[3] As mentioned earlier in footnote 1, this is a particular choice of gauging of interest to us. We can make a different choice of gauging such that the fluxes of the gauged Hamiltonian H^A come from only the α and β couplings as

$$H^A = -\sum_{\mu,\{i_\mu\}} \left(\sum_{p\in P^\mu_{(i_\mu,i_\mu+1)}} \boldsymbol{C}_p^\mu + \sum_{p\in P^\mu_{i_\mu}} \boldsymbol{B}_p^\mu \right) - (\alpha,\beta \text{ charge terms}), \quad (4.5)$$

where $\boldsymbol{B}_p^\mu = \boldsymbol{E}_p^{[\mu](\nu)} \times \boldsymbol{E}_p^{[\mu](\rho)}$ is the product of two $\boldsymbol{E}$ terms on the same plaquette p.

The lineon string operator that satisfies this set of relations and the trivial $\boldsymbol{E}$-flux condition is described in Fig. 4.7. We observe that the string operator is the product of a lineon flux string operator from the fracton-charge system, together with two planon flux string operators from two intersecting planon-charge systems. Thus, we conclude that the new lineon flux is the composite of a lineon flux and two planon fluxes from the decoupled models, respectively.

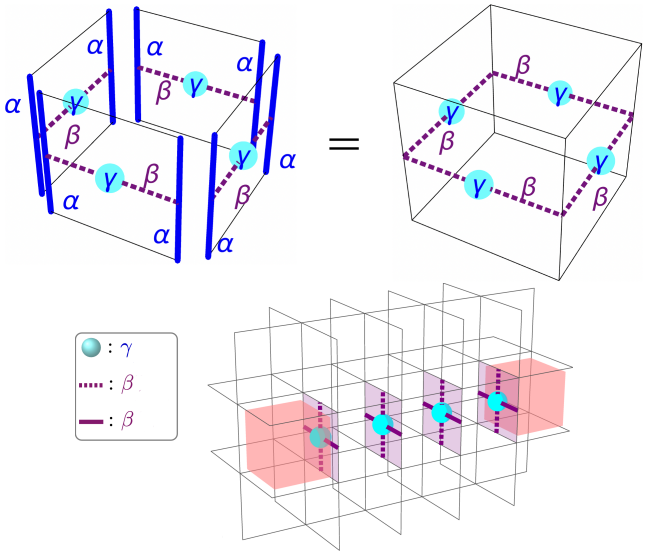

Figure 4.7: Model FP1: one of the relations between the original flux terms. The remaining relations can be obtained by rotations. LHS: the relation is the product of the four $\boldsymbol{E}$-type flux terms as shown, two $\boldsymbol{E}_p^{[y](x)}$'s and two $\boldsymbol{E}_p^{[x](y)}$'s. RHS: the $\boldsymbol{C}$-type and $\boldsymbol{\Gamma}$-type flux terms also have a relation. Right: Model FP1: the new lineon string operator for a y-mobile lineon. The locations of the new lineon excitations are indicated by the pink cubes. From this string operator, we see clearly that the new lineon is a composite of the original lineon flux together with two original planon fluxes from perpendicular planes.

Fracton+Planon: Model FP2

We present another nontrivial example of a model obtained from gauging composite symmetry. The underlying models consist of the same fracton-charge systems and the planon-charge systems as considered for Model FP1. However, the planon-charge systems are laid out such that the matter qubits live on the vertices; thus the nature of the composite symmetry is different. Below we show that the gauge theory obtained from gauging the composite symmetry has only planon fluxes; each is a composite of a planon flux and a lineon dipole flux from the decoupled gauged theories.

Similar to Model FP1, we have the fracton-charge system with matter qubits on the

vertices. We insert the three stacks of planon-charge systems into the cubic lattice, as shown in Fig. 4.8(a). The plaquettes of the planon-charge systems (not drawn) coincide with those of the cubic lattice. Each vertex hosts four matter qubits, one (the red sphere) from the fracton-charge system and three (the green disks) from three mutually intersecting planon-charge systems. We gauge the composite symmetry whose generators are given by

$$\mathcal{S}^{\mu}_{i_\mu} = \prod_{v \in P^{\mu}_{i_\mu}} X_{v,f} X_{v,\mu}, \tag{4.7}$$

where f denotes the matter qubit belonging to the fracton-charge system and μ denotes the matter qubit belonging to the planon charge system in the plane with direction i_μ. We note that the composite symmetry group of Model FP2 is isomorphic to that of 3 decoupled stacks of planon symmetry generators with no global relation.

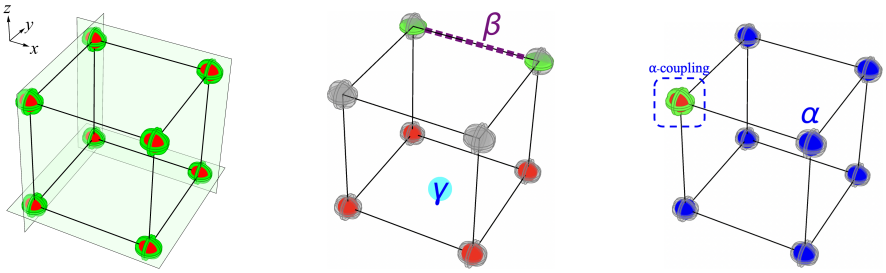

(a) (b) (c)

Figure 4.8: Model FP2. (a): lattice setup. Same as in Model FP1, we place the matter qubits of the fracton-charge system on the vertices. The stacks of planon-charge systems are arranged such that their qubits also live on the vertices. The plaquettes of the planon-charge systems coincide with those of the cubic lattice. (b): the original minimal coupling terms. The 2-qubit β-coupling terms are also minimal coupling for the composite symmetry Eq. (4.7). (c): the new minimal coupling term as a result of gauging the composite symmetry.

The couplings associated with the composite symmetry are the 2-qubit β-coupling terms, the 4-qubit γ-coupling terms, and the 2-qubit α-coupling terms as shown in Fig. 4.8. We add gauge qubits for each coupling term. Following the gauging procedure, we obtain the Hamiltonian for Model FP2 as

$$H^{FP2} = -\sum_{\mu,\{i_\mu\}} \left(\sum_{p \in P^{\mu}_{i_\mu}} \boldsymbol{\Gamma}^{\mu}_{p} + \sum_{p \in P^{\mu}_{i_\mu}} \boldsymbol{C}^{\mu}_{p} + \sum_{v, p \in P^{\mu}_{i_\mu}} \boldsymbol{E}^{[\mu](v)}_{p} \right) - (\text{charge terms}). \tag{4.8}$$

The fluxes consist of the original flux terms of the decoupled models, i.e., the $\boldsymbol{C}$-type and $\boldsymbol{\Gamma}$-type flux terms similar to Model FP1. But we also have the new $\boldsymbol{E}$-type

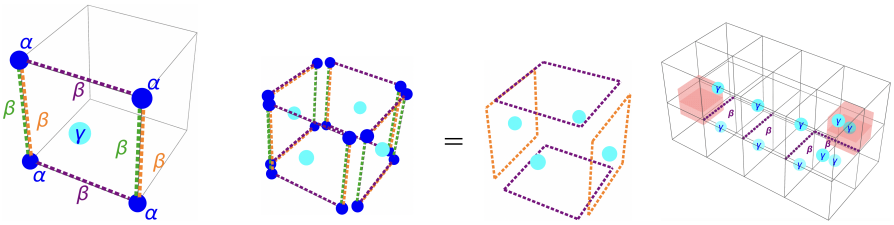

Figure 4.9: Model FP2. (a): One of the $\boldsymbol{E}$-type flux terms ($\boldsymbol{E}_p$). The other $\boldsymbol{E}$-type flux terms are plaquettes of the same form in the other 2 spatial planes. (b): One of the relations between the original flux terms. The remaining relations can be obtained by rotations. LHS: the relation is the product of the four $\boldsymbol{E}$-type flux terms as shown, two $\boldsymbol{E}_p^{[y](x)}$'s and two $\boldsymbol{E}_p^{[x](y)}$'s. RHS: the $\boldsymbol{C}$-type and $\boldsymbol{\Gamma}$-type flux terms also have a relation. (c): The new planon string operator for a z-plane mobile planon. We indicate the locations of the new planon excitations by the pink cubes. Notice that this string operator is exactly the product of an original z-plane planon flux string operator and an original z-plane lineon dipole flux string operator.

flux terms, Fig. 4.9, that arise from gauging the composite symmetry. Similar to the bilayer Model and Model FP1, we observe that the $\boldsymbol{E}$ terms do not contribute to the superselection sectors. In fact, on setting $\boldsymbol{E}_p^{[\mu]}$ to Identity, we get a relation between the $\boldsymbol{C}$ and the $\boldsymbol{\Gamma}$ flux terms. The corresponding gauge flux is a planon composed of a planon flux from the planon-charge system and a lineon dipole flux from the fracton-charge system; see the string operator for this combined gauge flux in Fig. 4.9.

We note that Model FP2 is equivalent to stacks of 2D toric codes. To see this, we recall that the gauge charges in Model FP2 consist of one fracton and three planons (in the xy, yz, zx directions). We write this charge basis as $\{f, p_{xy}, p_{yz}, p_{zx}\}$. The new minimal coupling (see Fig. 4.8(c)) corresponding to the composite symmetry is a product of the four elements of the charge basis. Hence $f \times p_{xy} \times p_{yz} \times p_{zx} = 1$, which implies that $p_{xy} \times p_{yz} \times p_{zx} = f$. This suggests that the charge basis is not independent, as the planon charges ($\{p_{xy}, p_{yz}, p_{zx}\}$) generate the fracton charge (f). Thus, we can choose an independent charge basis consisting of only planons ($\{p_{xy}, p_{yz}, p_{zx}\}$). For each basis planon, we can apply an entanglement renormalization circuit to extract a toric code layer [101, 102], leading to the result that Model FP2 is just a stack of 2D toric codes. Thus, we see that different patterns of flux binding, due to gauging different composite symmetries, result in different topological orders.

4.3 Flux binding via Remote Detectability

In the previous section, we saw through exactly solvable stabilizer models how the lineon fluxes of a fracton charge bind with the planon fluxes of planon charges when some composite planar symmetries of the fracton and planon charges are gauged. In this section, we arrive at the same result without solving the lattice models. In particular, we will use the principle of "remote detectability" to deduce how the old fluxes bind together to form new fluxes. This argument does not rely on the Model FP2 being a stabilizer or even exactly solvable and can be applied generally. We will apply the resulting insight to reproduce some interesting fracton models and construct new ones with nontrivial features in the next section.

The principle of "remote detectability" says: *fractional excitations can be detected with some 'remote' unitary operators which act only at a large distance from the excitation; non-fractional excitations, on the other hand, cannot be detected remotely*.

We apply this principle to fractional charge excitations in a gauge theory and deduce the corresponding form of the gauge flux[4]. In particular, knowing the form of the gauge charge, we can deduce the form of the remote detection operator. Truncating the remote detection operator then exposes the shape and mobility of the gauge flux excitation. We illustrate this line of argument using models with 2D global symmetry and 3D planar subsystem symmetries. Moreover, if we start with two independent systems but only keep some of their composite symmetries, certain local composites of the symmetry charges will no longer carry nontrivial charges. When the composite symmetries are gauged, remote detection operators that detect such local composites no longer give rise to deconfined flux excitations once truncated. We will see how this mechanism leads to the binding of individual fluxes when composite symmetries are gauged.

Flux excitations from truncating remote detection operators

Consider first a 2D system with global $\mathbb{Z}_2$ symmetry. A single charged particle carries a nontrivial symmetry charge while a charge pair does not. After coupling to the gauge field, the remote defection operator, therefore, should be able to detect a single charge but not a pair. This can be achieved, of course, with a loop integration of an electric field that intersects and anti-commutes with the Wilson line connecting to the single charge when it is created, as shown in Fig. 4.10(c). When the loop-

[4] Although remote detection operators do not necessarily act as pure $U(1)$ phases (in the case of non-abelian anyons with degeneracies), in this paper we only consider systems in which remote detection operators act as $U(1)$ phases on the excited states.

shaped remote detection operator is truncated, it leaves two endpoints (Fig. 4.10(d)), which correspond to a pair of point flux excitations that can move along the loop operator that twists and turns freely on the 2D plane. The flux excitations are hence planons.

In a 3D model with planar $\mathbb{Z}_2$ symmetry in each xy, yz, and zx plane and one charge at each triple intersection point of three perpendicular planes, local symmetric processes create a minimum of four charges at a time (Fig. 4.11 (a)). The remote detection operator should be able to detect not only single charges but also charge pairs remotely. This is achieved with the wireframe operator in Fig. 4.11 (b). When the wireframe encloses a single charge, it intersects and anti-commutes with the Wilson 'membrane' that extends from the single charge and detects its existence. The same configuration can be used to detect charge pairs. For example, to detect the vertical pair of charges on the left in Fig. 4.11 (c), we can use a wireframe operator such that half of the charge pair is 'inside' the wireframe while the other half is outside. Although the two charges in the pair can be very close to each other, this is still a 'remote' detection method because the wireframe operator only acts along the edges of the cube area it encloses and never gets close to either of the charges. Truncating the wireframe operator exposes point flux excitations that move along rigid wireframe edge directions (Fig. 4.10(d)). The flux excitations are hence lineons, and lineons in the x, y, and z directions fuse into the vacuum.

To determine the principle of truncation of remote detection (RD) operators, we find and slice the RD operators of a 2D model with global symmetry and a 3D system with planar symmetry and fracton charge (the ingredient models in our construction of sample models with a gauged composite symmetry). We first consider the 2D system, whose remote detection operator is a loop consisting of products of charge operators shown in Fig. 4.10(a). To determine the exact product of charge operators needed to create the RD loop, we refer to Fig. 4.10(b). The operator depicted in this figure detects charge excitations within the bulk in the ungauged theory; if there is an odd number of violations (eigenvalue -1) within this membrane of Pauli X operators, the operator is measured to be -1 (hence it can detect violations). Thus adding the gauge fields associated with each qubit in Fig. 4.10(b) should give the gauged RD operator (see Fig. 4.10(c)). An equivalent method of determining the particular form of the RD operator is to note what product of charge operators annihilates all gauge fields in the bulk and leaves gauge fields only at the region's boundary over which the product of terms is taken. Using this, one can see that a product of charge

terms in a closed loop satisfies this exact condition; hence the charge RD operator for a 2D system with global symmetry is a loop operator. This loop RD operator can detect individual anyon charges within the loop by anti-commuting with the excitation creation operator (see Fig. 4.10(d)). Truncating this loop RD operator (see Fig. 4.10(e)) reveals a single anyon (violation of Z plaquette stabilizer) at each endpoint; we conclude that the flux excitations of the 2D system are anyons. The same analysis can be done for a general 3D model with planar symmetry and a fracton charge.

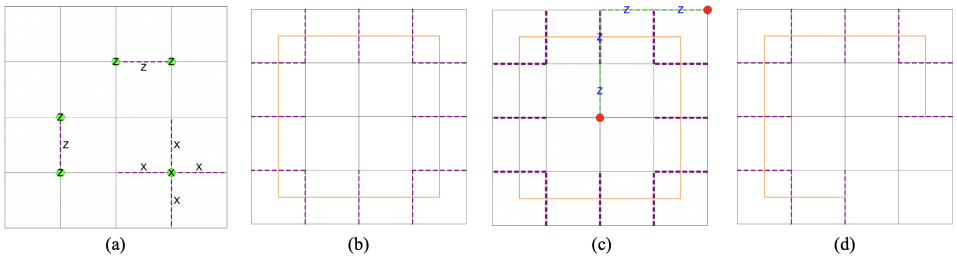

Figure 4.10: 2D model with global symmetry. (a): Minimal couplings and gauge symmetry operator. Qubits (green disks) live on vertices, and gauge fields (purple edges) are assigned to edges. (b): Operator that detects charges within the bulk (in the ungauged theory). (c): Remote detection operator capable of detecting excitations within the loop (shown in orange). This RD operator is formed by taking products of gauge symmetry operators such that the gauge fields in the bulk cancel out. (d): Loop RD operator detecting anyon charge via anticommutation between the loop and string creation operator. (e): Truncated remote detection operator. The excitations at the boundary of the truncation possess the same mobility as flux excitations.

Looking at the 3D model, the charge terms are given by cube operators (violations of which are fractons) shown in Fig. 4.11(a). Similar to the 2D model, we can see that in the ungauged theory, to detect a single violation of a Pauli X operator inside a finite volume, we take the product of Pauli X's at the body centers within the cubic volume (see Fig. 4.11(b)). Adding in the gauge fields according to the cubic charge operator, we see that the gauged RD operator is a cubic wireframe with gauge fields along the edges (see Fig. 4.11(c)). This wireframe detects fracton charges by anti-commuting with the membrane creation operator (see Fig. 4.11(d)). Truncating this RD operator (see Fig. 4.11(e)) shows that the excitations at the endpoints of the wireframe are lineons, i.e., the violations of the Z vertex terms of the 3D system. Additionally, note that since the endpoints of the truncated RD operator are lineons, RD operators can also be viewed as operators that move the flux excitations in a closed path far from the charge.

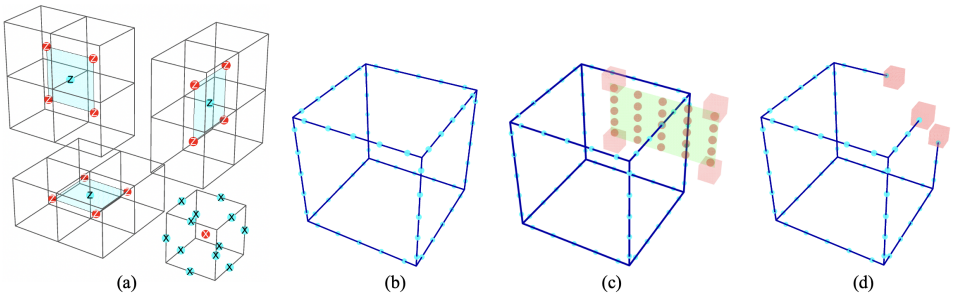

Figure 4.11: 3D model with planar symmetries and fracton charge. (a): Minimal couplings and gauge symmetry operator. Qubits (red spheres) live at body centers, and gauge fields (cyan spheres) are assigned to edges. (b): Operator that detects charges within the bulk (in the ungauged theory). (c): Remote detection operator capable of detecting excitations within the wireframe (shown in blue). This RD operator is formed by taking products of gauge symmetry operators such that the gauge fields in the bulk cancel out. (d): Wireframe RD operator detecting fracton charge via anticommutation between wireframe and membrane creation operator. This operator detects a fracton dipole in 2 steps: it first detects one fracton and then is moved to detect the second fracton in the dipole. (e): Truncated remote detection operator. The excitations at the boundary of the truncation possess the same mobility as flux excitations.

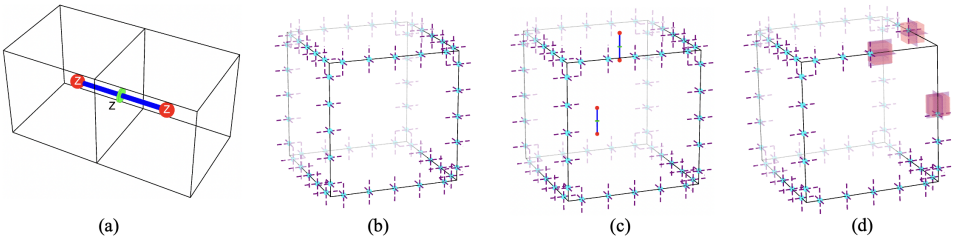

Figure 4.12: Model FP1. (a): The new 3-body minimal coupling due to gauging the composite symmetry. (b): Remote detection operator capable of detecting excitations within the decorated wireframe (shown in black). This RD operator is formed by taking gauge symmetry operators' products such that the bulk gauge fields cancel out. (c): The RD operator cannot detect the new minimal coupling; hence it is not a fractional excitation. (d): Truncated remote detection operator. The excitations at the boundary of the truncation possess the same mobility as flux excitations.

Remote detection in Model FP1

Now we will use the remote detection principle to see how the fluxes bind in Model FP1. Recall that in Model FP1, we had fracton charges at lattice sites of a cube lattice and planon charges on three sets of planes cutting through edges of the cube lattices. If the fracton-charge system is gauged alone, the remote detection operators are in the shape of a wire-frame, and correspondingly, the flux excitations are lineons, as

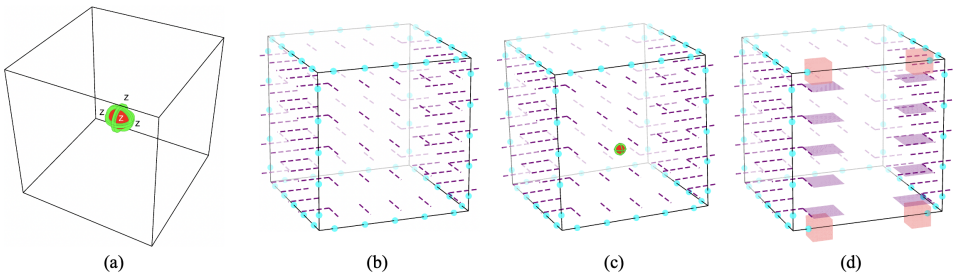

Figure 4.13: Model FP2. (a): The new 3-body minimal coupling due to gauging the composite symmetry. (b): Remote detection operator capable of detecting excitations within the decorated wireframe (shown in black). This RD operator is formed by taking gauge symmetry operators' products such that the bulk gauge fields cancel out. (c): The RD operator cannot detect the new minimal coupling; hence it is not a fractional excitation. (d): Truncated remote detection operator. The excitations at the boundary of the truncation possess the same mobility as flux excitations.

discussed above. If the planon-charge system is gauged alone, the remote detection operators are loops, and correspondingly the flux excitations are planons. If some composite symmetry is gauged, the lineon and planon fluxes must bind together. In particular, according to how the planar symmetries are combined in Model FP1, there is a new type of minimal coupling term containing both the fracton and the planon charges as shown in Fig. 4.12 (a). The wire-frame and loop remote detection operator would each detect the existence of such a term so we need to combine them in a way that this three-body term is not detected by any remote detection operator as it corresponds to a trivial superselection sector. This can be achieved with a remote detection operator, as shown in Fig. 4.12(b), where the loop operators are attached to the six surfaces of the wire-frame operator.

The new operator still takes the shape of a wire-frame. We can check that 1. individual fracton charges and fracton dipoles can still be detected if properly placed inside the decorated wire-frame operator; 2. individual planon charges can still be detected if placed on the surface of the decorated wire-frame operator; 3. the new three-body minimal coupling cannot be detected by any of the decorated wire-frame operators, whether the minimal coupling is entirely inside the operator or partially outside as shown in Fig. 4.12(c). From this operator, we can then determine the form of the new flux excitation. Since the operator still takes the shape of a wire-frame, we can see from its truncation that the flux excitations are still lineons. This conclusion is consistent with that obtained in section 4.2 but applies more generally. In particular, the argument we use in this section is independent of the symmetric

state of the fracton and planon charges, so it works even when they form some nontrivial symmetry-protected topological state.

Remote detection in Model FP2

A similar argument can be applied to Model FP2. We will see how the difference in the composite symmetry results in a different binding of fluxes compared to Model FP1, such that the new fluxes are planons instead of lineons. In Model FP2, the fracton charges are still at the lattice sites of a cubic lattice, while the planon charges lie on the xy, yz, and zx planes of the cubic lattice. The planar symmetries are combined so that there is a new type of minimal coupling term containing the fracton charge and three planon charges at the same lattice site, as shown in Fig. 4.13 (a). To not detect this term, we need to combine the wire-frame operator with all the loop operators that wind around the wire-frame in a particular direction. For example, Fig. 4.13 (b) shows one such operator with the wire-frame bound to loop operators in the xy plane. There are two other types of operators with loops in the yz and zx planes, respectively.

We can check that: 1. individual fracton charges and fracton dipoles can still be detected if properly placed inside the decorated wire-frame operator; 2. individual planon charges can still be detected if placed inside the wire-frame operator with loop operators in the same plane; 3. the new four-body minimal coupling cannot be detected by any of the new remote detection operators as shown in Fig. 4.13 (c). Truncating the remote detection operator exposes the new flux excitations. The operator is not a wire-frame anymore but instead takes the shape of a ribbon loop. When the ribbon is thin, the endpoints of the truncated operator are point excitations that move in planes. Therefore, the elementary flux excitations are planons in xy, yz, and zx planes, respectively. Again, this result is derived independent of the symmetric state formed by the fractons and planons.

4.4 Decoration of sub-dimensional excitations

The flux-binding result derived in section 4.3 allows us to construct interesting fracton models by binding lineons / fractons with planons, thereby passing the non-trivial statistics or non-abelian internal structure of the planons onto the lineons or fractons. We discuss the decoration of lineon excitations and fracton excitations. In particular, we demonstrate how some of the cage-net models discussed in Ref. [42] can be obtained by gauging the subsystem symmetry of an SSPT (subsystem symmetry protected topological) model.

Decoration of lineons

To construct the models with the decoration of lineon flux superselection sectors, we follow the construction of Model FP1 (Sec. 4.2) but use the 2D symmetry-protected topological phases (SPT) or symmetry-enriched topological orders (SET) with $\mathbb{Z}_2$ planar symmetry as the planon-charge systems (see Fig. 4.14). We recall that in Model FP1, the new gauge flux is a composite of the original lineon flux of the fracton-charge system and two planon fluxes from orthogonal planon-charge systems. Below, we consider examples where we replace the 2D Ising paramagnet on the ungauged side by the 2D Levin-Gu SPT with global $\mathbb{Z}_2$ symmetry or the 2D toric code with global $e \leftrightarrow m$ anyon-swap symmetry. We obtain decorated lineon superselection sectors with nontrivial statistics or non-abelian fusion rules in these cases.

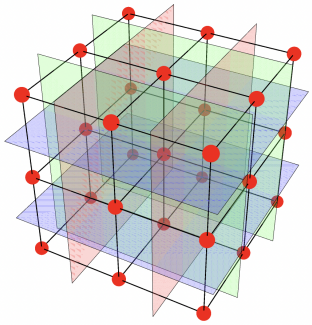

Figure 4.14: The general setup for Model FP1. We have a fracton-charge system (red spheres) and 2D planon-charge systems (colored planes). The green, blue, and red planes represent the planon-charge system, which are in some potentially non-trivial SPT or SET states.

- *Example of Model FP1 with decorated lineons that have nontrivial statistics* We consider an example of Model FP1 where we introduce nontrivial $\mathbb{Z}_2$ SPTs as the planon-charge systems. In particular, we can use the Levin-Gu SPTs [103] as the planon-charge systems. Gauging just the $\mathbb{Z}_2$ symmetry of the Levin-Gu SPT yields the double semion model that has two semionic fluxes. The flux binding result of Model FP1 implies that upon gauging its composite symmetry, the two semionic fluxes from two orthogonal double semion planes must bind with the lineon flux of the fracton-charge system to yield a lineon flux composite. The resulting 3D model is the 3D semionic X-cube model [41]. One can show that two lineon fluxes of this model have mutual statistics of π by designing processes analogous to braiding in 2D topological orders [41].

- *Example of Model FP1 with decorated lineons that have non-abelian fusion rules*

  We now discuss an example of Model FP1, where we introduce nontrivial SETs as the planon-charge systems. For instance, we consider toric code SETs (enriched by the $e-m$ swap symmetry) and gauge the composite symmetry that is a product of this planar swap symmetry and the planar symmetries of the fracton-charge system. Gauging the swap symmetry alone in the toric code layer would give the doubled Ising string-net model with non-abelian fluxes, the Ising anyons σ's and $\bar{\sigma}$'s, each with quantum dimension $\sqrt{2}$. On gauging the composite symmetry, the non-abelian Ising anyons from orthogonal doubled-Ising string-net planes must bind with the lineon flux of the gauged fracton-charge system to yield a decorated lineon flux that is non-abelian with quantum dimension 2. The resulting 3D model is the Ising cage-net model [42].

4.5 Decoration of fractons: Model LP

We now consider a different model of flux binding such that we obtain decorated fracton superselection sectors. In particular, we consider a class of models obtained from combining a 3D lineon-charge system with three stacks of 2D planon-charge systems. Hence, we refer to this class of models as Model LP. The key difference between Model LP and Model FP1 is that the construction of the former uses a lineon-charge system, while the latter uses a fracton-charge system instead in its construction. It is due to this change that the gauged model hosts decorated fracton flux superselection sectors instead of decorated lineon flux superselection sectors; the fracton flux is a composite of the original fracton flux with three planon fluxes, each from a different 2D system.

We demonstrate Model LP's flux binding of fracton flux with planon fluxes by considering a 3D Ising paramagnet with planar symmetries as the lineon-charge system and stacks of 2D models with on-site $\mathbb{Z}_2$ planar symmetries as the planar-charge systems. This lineon-charge system, a 3D Ising paramagnet with planar symmetries, is "dual" to the fracton-charge system discussed earlier; gauging the planar systems in either of these, i.e., the lineon-charge system or the fracton-charge system, yields the X-cube model [32]. The difference in the resulting gauged models is that in the gauging of the lineon-charge system, the X-cube fracton is the flux excitation, while in the gauging of the fracton-charge system, the X-cube lineon is the flux excitation.

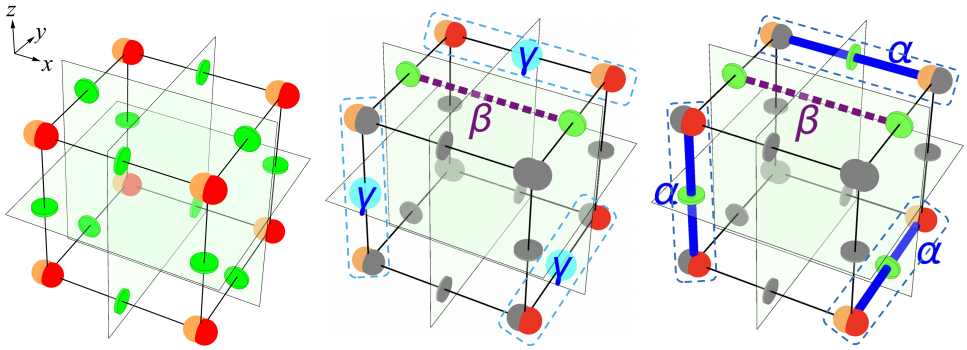

(a) (b) (c)

Figure 4.15: Model LP: lattice setup. We take the 3D lineon-charge system, a model that is dual to the fracton-charge system [32], on the cubic lattice. The orange and red spheres represent the qubits. As in Model FP1 (Sec. 4.2), we insert three stacks of the 2D planon-charge systems bisecting the edges. The green disks show their qubits. (b) & (c): the minimal coupling terms. (a): all three kinds of the original minimal coupling terms γ of the 3D lineon-charge system (inside the dashed cyan colored loops), and an example of the minimal coupling of the planon-charge systems β. (b): the new minimal coupling terms α for the composite symmetry are highlighted by the dashed blue loops. The β's and γ's remain minimal coupling terms for the composite symmetry.

We put the lineon-charge system on the cubic lattice with two matter qubits per vertex, the orange and the red spheres in Fig. 4.15. The orange spins transform under the planar symmetries of the y- and x-planes, and the red spins transform under the z- and x-planes. These subsystem symmetries are defined by: $\prod_{v\in P^x_{i_x}} X^r_v X^o_v$ for the x-planes; $\prod_{v\in P^y_{i_y}} X^o_v$ for the y-planes; and $\prod_{v\in P^z_{i_z}} X^r_v$ for the z-planes. We place the qubits of the planon-charge systems on the edges. We recall that each planon-charge system has the 2D global symmetry of $\prod_{\rho\in P^\mu_{(i_\mu,i_\mu+1)}} X_\rho$ where $(i_\mu, i_\mu+1)$ indicates the edges on which the qubits of the planon-charge systems live. Like Model FP1, the composite symmetry we gauge here also has a sandwiched structure. Specifically, for each direction, we consider the symmetry generators,

$$\mathcal{S}^x_{i_x} = \prod_{\rho\in P^x_{(i_x,i_x+1)}} \prod_{v\in P^x_{i_x}} \prod_{\rho'\in P^x_{(i_x-1,i_x)}} X_\rho X^r_v X^o_v X_{\rho'}, \tag{4.9}$$

$$\mathcal{S}^y_{i_y} = \prod_{\rho\in P^y_{(i_y,i_y+1)}} \prod_{v\in P^y_{i_y}} \prod_{\rho'\in P^y_{(i_y-1,i_y)}} X_\rho X^o_v X_{\rho'}, \tag{4.10}$$

$$\mathcal{S}^z_{i_z} = \prod_{\rho\in P^z_{(i_z,i_z+1)}} \prod_{v\in P^z_{i_z}} \prod_{\rho'\in P^z_{(i_z-1,i_z)}} X_\rho X^r_v X_{\rho'}. \tag{4.11}$$

We illustrate the minimal couplings associated with the original decoupled symmetries and the new composite symmetry in Fig. 4.15(b) and Fig. 4.15(c) respectively.

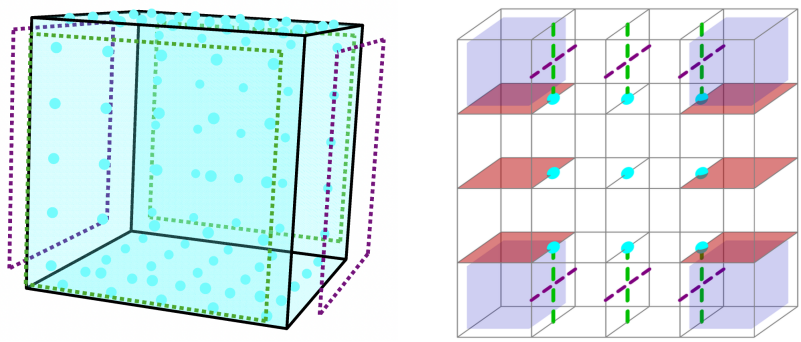

(a) (b)

Figure 4.16: Model LP: flux binding from remote detection operators. (a): A new charge remote detection (RD) operator, which is built from the original RD operators supported on four sides of the cube. The membrane charge RD operator of the lineon-charge system is drawn in cyan color. The green and purple loops are the RD operators of the planon-charge system on the y- and z-planes, respectively. (b): cutting the charge RD operator reveals a membrane with fractons (purple cubes) at the corners and planons (red plaquettes and green and purple edges) along the sides.

We denote the original minimal couplings (for decoupled symmetries) as β and γ while the new minimal couplings (for composite symmetries) as α. The α terms along different directions $x|y|z$ are specified by adding a subscript $(x)|(y)|(z)$.

We can determine the flux binding of this model using the principle of Remote Detectability[5]. We recall from Sec. 4.3 that the closed local membrane operators for the new fluxes in the model obtained by gauging the composite symmetry are the RD operators for the charges. These new RD operators can be constructed using the original RD operators such that they do not detect the 'composite condensates', i.e., the charges associated with the new minimal couplings that were not present for decoupled symmetries. For example, consider the RD operator for charges of the lineon-charge system, drawn in cyan in Fig. 4.16(a). This operator detects the original x and y lineons. So, it can also detect our 'composite condensates' associated with $\alpha_{(z)}$ and $\alpha_{(y)}$ coupling terms. To prevent the detection of $\alpha_{(z)}$, we add two remote detection operators of the planon-charge system on the side planes (the purple loops). Similarly, for $\alpha_{(y)}$, we add two remote detection operators on the front and back faces, as indicated by the green loops. This yields the required remote detection operator, as stated earlier. By slicing this closed membrane operator, we get the creation operator for the new fracton flux, as shown in Fig. 4.16(b). The excitation created by this sliced membrane operator is our bound flux excitation

[5]See Section 4.5 for an alternative explanation of flux binding by writing the gauged model and looking at independent superselection sectors.

which is a composite of the original fracton fluxes of the gauged lineon-charge system and three planon fluxes from the gauged planon-charge systems in orthogonal layers.

Above, we described a particular example of Model LP class to demonstrate the flux binding that yields decorated fractons. In general, we can consider different planon-charge systems with global $\mathbb{Z}_2$ symmetry instead of the 2D Ising paramagnet. The general setup for Model LP is illustrated in Fig. 4.17.

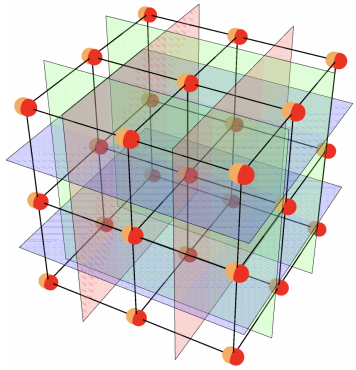

Figure 4.17: The general setup for Model LP. The Model LP consists of a lineon-charge system and a stack of 2D planon-charge systems. The lineon-charge system has red and orange qubits on vertices, and the 2D planon-charge systems live on dual planes, as shown. The composite symmetry generators act on the qubits of the lineon-charge system and the planon-charge system together.

We now present an example of ModelLP where we use nontrivial SETs as the planon-charge systems. For instance, we consider 2D toric code SETs (enriched by the e-m swap symmetry) as planon-charge systems. We gauge the composite symmetry, each generator of which is a product of the swap symmetries of two toric code layers and a planar symmetry of the lineon-charge system. As mentioned earlier, gauging the swap symmetry alone in the toric code layer would give the doubled Ising string-net model with non-abelian planons; the gauge fluxes are the Ising anyons σ's and $\bar{\sigma}$'s, each with quantum dimension $\sqrt{2}$. Now, in the case of gauging the composite symmetry, the fractons in the model obtained from gauging composite symmetry are decorated with these non-abelian anyons and are, hence, non-abelian. In particular, three non-abelian planon fluxes decorate the original fracton flux; hence, this decorated fracton flux has a quantum dimension of $(\sqrt{2})^3$. This model is similar to that constructed from the Ising anyons in Ref. [39, 57]. However, the non-abelian fracton model obtained here is different from the model in Ref. [39] where the planons are non-abelian and the model in Ref. [57] where

the non-abelian fracton has a quantum dimension of $\sqrt{2}$. To give this new model a name, we call it the *tri-Ising-fracton model*. We note that it is also possible to obtain non-abelian fractons from gauging twisted abelian theories as discussed in Ref. [59].

Model LP: gauged Hamiltonian

We have introduced a lineon-charge system that is the dual of the fracton-charge system used in Sec. 4.2. Gauging this model yields the X-cube model but now with the identification of the fracton superselection sectors as fluxes. We added three stacks of 2D planon charge systems to the model (shown in Fig. 4.15(a)) and gauged a composite symmetry with generators supported on both models to yield the model LP with decorated fracton superselection sectors. To illustrate the flux binding that leads to the decorated fracton superselection sectors, we constructed the remote detection operator (a membrane operator shown in Fig. 4.16(c)) of the fluxes in the model with gauged composite symmetry. In this Section, we show the flux binding by writing the fully gauged Hamiltonian.

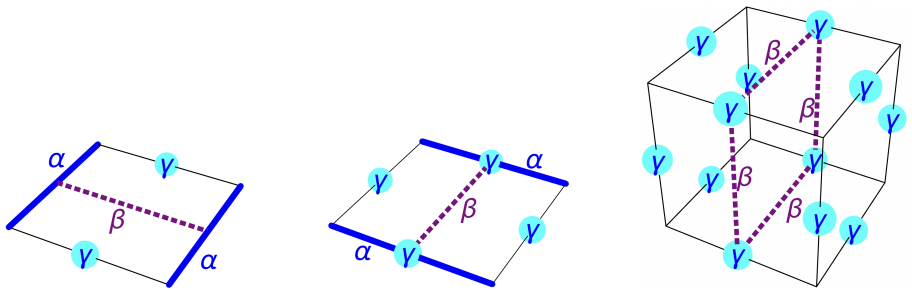

Figure 4.18: Model LP: the $\boldsymbol{E}$-type flux terms. Drawn here are: (a) the $\boldsymbol{E}_p^{[z](x)}$, and (b) the $\boldsymbol{E}_p^{[z](y)}$ terms. The remaining $\boldsymbol{E}_p^{[x](\cdot)}$ and $\boldsymbol{E}_p^{[y](\cdot)}$ terms are similar. (c): one of the three relations between the original flux terms, which is the product of a cube flux term of the lineon-charge system and a plaquette flux term of the planon-charge system. It is obtained from multiplying the $\boldsymbol{E}$-type flux terms around the faces of a cube. The other two relations can be obtained by rotations.

Following the procedure in Sec. 4.2, we add gauge fields to the coupling terms as shown in (b) and (c) of Fig. 4.15.

$$\begin{aligned} H^{LP} = &- \sum_{x' \in P^x_{(i_x, i_x+1)}} \sum_{y' \in P^y_{(i_y, i_y+1)}} \sum_{z' \in P^z_{(i_z, i_z+1)}} \boldsymbol{\Gamma}^{(x',y',z')} \\ &- \sum_{\mu, \{i_\mu\}} \left(\sum_{p \in P^\mu_{(i_\mu, i_\mu+1)}} \boldsymbol{C}_p^\mu + \sum_{\nu, p \in P^\mu_{i_\mu}} \boldsymbol{E}_p^{[\mu](\nu)} \right) - (\text{charge terms}). \end{aligned} \tag{4.12}$$

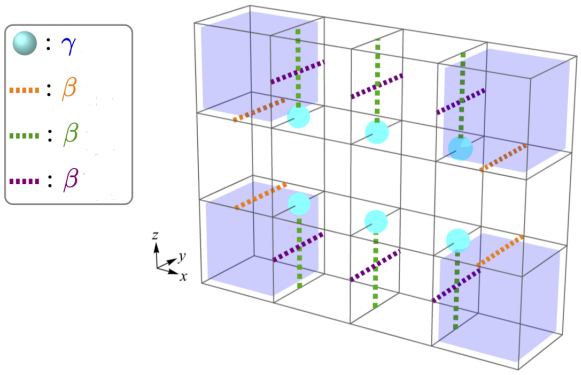

Figure 4.19: Model LP: the new fracton membrane operator where the fractons are created at the four corners, the blue cubes. The new fracton flux is a product of three original planon fluxes from three mutually perpendicular planon-charge systems together with the original fracton flux from the 3D lineon-charge system.

The $\boldsymbol{\Gamma}$-type flux terms are the original 12-body cube fluxes of the lineon-charge system. The $\boldsymbol{C}$-type flux terms are the original 4-body plaquette fluxes of the planon-charge system (shown in Fig. 4.6(a)). The $\boldsymbol{E}$-type flux terms, involving both the original minimal couplings and the new minimal couplings, are given in (a) and (b) of Fig. 4.18. Since these $\boldsymbol{E}$ terms do not contribute to the superselection sectors (since they can be converted to $\boldsymbol{C}$-type fluxes via a $\beta^x_{[\mu](\nu)}$ operator), we can set them to the identity. This yields relations between the original flux terms, e.g. (c) of Fig. 4.18. The product of 4 $\boldsymbol{E}$ terms around the faces of a cube equals the identity, but it is also equivalent to the product of a $\boldsymbol{\Gamma}$ and a $\boldsymbol{C}$ flux term. Using these constraints, we construct the logical operator for the new flux excitation in Fig. 4.19. The new flux is also a fracton since it is a composite of an original fracton together with three original planon fluxes, each from a different 2D system.

4.6 Connection to cage-net fracton models

In Sec. 4.4, we saw that Model FP1 (Sec. 4.2) can give rise to the cage-net fracton models [41, 42]. The cage-net models are constructed using three stacks of 2D topological orders and then coupled with particle-loop (p-loop) condensation. Here, we show how the p-loop condensation can be understood as gauging a composite symmetry.

Consider two 'composite condensates' in the z-direction, i.e. the charges associated with the $\alpha_{(z)}$-coupling term, Fig. 4.5(a). And two 'composite condensates' in the x-direction. The product of these four terms is equal to four planon charges on the same face of a cube, Fig. 4.20. If we represent a planon charge by a line orthogonal

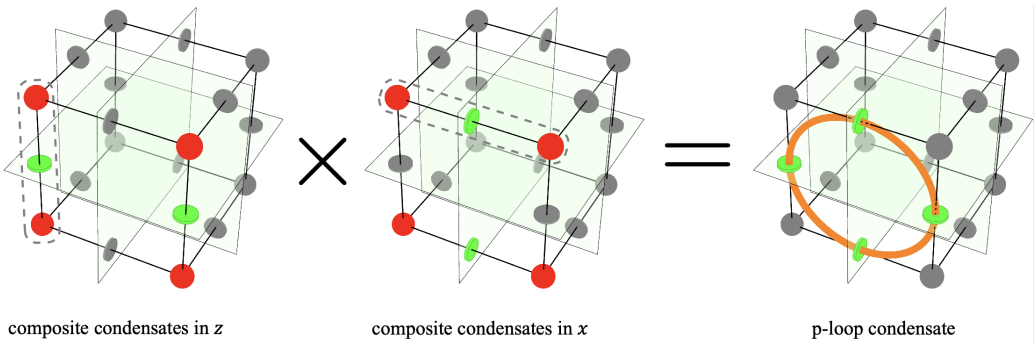

Figure 4.20: Particle-loop (p-loop) condensation in Model FP1. The p-loop, the orange loop on the RHS, is generated by the 'composite condensates' on the LHS.

to its plane, then we get a loop, i.e. the orange loop in Fig. 4.20. This loop is precisely the p-loop considered in Ref. [41, 42]. Since we constructed this p-loop through the 'composite condensates', it is also condensed. Therefore, gauging the composite symmetry is the same as condensing the p-loop. We can then regard Model FP1 as the ungauged version of the cage-net fracton models.

4.7 The models and their generalized foliated fracton orders

The model obtained by gauging the composite symmetry can be equivalently obtained by condensing a composite of gauge charges in the gauged decoupled models. This composite gauge charge corresponds to the new minimal coupling obtained for the composite symmetry. We expect that such a condensation can be realized using a sequential linear-depth circuit. Since we consider only planar symmetries in this work, such a sequential linear-depth circuit would also be in-plane. In particular, starting from Model FP1 or FP2, we can obtain the gauged decoupled models by application of in-plane sequential linear-depth circuits that condense fractional excitations in foliations. The gauged models could, hence, be understood as generalized foliated fracton models where the notion of generalized foliation is described in Chapter 3. Thus, in this sense of generalized foliation, our models are equivalent to the decoupled models[6]. On the ungauged side, this corresponds to having a weak subsystem symmetry-protected topological phase (SSPT) [33] if we apply the notion of generalized foliation in the definition of SSPTs. Thus, we expect the models obtained by gauging strong SSPTs cannot be obtained using the construction presented in this work.

[6]Therefore, for example, the Ising cage-net and the tri-Ising-fracton model are in the same generalized foliated fracton order as the X-cube.

BIBLIOGRAPHY

[1] J. F. Kaiser. "Richard Hamming - You and Your Research". In: *Simula Research Laboratory: by Thinking Constantly about it*. Ed. by Aslak Tveito, Are Magnus Bruaset, and Olav Lysne. Berlin, Heidelberg: Springer Berlin Heidelberg, 2010, pp. 37–60. ISBN: 978-3-642-01156-6. DOI: 10.1007/978-3-642-01156-6_6.

[2] Michael A. Nielsen and Isaac L. Chuang. *Quantum Computation and Quantum Information: 10th Anniversary Edition*. Cambridge University Press, 2010.

[3] Ilya N. Moskalenko, Ilya A. Simakov, Nikolay N. Abramov, Alexander A. Grigorev, Dmitry O. Moskalev, Anastasiya A. Pishchimova, Nikita S. Smirnov, Evgeniy V. Zikiy, Ilya A. Rodionov, and Ilya S. Besedin. "High fidelity two-qubit gates on fluxoniums using a tunable coupler". In: *npj Quantum Information* 8.1 (Nov. 2022), p. 130. ISSN: 2056-6387. DOI: 10.1038/s41534-022-00644-x.

[4] Dongxin Gao et al. "Establishing a New Benchmark in Quantum Computational Advantage with 105-qubit Zuchongzhi 3.0 Processor". In: *Phys. Rev. Lett.* 134 (9 Mar. 2025), p. 090601. DOI: 10.1103/PhysRevLett.134.090601.

[5] Nicolas Maring et al. "A versatile single-photon-based quantum computing platform". In: *Nature Photonics* 18.6 (June 2024), pp. 603–609. ISSN: 1749-4893. DOI: 10.1038/s41566-024-01403-4.

[6] S. A. Moses et al. "A Race-Track Trapped-Ion Quantum Processor". In: *Phys. Rev. X* 13 (4 Dec. 2023), p. 041052. DOI: 10.1103/PhysRevX.13.041052.

[7] Simon J. Evered, Dolev Bluvstein, Marcin Kalinowski, Sepehr Ebadi, Tom Manovitz, Hengyun Zhou, Sophie H. Li, Alexandra A. Geim, Tout T. Wang, Nishad Maskara, Harry Levine, Giulia Semeghini, Markus Greiner, Vladan Vuletić, and Mikhail D. Lukin. "High-fidelity parallel entangling gates on a neutral-atom quantum computer". In: *Nature* 622.7982 (Oct. 2023), pp. 268–272. ISSN: 1476-4687. DOI: 10.1038/s41586-023-06481-y.

[8] C. M. Löschnauer, J. Mosca Toba, A. C. Hughes, S. A. King, M. A. Weber, R. Srinivas, R. Matt, R. Nourshargh, D. T. C. Allcock, C. J. Ballance, C. Matthiesen, M. Malinowski, and T. P. Harty. *Scalable, high-fidelity all-electronic control of trapped-ion qubits*. 2024. arXiv: 2407.07694 [quant-ph].

[9] Jwo-Sy Chen, Erik Nielsen, Matthew Ebert, Volkan Inlek, Kenneth Wright, Vandiver Chaplin, Andrii Maksymov, Eduardo Páez, Amrit Poudel, Peter Maunz, and John Gamble. "Benchmarking a trapped-ion quantum computer

with 30 qubits". In: *Quantum* 8 (Nov. 2024), p. 1516. ISSN: 2521-327X. DOI: 10.22331/q-2024-11-07-1516.

[10] David C. McKay, Ian Hincks, Emily J. Pritchett, Malcolm Carroll, Luke C. G. Govia, and Seth T. Merkel. *Benchmarking Quantum Processor Performance at Scale*. 2023. arXiv: 2311.05933 [quant-ph].

[11] Ben W. Reichardt et al. *Logical computation demonstrated with a neutral atom quantum processor*. 2024. arXiv: 2411.11822 [quant-ph].

[12] Leonid Abdurakhimov et al. *Technology and Performance Benchmarks of IQM's 20-Qubit Quantum Computer*. 2024. arXiv: 2408.12433 [quant-ph].

[13] Xuandong Sun et al. *Universal logical operations with a dynamical qubit in Floquet code*. 2025. arXiv: 2503.03867 [quant-ph].

[14] Asher Peres. "Reversible logic and quantum computers". In: *Phys. Rev. A* 32 (6 Dec. 1985), pp. 3266–3276. DOI: 10.1103/PhysRevA.32.3266.

[15] Michael H. Freedman and Matthew B. Hastings. "Quantum systems on non-k-hyperfinite complexes: a generalization of classical statistical mechanics on expander graphs". In: *Quantum Info. Comput.* 14.1–2 (Jan. 2014), pp. 144–180. ISSN: 1533-7146.

[16] Peter W. Shor. "Scheme for reducing decoherence in quantum computer memory". In: *Phys. Rev. A* 52 (4 Oct. 1995), R2493–R2496. DOI: 10.1103/PhysRevA.52.R2493.

[17] A.Yu. Kitaev. "Fault-tolerant quantum computation by anyons". In: *Annals of Physics* 303.1 (2003), pp. 2–30. ISSN: 0003-4916. DOI: https://doi.org/10.1016/S0003-4916(02)00018-0.

[18] Rajeev Acharya et al. "Quantum error correction below the surface code threshold". In: *Nature* 638.8052 (Feb. 2025), pp. 920–926. ISSN: 1476-4687. DOI: 10.1038/s41586-024-08449-y.

[19] Olivier Landon-Cardinal, Beni Yoshida, David Poulin, and John Preskill. "Perturbative instability of quantum memory based on effective long-range interactions". In: *Phys. Rev. A* 91 (3 Mar. 2015), p. 032303. DOI: 10.1103/PhysRevA.91.032303.

[20] Eric Dennis, Alexei Kitaev, Andrew Landahl, and John Preskill. "Topological quantum memory". In: *Journal of Mathematical Physics* 43.9 (Sept. 2002), pp. 4452–4505. ISSN: 0022-2488. DOI: 10.1063/1.1499754.

[21] Sergey Bravyi and Barbara Terhal. "A no-go theorem for a two-dimensional self-correcting quantum memory based on stabilizer codes". In: *New Journal of Physics* 11.4 (Apr. 2009), p. 043029. DOI: 10.1088/1367-2630/11/4/043029.

[22] Jeongwan Haah and John Preskill. "Logical-operator tradeoff for local quantum codes". In: *Phys. Rev. A* 86 (3 Sept. 2012), p. 032308. DOI: 10.1103/PhysRevA.86.032308.

[23] Alastair Kay and Roger Colbeck. *Quantum Self-Correcting Stabilizer Codes*. 2008. arXiv: 0810.3557 [quant-ph].

[24] Jeongwan Haah. "Local stabilizer codes in three dimensions without string logical operators". In: *Phys. Rev. A* 83 (4 Apr. 2011), p. 042330. DOI: 10.1103/PhysRevA.83.042330.

[25] Sagar Vijay, Jeongwan Haah, and Liang Fu. "Fracton topological order, generalized lattice gauge theory, and duality". In: *Phys. Rev. B* 94 (23 Dec. 2016), p. 235157. DOI: 10.1103/PhysRevB.94.235157.

[26] Sergey Bravyi and Jeongwan Haah. "Quantum Self-Correction in the 3D Cubic Code Model". In: *Phys. Rev. Lett.* 111 (20 Nov. 2013), p. 200501. DOI: 10.1103/PhysRevLett.111.200501.

[27] Cory T. Aitchison, Daniel Bulmash, Arpit Dua, Andrew C. Doherty, and Dominic J. Williamson. "Boundaries and defects in the cubic code". In: *Phys. Rev. B* 109 (20 May 2024), p. 205125. DOI: 10.1103/PhysRevB.109.205125.

[28] Alioscia Hamma, Paolo Zanardi, and Xiao-Gang Wen. "String and membrane condensation on three-dimensional lattices". In: *Phys. Rev. B* 72 (3 July 2005), p. 035307. DOI: 10.1103/PhysRevB.72.035307.

[29] Xiao-Gang Wen. "Colloquium: Zoo of quantum-topological phases of matter". In: *Rev. Mod. Phys.* 89 (4 Dec. 2017), p. 041004. DOI: 10.1103/RevModPhys.89.041004.

[30] Claudio Chamon. "Quantum Glassiness in Strongly Correlated Clean Systems: An Example of Topological Overprotection". In: *Phys. Rev. Lett.* 94 (4 Jan. 2005), p. 040402. DOI: 10.1103/PhysRevLett.94.040402.

[31] Sergey Bravyi, Bernhard Leemhuis, and Barbara M. Terhal. "Topological order in an exactly solvable 3D spin model". In: *Annals of Physics* 326.4 (2011), pp. 839–866. ISSN: 0003-4916. DOI: https://doi.org/10.1016/j.aop.2010.11.002.

[32] Wilbur Shirley, Kevin Slagle, and Xie Chen. "Foliated fracton order from gauging subsystem symmetries". In: *SciPost Phys.* 6 (2019), p. 041. DOI: 10.21468/SciPostPhys.6.4.041.

[33] Trithep Devakul, Wilbur Shirley, and Juven Wang. "Strong planar subsystem symmetry-protected topological phases and their dual fracton orders". In: *Phys. Rev. Res.* 2 (1 Mar. 2020), p. 012059. DOI: 10.1103/PhysRevResearch.2.012059.

[34] Dominic J. Williamson. "Fractal symmetries: Ungauging the cubic code". In: *Phys. Rev. B* 94 (15 Oct. 2016), p. 155128. DOI: 10.1103/PhysRevB.94.155128.

[35] Nathanan Tantivasadakarn, Wenjie Ji, and Sagar Vijay. "Hybrid fracton phases: Parent orders for liquid and nonliquid quantum phases". In: *Phys. Rev. B* 103 (24 June 2021), p. 245136. DOI: 10.1103/PhysRevB.103.245136.

[36] Nathanan Tantivasadakarn, Wenjie Ji, and Sagar Vijay. "Non-Abelian hybrid fracton orders". In: *Phys. Rev. B* 104 (11 Sept. 2021), p. 115117. DOI: 10.1103/PhysRevB.104.115117.

[37] Avi Vadali, Zongyuan Wang, Arpit Dua, Wilbur Shirley, and Xie Chen. "Composite subsystem symmetries and decoration of sub-dimensional excitations". In: *SciPost Phys.* 17 (2024), p. 071. DOI: 10.21468/SciPostPhys.17.3.071.

[38] Dominic J. Williamson and Trithep Devakul. "Type-II fractons from coupled spin chains and layers". In: *Phys. Rev. B* 103 (15 Apr. 2021), p. 155140. DOI: 10.1103/PhysRevB.103.155140.

[39] Sagar Vijay and Liang Fu. *A Generalization of Non-Abelian Anyons in Three Dimensions*. 2017. arXiv: 1706.07070 [cond-mat.str-el].

[40] Gábor B. Halász, Timothy H. Hsieh, and Leon Balents. "Fracton Topological Phases from Strongly Coupled Spin Chains". In: *Phys. Rev. Lett.* 119 (25 Dec. 2017), p. 257202. DOI: 10.1103/PhysRevLett.119.257202.

[41] Han Ma, Ethan Lake, Xie Chen, and Michael Hermele. "Fracton topological order via coupled layers". In: *Phys. Rev. B* 95 (24 June 2017), p. 245126. DOI: 10.1103/PhysRevB.95.245126.

[42] Abhinav Prem, Sheng-Jie Huang, Hao Song, and Michael Hermele. "Cage-Net Fracton Models". In: *Phys. Rev. X* 9 (2 Apr. 2019), p. 021010. DOI: 10.1103/PhysRevX.9.021010.

[43] Michael Pretko. "Subdimensional particle structure of higher rank $U(1)$ spin liquids". In: *Phys. Rev. B* 95 (11 Mar. 2017), p. 115139. DOI: 10.1103/PhysRevB.95.115139.

[44] Michael Pretko. "Generalized electromagnetism of subdimensional particles: A spin liquid story". In: *Phys. Rev. B* 96 (3 July 2017), p. 035119. DOI: 10.1103/PhysRevB.96.035119.

[45] Daniel Bulmash and Maissam Barkeshli. "Higgs mechanism in higher-rank symmetric U(1) gauge theories". In: *Phys. Rev. B* 97 (23 June 2018), p. 235112. DOI: 10.1103/PhysRevB.97.235112.

[46] Han Ma, Michael Hermele, and Xie Chen. "Fracton topological order from the Higgs and partial-confinement mechanisms of rank-two gauge theory". In: *Phys. Rev. B* 98 (3 July 2018), p. 035111. DOI: 10.1103/PhysRevB.98.035111.

[47] Dominic J. Williamson, Zhen Bi, and Meng Cheng. "Fractonic matter in symmetry-enriched $U(1)$ gauge theory". In: *Phys. Rev. B* 100 (12 Sept. 2019), p. 125150. DOI: 10.1103/PhysRevB.100.125150.

[48] Nathan Seiberg and Shu-Heng Shao. "Exotic $U(1)$ symmetries, duality, and fractons in 3+1-dimensional quantum field theory". In: *SciPost Phys.* 9 (2020), p. 046. DOI: 10.21468/SciPostPhys.9.4.046.

[49] Alexei Kitaev. "Anyons in an exactly solved model and beyond". In: *Annals of Physics* 321.1 (Jan. 2006), pp. 2–111. ISSN: 0003-4916. DOI: 10.1016/j.aop.2005.10.005.

[50] Tian Lan, Liang Kong, and Xiao-Gang Wen. "Classification of (3 + 1)D Bosonic Topological Orders: The Case When Pointlike Excitations Are All Bosons". In: *Phys. Rev. X* 8 (2 June 2018), p. 021074. DOI: 10.1103/PhysRevX.8.021074.

[51] Tian Lan and Xiao-Gang Wen. "Classification of 3+1D Bosonic Topological Orders (II): The Case When Some Pointlike Excitations Are Fermions". In: *Phys. Rev. X* 9 (2 Apr. 2019), p. 021005. DOI: 10.1103/PhysRevX.9.021005.

[52] Wilbur Shirley, Kevin Slagle, Zhenghan Wang, and Xie Chen. "Fracton Models on General Three-Dimensional Manifolds". In: *Phys. Rev. X* 8 (3 Aug. 2018), p. 031051. DOI: 10.1103/PhysRevX.8.031051.

[53] Wilbur Shirley, Kevin Slagle, and Xie Chen. "Fractional excitations in foliated fracton phases". In: *Annals of Physics* 410 (2019), p. 167922. ISSN: 0003-4916. DOI: https://doi.org/10.1016/j.aop.2019.167922.

[54] Wilbur Shirley, Kevin Slagle, and Xie Chen. "Foliated fracton order in the checkerboard model". In: *Phys. Rev. B* 99 (11 Mar. 2019), p. 115123. DOI: 10.1103/PhysRevB.99.115123.

[55] Taige Wang, Wilbur Shirley, and Xie Chen. "Foliated fracton order in the Majorana checkerboard model". In: *Phys. Rev. B* 100 (8 Aug. 2019), p. 085127. DOI: 10.1103/PhysRevB.100.085127.

[56] Abhinav Prem and Dominic J. Williamson. "Gauging permutation symmetries as a route to non-Abelian fractons". In: *SciPost Phys.* 7 (2019), p. 068. DOI: 10.21468/SciPostPhys.7.5.068.

[57] Dominic J. Williamson and Meng Cheng. "Designer non-Abelian fractons from topological layers". In: *Phys. Rev. B* 107 (3 Jan. 2023), p. 035103. DOI: 10.1103/PhysRevB.107.035103.

[58] Yi-Ting Tu and Po-Yao Chang. "Non-Abelian fracton order from gauging a mixture of subsystem and global symmetries". In: *Phys. Rev. Res.* 3 (4 Oct. 2021), p. 043084. DOI: 10.1103/PhysRevResearch.3.043084.

[59] Hao Song, Abhinav Prem, Sheng-Jie Huang, and M. A. Martin-Delgado. "Twisted fracton models in three dimensions". In: *Phys. Rev. B* 99 (15 Apr. 2019), p. 155118. DOI: 10.1103/PhysRevB.99.155118.

[60] Daniel Bulmash and Maissam Barkeshli. "Gauging fractons: Immobile non-Abelian quasiparticles, fractals, and position-dependent degeneracies". In: *Phys. Rev. B* 100 (15 Oct. 2019), p. 155146. DOI: 10.1103/PhysRevB.100.155146.

[61] Joseph Sullivan, Thomas Iadecola, and Dominic J. Williamson. "Planar p-string condensation: Chiral fracton phases from fractional quantum Hall layers and beyond". In: *Phys. Rev. B* 103 (20 May 2021), p. 205301. DOI: 10.1103/PhysRevB.103.205301.

[62] David Aasen, Daniel Bulmash, Abhinav Prem, Kevin Slagle, and Dominic J. Williamson. "Topological defect networks for fractons of all types". In: *Phys. Rev. Res.* 2 (4 Oct. 2020), p. 043165. DOI: 10.1103/PhysRevResearch.2.043165.

[63] Wilbur Shirley, Kevin Slagle, and Xie Chen. "Universal entanglement signatures of foliated fracton phases". In: *SciPost Phys.* 6 (2019), p. 015. DOI: 10.21468/SciPostPhys.6.1.015.

[64] Wilbur Shirley, Kevin Slagle, and Xie Chen. "Twisted foliated fracton phases". In: *Phys. Rev. B* 102 (11 Sept. 2020), p. 115103. DOI: 10.1103/PhysRevB.102.115103.

[65] Xiuqi Ma, Wilbur Shirley, Meng Cheng, Michael Levin, John McGreevy, and Xie Chen. "Fractonic order in infinite-component Chern-Simons gauge theories". In: *Phys. Rev. B* 105 (19 May 2022), p. 195124. DOI: 10.1103/PhysRevB.105.195124.

[66] Xie Chen, Ho Tat Lam, and Xiuqi Ma. *Gapless Infinite-component Chern-Simons-Maxwell Theories*. 2022. arXiv: 2211.10458 [cond-mat.str-el].

[67] Xie Chen, Ho Tat Lam, and Xiuqi Ma. *Ground State Degeneracy of Infinite-Component Chern-Simons-Maxwell Theories*. 2023. arXiv: 2306.00291 [cond-mat.str-el].

[68] Michael A. Levin and Xiao-Gang Wen. "String-net condensation: A physical mechanism for topological phases". In: *Phys. Rev. B* 71 (4 Jan. 2005), p. 045110. DOI: 10.1103/PhysRevB.71.045110.

[69] D. A. Ivanov. "Non-Abelian Statistics of Half-Quantum Vortices in *p*-Wave Superconductors". In: *Phys. Rev. Lett.* 86 (2 Jan. 2001), pp. 268–271. DOI: 10.1103/PhysRevLett.86.268.

[70] Xueda Wen and Xiao-Gang Wen. "Distinguish modular categories and 2+1D topological orders beyond modular data: Mapping class group of higher genus manifold". In: (Aug. 2019). arXiv: 1908.10381 [cond-mat.str-el].

[71] Parsa Hassan Bonderson. *Non-Abelian anyons and interferometry*. California Institute of Technology, 2012.

[72] David Aasen, Roger S K Mong, and Paul Fendley. "Topological defects on the lattice: I. The Ising model". In: *Journal of Physics A: Mathematical and Theoretical* 49.35 (Aug. 2016), p. 354001. DOI: 10.1088/1751-8113/49/35/354001.

[73] F J Burnell, Steven H Simon, and J K Slingerland. "Phase transitions in topological lattice models via topological symmetry breaking". In: *New Journal of Physics* 14.1 (Jan. 2012), p. 015004. DOI: 10.1088/1367-2630/14/1/015004.

[74] Kevin Slagle, David Aasen, Dominic Williamson, and Wilbur Shirley. private communication.

[75] Douglas R Farenick. *Algebras of linear transformations*. Springer Science & Business Media, 2000.

[76] Roger A. Horn and Charles R. Johnson. *Matrix Analysis*. 2nd. Cambridge; New York: Cambridge University Press, 2013. ISBN: 9780521839402.

[77] Yuting Hu, Nathan Geer, and Yong-Shi Wu. "Full dyon excitation spectrum in extended Levin-Wen models". In: *Phys. Rev. B* 97 (19 May 2018), p. 195154. DOI: 10.1103/PhysRevB.97.195154.

[78] Tian Lan and Xiao-Gang Wen. "Topological quasiparticles and the holographic bulk-edge relation in (2 + 1)-dimensional string-net models". In: *Phys. Rev. B* 90 (11 Sept. 2014), p. 115119. DOI: 10.1103/PhysRevB.90.115119.

[79] Chien-Hung Lin, Michael Levin, and Fiona J. Burnell. "Generalized string-net models: A thorough exposition". In: *Phys. Rev. B* 103 (19 May 2021), p. 195155. DOI: 10.1103/PhysRevB.103.195155.

[80] Zhenghan Wang. *Topological quantum computation*. 112. American Mathematical Soc., 2010.

[81] Marc D. Schulz and Fiona J. Burnell. "Frustrated topological symmetry breaking: Geometrical frustration and anyon condensation". In: *Phys. Rev. B* 94 (16 Oct. 2016), p. 165110. DOI: 10.1103/PhysRevB.94.165110.

[82] Eric Rowell, Richard Stong, and Zhenghan Wang. "On Classification of Modular Tensor Categories". In: *Communications in Mathematical Physics* 292.2 (Dec. 2009), pp. 343–389. ISSN: 1432-0916. DOI: 10.1007/s00220-009-0908-z.

[83] K. J. Satzinger et al. “Realizing topologically ordered states on a quantum processor”. In: *Science* 374.6572 (2021), pp. 1237–1241. DOI: 10.1126/science.abi8378.

[84] Yu-Jie Liu, Kirill Shtengel, Adam Smith, and Frank Pollmann. “Methods for Simulating String-Net States and Anyons on a Digital Quantum Computer”. In: *PRX Quantum* 3 (4 Nov. 2022), p. 040315. DOI: 10.1103/PRXQuantum.3.040315.

[85] G. Vidal. “Entanglement Renormalization”. In: *Phys. Rev. Lett.* 99.22 (2007), p. 220405. DOI: 10.1103/PhysRevLett.99.220405.

[86] Xie Chen, Zheng-Cheng Gu, and Xiao-Gang Wen. “Local unitary transformation, long-range quantum entanglement, wave function renormalization, and topological order”. In: *Phys. Rev. B* 82 (15 Oct. 2010), p. 155138. DOI: 10.1103/PhysRevB.82.155138.

[87] F.J. Burnell. “Anyon Condensation and Its Applications”. In: *Annual Review of Condensed Matter Physics* 9.1 (2018), pp. 307–327. DOI: 10.1146/annurev-conmatphys-033117-054154.

[88] Davide Gaiotto, Anton Kapustin, Nathan Seiberg, and Brian Willett. “Generalized global symmetries”. In: *Journal of High Energy Physics* 2015.2 (Feb. 2015), p. 172. ISSN: 1029-8479. DOI: 10.1007/JHEP02(2015)172.

[89] F. A. Bais and J. K. Slingerland. “Condensate-induced transitions between topologically ordered phases”. In: *Phys. Rev. B* 79 (4 Jan. 2009), p. 045316. DOI: 10.1103/PhysRevB.79.045316.

[90] Alexei Kitaev and Liang Kong. “Models for gapped boundaries and domain walls”. In: *Communications in Mathematical Physics* 313.2 (2012), pp. 351–373. DOI: https://doi.org/10.1007/s00220-012-1500-5.

[91] Liang Kong. “Anyon condensation and tensor categories”. In: *Nuclear Physics B* 886 (2014), pp. 436–482. ISSN: 0550-3213. DOI: https://doi.org/10.1016/j.nuclphysb.2014.07.003.

[92] Ling-Yan Hung and Yidun Wan. “Generalized ADE classification of topological boundaries and anyon condensation”. In: *Journal of High Energy Physics* 2015.7 (2015), pp. 1–29.

[93] Anton Kapustin and Natalia Saulina. “Topological boundary conditions in abelian Chern–Simons theory”. In: *Nuclear Physics B* 845.3 (2011), pp. 393–435. ISSN: 0550-3213. DOI: https://doi.org/10.1016/j.nuclphysb.2010.12.017.

[94] Maissam Barkeshli, Chao-Ming Jian, and Xiao-Liang Qi. “Classification of topological defects in Abelian topological states”. In: *Phys. Rev. B* 88 (24 Dec. 2013), p. 241103. DOI: 10.1103/PhysRevB.88.241103.

[95] Maissam Barkeshli, Chao-Ming Jian, and Xiao-Liang Qi. "Theory of defects in Abelian topological states". In: *Phys. Rev. B* 88 (23 Dec. 2013), p. 235103. DOI: 10.1103/PhysRevB.88.235103.

[96] Michael Levin. "Protected Edge Modes without Symmetry". In: *Phys. Rev. X* 3 (2 May 2013), p. 021009. DOI: 10.1103/PhysRevX.3.021009.

[97] Daniel Bulmash and Thomas Iadecola. "Braiding and gapped boundaries in fracton topological phases". In: *Phys. Rev. B* 99 (12 Mar. 2019), p. 125132. DOI: 10.1103/PhysRevB.99.125132.

[98] Zhu-Xi Luo, Ryan C. Spieler, Hao-Yu Sun, and Andreas Karch. "Boundary theory of the X-cube model in the continuum". In: *Phys. Rev. B* 106 (19 Nov. 2022), p. 195102. DOI: 10.1103/PhysRevB.106.195102.

[99] F. J. Burnell, Steven H. Simon, and J. K. Slingerland. "Condensation of achiral simple currents in topological lattice models: Hamiltonian study of topological symmetry breaking". In: *Phys. Rev. B* 84 (12 Sept. 2011), p. 125434. DOI: 10.1103/PhysRevB.84.125434.

[100] Julien Vidal, Sébastien Dusuel, and Kai Phillip Schmidt. "Low-energy effective theory of the toric code model in a parallel magnetic field". In: *Phys. Rev. B* 79 (3 Jan. 2009), p. 033109. DOI: 10.1103/PhysRevB.79.033109.

[101] Arpit Dua, Pratyush Sarkar, Dominic J. Williamson, and Meng Cheng. "Bifurcating entanglement-renormalization group flows of fracton stabilizer models". In: *Physical Review Research* 2.3 (July 2020). DOI: 10.1103/physrevresearch.2.033021.

[102] Arpit Dua, Dominic J. Williamson, Jeongwan Haah, and Meng Cheng. "Compactifying fracton stabilizer models". In: *Phys. Rev. B* 99 (24 June 2019), p. 245135. DOI: 10.1103/PhysRevB.99.245135.

[103] Michael Levin and Zheng-Cheng Gu. "Braiding statistics approach to symmetry protected topological phases". In: *Phys. Rev. B* 86 (11 Sept. 2012), p. 115109. DOI: 10.1103/PhysRevB.86.115109.